Multiple Defects Induced Catalytic and Optical Properties in Se Doped ZnO Nanorods for Environmental and Healthcare Applications

Ph.D. Thesis

By

A.V.R. KRISHNA RAO

DISCIPLINE OF BIOSCIENCES AND BIOMEDICAL ENGINEERING
INDIAN INSTITUTE OF TECHNOLOGY INDORE
JANUARY 2021

Multiple Defects Induced Catalytic and Optical Properties in Se Doped ZnO Nanorods for Environmental and Healthcare Applications

A THESIS

Submitted in partial fulfillment of the requirements for the award of the degree of

DOCTOR OF PHILOSOPHY

by

A.V.R. KRISHNA RAO

DISCIPLINE OF BIOSCIENCES AND BIOMEDICAL ENGINEERING
INDIAN INSTITUTE OF TECHNOLOGY INDORE
JANUARY 2021

INDIAN INSTITUTE OF TECHNOLOGY INDORE

CANDIDATE'S DECLARATION

I hereby certify that the work which is being presented in the thesis entitled **Multiple Defects Induced Catalytic and Optical Properties in Se Doped ZnO Nanorods for Environmental and Healthcare Applications** in partial fulfillment of the requirements for the award of the degree of **DOCTOR OF PHILOSOPHY** and submitted in the **DISCIPLINE OF BIOSCIENCES AND BIOMEDICAL ENGINEERING, INDIAN INSTITUTE OF TECHNOLOGY INDORE**, is an authentic record of my own work carried out during the time period from July 2015 to January 2021 under the supervision of **Dr. VENKATESH CHELVAM**, Associate Professor, Discipline of Chemistry, IIT Indore.

The matter presented in this thesis has not been submitted by me for the award of any other degree of this or any other institute.

31 January, 2021

Signature of the student with date
(A.V.R. KRISHNA RAO)

This is to certify that the above statement made by the candidate is correct to the best of my knowledge.

Jan.31, 2021

Signature of Thesis Supervisor with date
(Dr. VENKATESH CHELVAM)

A.V.R. Krishna Rao has successfully given his Ph.D. Oral Examination held on Aug.5, 2021

Aug.5, 2021

Signature of Thesis Supervisor with date
(Dr. VENKATESH CHELVAM)

Acknowledgements

It is my great pleasure to acknowledge all the individuals who have helped and supported me over the last six years for the completion of this thesis. I would like to express my deep sense of gratitude and thanks to my supervisor, Dr. Venkatesh Chelvam, for giving me the opportunity to work on such an exciting research area. His excellent supervision, advice, and guidance from the very early stage made the completion of this study possible.

I also like to extend my gratitude to my PSPC members, Dr. Debasis Nayak and Dr. Sanjay Kumar Singh, for their guidance and valuable suggestions during my whole research work.

With great pleasure, I express my respect to Prof. Neelesh Kumar Jain (Director) Indian Institute of Technology Indore for his encouragement and for providing all the facilities at the Indian Institute of Technology Indore.

I would like to acknowledge IIT Indore for providing laboratory and financial support during my work.

I would also like to thank Dr. Prashant Kodgire (DPGC, BSBE), Dr. Debasis Nayak (Head, Discipline of BSBE), and the entire faculty for their guidance and support.

I extend my deep appreciation to my group members, Mr. Sagnik Sengupta, Mr. Ramesh Reddy B., Ms. Mena Asha Krishnan, Mr. Amit Pandit, Mr. Premansh Dudhe, for their generous help and co-operation to make my work successful.

I would like to thank the Ministry of Human Resource and Development (MHRD), New Delhi, for a research fellowship.

I am thankful to Mr. Kinney Pandey, Mr. Ghanshyam Bhavsar, Dr. Ravinder, Mr. Arif Patel, and Mr. Manish Kushwaha for their technical help and support. I would also like to acknowledge Ms. Anjali Bandiwadekar, Mr. Rajesh Kumar, other library staff, and non-technical staff of IIT Indore for their constant help during my Ph.D. program.

I would also like to thank IIT Bombay (Sophisticated Analytical Instrument Facility), University of Hyderabad, Indian Institute of Science Education and Research Bhopal, for providing the facility for sample characterization during my manuscript submission and revisions.

I would personally like to extend my admiration to all my friends during various times of my Ph.D. period, M.Tech friends (Dr. Naren Raja, Dr. Kiran P. Shejale, Dr. Uday Kumar Sukumar, Dr. Chaitanya Narayanam, Dr. Amit Panwar, Dharmveer Choudhary, Harjeet Singh), Dr. Arun Kumar Verma, Ms. Anjali Roy, Ms. Akanksha Tiwari, Monika Jain, Rinki Singh, Ritudhwaj Tiwari, Shyam Singh, Dr. Biju Majumdar, Mr. Soumya Kanti Dey, Mr. Sayan Maity, Ms. Nishu Kanwa, Dr. Arpan Bhattacharya, Dr. Jamuna K. Vaishnav, Mr. Siddarth Jain, Mr. Abhiram Panigrahi, Ms. Neha Thakur, Ms. Daisy Sarma, B. Praveen Reddy, T. Venu Madhav, R. Sunil Kumar who were always there to support and never let me down during these Ph.D. days.

Most importantly, none of this would have been possible without the support of my family, and I deeply express my love and gratitude to my lovable parents (Mr. Sammaiah and late Mrs. Kousalya), my wife (Mrs. Revathi), and my daughter (Ms.Tanusrihitha), my sister and brother-in-law (Mrs. Bharathi and Mr. Balakrishna), my cousin brothers and sisters for their support throughout my Ph.D. and in my life.

A.V.R. Krishna Rao

Dedicated to my

Mother (Late) and Father

A.V.R. Krishna Rao

Abstract

Environment and healthcare are very closely related to each other, and human health is greatly influenced by the surrounding environment. The environment is essential for the survival of the earth planet and its living organisms that are uniquely positioned to be at the forefront of progress. Human beings are exposed to various environmental risk factors and toxic chemicals derived from chlorofluorocarbons, heavy metals, volatile organic compounds, hydrocarbons, and pesticides that are major causes of various diseases. Therefore, in the present thesis work, the preparation and application Se doped ZnO nanorods in biodiesel production, detection of mercury and optical properties for environmental and healthcare applications are reported. Se doped ZnO generates multiple zinc (V_{Zn}), oxygen (V_O) vacancies and oxygen interstitials (O_i) defects, in the crystal lattice that are characterized by XRD, XPS, EPR and PL studies. Oxygen interstitials (O_i) play essential role in enhancing basic site reactivity in transesterifcation reaction and was found to be usage of 1:20 oil to methanol volume ratio, 5 wt.% catalyst load, 65 ^oC as reaction temperature to give a maximum yield of 94.7% FAME in 3 h. Photoluminescent Se doped ZnO that was coated with 3-mercaptopropionic acid (3MPA), a chelating ligand to detect mercury ions demonstrate strong affnity for –SH functionality. In the presence of Hg^{2+} ions, 3MPA–Se doped ZnO nanoprobe show effcient turn-on (restoration) photoluminescence over dual emission-quenching phenomenon owing to increased zeta potential (− 17.06 mV) and anti-aggregation effect induced by rapidly separated 3MPA surface ligands bound to selenium doped ZnO within 30 s. This “turn-on” was employed for selective detection of Hg^{2+} ions with the lowest limit of concentration to 1 pM. Later, multiple defects induced multicolor emissions by single and two-photon single wavelength excitations show broad emission with and a large Stokes shift of about 250

nm due to overlapping of defects in electronic transitions. The EPR signals also reveal detail information about these defects and show correlation with optical electronic transition states of blue, green and red emissions in Se doped ZnO NRs. Two-photon confocal studies of Se doped ZnO NRs shows multicolor emission at 720, 800 and 860 nm excitations which are consistent with one photon fluorescence at 360, 400 and 430 nm excitations.

List of publications

1. **A.V.R. Krishna Rao**, Premansh Dudhe, Venkatesh Chelvam. Role of oxygen defects in basicity of Se doped ZnO nanocatalyst for enhanced triglyceride transesterification in biodiesel production. Catal. Commun. 149 (2021), 106258. (Impact Factor: 3.6)

2. **A.V.R. Krishna Rao**, R. B. Reddy, S. Sengupta, V. Chelvam. Efficient "turn-on" nanosensor by dual emission-quenching mechanism of functionalized Se doped ZnO nanorods for mercury (II) detection. Appl. Nanosci. 8 (2018) 1973–1987. (Impact Factor: 2.8)

3. **A.V.R. Krishna Rao**, Venkatesh Chelvam. Defects Induced multicolor down- and up-conversion fluorescence in Se doped ZnO nanorods by single wavelength excitation. Opt. Mater. 107 (2020), 110122. (Impact Factor: 2.7)

TABLE OF CONTENTS

List of Figures

Chapter 1

Introduction

List of Tables

Chapter 2

Role of oxygen defects in the basicity of Se doped ZnO nanocatalyst for enhanced triglyceride transesterification in biodiesel production

Chapter 3

Efficient "turn-on" nanosensor by dual emission-quenching mechanism of functionalized Se doped ZnO nanorods for mercury (II) detection

LIST OF SCHEMES

Chapter 1

Introduction

Chapter 2

Role of oxygen defects in the basicity of Se doped ZnO nanocatalyst for enhanced triglyceride transesterification in biodiesel production

Chapter 3

Efficient "turn-on" nanosensor by dual emission-quenching mechanism of functionalized Se doped ZnO nanorods for mercury (II) detection

ACRONYMS

Abbreviations used for amino acids, peptides, derivatives, substituents, reagents, etc., are largely in accordance with the recommendations of the IUPAC-IUB commission on Biochemical Nomenclature, 1974, Pure and Applied Chemistry, 40, 315-331. The abbreviations used in this thesis are listed below.

0D	Zero-Dimensional
3D	Three-Dimensional
As	Arsenic
$C_2H_2O_4$	Oxalic acid
CB	Conduction Band
Cd	Cadmium
DLE	Deep Level Emission
EIA	International Energy Outlook
EPR	Electron paramagnetic resonance
FTIR	Fourier Transform Infrared
GaN	Gallium Nitride
GC	Gas Chromatography
GC-MS	Gas Chromatography Mass Spectrometry
g-factor	Landé g-factor
Hg	Mercury
HIV	Human Immunodeficiency Virus
HOMO	Highest Occupied Molecular Orbital
HPLC	High-Performance Liquid Chromatography
IR	Infra-Red
LUMO	Lowest Unoccupied Molecular Orbital
MeOH	Methanol
MQ	Milli-Q
NaCl	Sodium Chloride

NaOH	Sodium hydroxide
NBE	Near-Band-edge Emission
NIR	Near Infra-Red
NIST	National Institute of Standards & Technology
NOx	Nitric oxide (NO), Nitrogen Dioxide (NO_2)
O_3	Ozone
O_i	Oxygen Interstitial
O_{Zn}	Oxygen Anti-site
Pb	Lead
pH	The negative logarithm of hydronium-ion
PL	Photoluminescence
QD	Quantum Dot
Se	Selenium
SHG	Second Harmonic Generation
SO_2	Sulphur dioxide
SPION	Superparamagnetic Iron Oxide Nanoparticles
TPA	Two-Photon Absorption
TS-TPA	Two-Step Two-Photon Absorption
VB	Valence Band
V_O	Oxygen Vacancy
VOC	Volatile organic compounds
V_{Zn}	Zinc Vacancy
XPS	X-ray Photoelectron Spectroscopy
XRD	X-Ray Diffraction
$Zn(CH_3COO)_2$	Zinc acetate
Zn_i	Zinc Interstitial
ZnO	Zinc Oxide
Zn_O	Zinc Anti-site

Symbols/Units

α	Alfa
Å	Angstrom
a. u.	Arbitrary Unit
β	Beta
cm	Centimetre
°	Degree
°C	Degree Centigrade
δ	Delta
ε	Extinction coefficient
γ	Gamma
µm	Micrometre
µm	Micromolar
mmol	Millimole
mL	Millilitre
µL	Microlitre
nm	Nanometre
nM	Nanomolar
π	Pi
λ	Wavelength

Chapter 1

Introduction

1.1 Environment and Healthcare

Environment and healthcare are closely related to each other, and human health is greatly influenced by the surrounding environment. Human beings exposed to various environmental risk factors and toxic chemicals derived from chlorofluorocarbons, volatile organic compounds (VOCs), hydrocarbons, and pesticides, are significant causes of multiple diseases [1]. The polluted environment can significantly affect human health, and a less commonly known fact is that advancement in human health will also affect the ecosystem. The energy demand increases with inflation, structural reforms, and rising population, which will actively add to the total world energy consumption [2]. The extensive use of energy resources like fossil fuels, petroleum, coal, and natural gas emits pollutants that affect the environment and healthcare in a significant manner. In this way, the environment and healthcare are dependent on each other.

1.1.1 Global energy outlook

The world energy outlook provides critical analysis and insights into energy demand developments–supply, energy security, environmental protection, and economic development [3]. World energy developments have gone through a progression from firewood to coal and further promoted to oil and gas. Earlier, the world's primary energy supply was dominated by fossil fuels for economic growth. The energy consumption from most non-renewable energy resources includes fossil fuels like crude oil, natural gas, and coal. The demand for fossil fuel utilization is the leading cause of global climate change and creates several other environmental and health problems [4]. Developments in human health, such as increased energy consumption, advanced disease diagnosis, and

reduced mortality, can also cause environmental damage, such as increased fossil fuels consumption, deforestation, global warming, and pollution [5]. With the rapid growth of world energy consumption, renewables are the fastest-growing energy source between 2018 and 2050, surpassing non-renewables to become the most used energy source (International Energy Outlook, EIA, 2019), as shown in **Figure 1.1** [2].

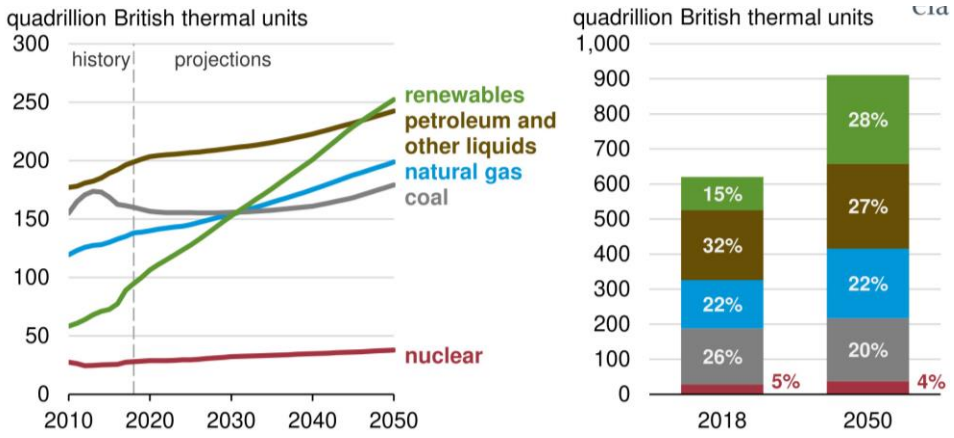

Figure 1.1 Global energy consumption by energy source [2].

The impact on the environment, loss of biodiversity, excess use of natural resources for energy demand, and health problems are critically linked to a sustainable ecosystem. The hydropower, wind, solar, and biomass clean energy substitutes are being developed and implemented at an increasing pace to provide upcoming energy demands, thereby playing a major role in ensuring the total energy supply and promotion of clean energy. The renewable energy technologies including electrification will lead to improvement in long term energy efficiency measures [6]. Worldwide coal and oil demand have already peaked, and there is a significant increase in electricity use, which is increasingly generated using renewable sources, as shown in **Figure 1.2** [3]. Therefore, the global energy system must undergo a clean energy transition to address these challenges, whereby increasingly cleaner sources replace energy sources that emit greenhouse gases.

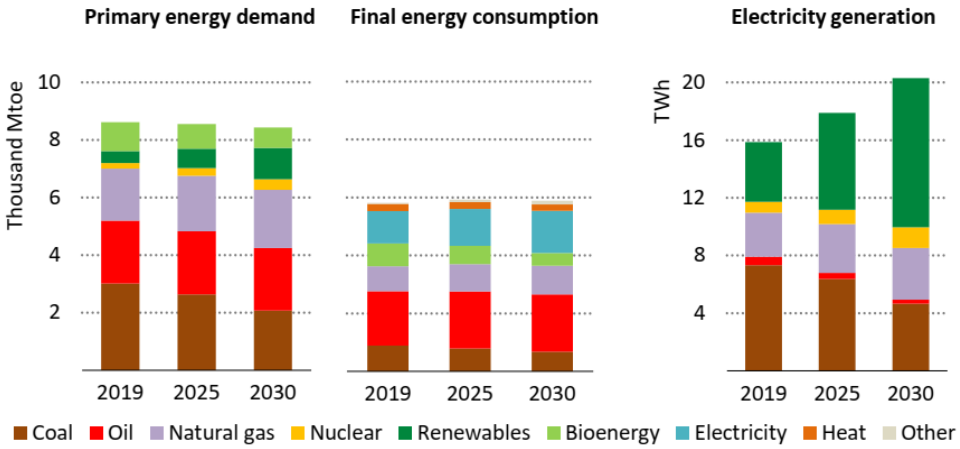

Figure 1.2 Energy sectors transformation in emerging market [3].

1.1.2 Environmental pollution

Our ecosystem has been changing significantly in recent years. Important issues contributing to the ecological changes include an increasing world population, global warming, industrial development, technological advancement, and economic growth. Some other changes are deteriorating air, water, and soil pollution, intensifying toxic wastes, hazardous chemicals, acid rain, ozone depletion, and increasing disruptors in the environment [7]. These changes have a discerning influence on the health and well-being of all living organisms.

Many pollutants present in indoor and outdoor air include SO_2, NOx, CO, O_3, photochemical oxidants, cigarette smoke, heavy metals such as lead, arsenic, cadmium, mercury, and different kinds of VOCs [8]. Air pollutions leading causes are burning fossil fuels for electricity generation, the transportation sector, industrial processes, heating, etc. The primary water contamination sources include discharging inorganic and organic effluents, petrochemicals, municipal solid wastes, agricultural wastes, etc. [9]. In addition to heavy metals, several inorganic and organic chemical compounds can pollute streams, lakes, canals, and rivers, alarming their water quality. Another primary concern is the potential harmful effect of releasing an increasing number of unnatural chemicals into the soil,

causing land pollution [10]. Also, the chemicals release is not restricted to areas nearby their point sources such as industrial facilities. Instead, the chemical substances can move to faraway regions where they may cause harmful effects on humans and the ecosystem, as shown in **Figure 1.3** [11]. The air, water, and soil pollution cause multiple diseases from perinatal disorders, infant mortality, respiratory infections, malignancies, cardiovascular disorders, and other harmful effects [12].

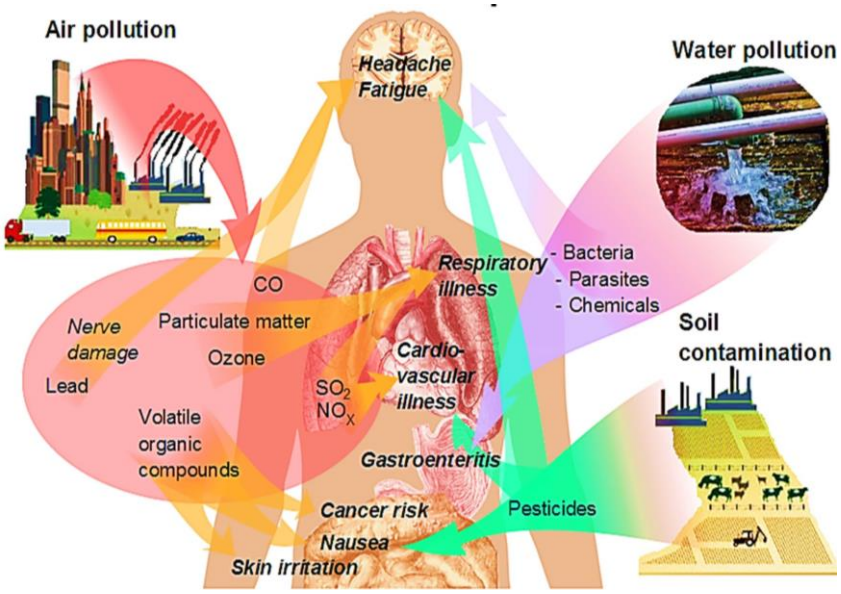

Figure 1.3 Health effects on humans from air, water, and soil pollution [11]

Environment contamination by heavy metals (Hg^{2+}, Cd^{2+}, As^{3+}, Pb^{2+}, etc.) is becoming a serious problem since they tend to accumulate in the ecological food chain, causing various adverse effects on human ecosystem health [13]. Mercury is considered as a global pollutant that affects humans due to its long-range transportation and persistence in the environment [14]. The natural, anthropogenic, and industrial practices that release Hg into the atmosphere include volcanic eruptions, geothermal emissions, gold mining, and coal and power plants combustion [15]. In the environment, inorganic Hg(II) form is prevalent in water, soil, and sediment, whereas methylmercury (MeHg) is predominant in aquatic

organisms and Hg(0) in the atmosphere, as shown in **Figure 1.4** [16,17]. Mercury is highly toxic to humans. The harmful effects of occupational exposure to mercury cause Mad Hatter disease reported from the 18th and 19th centuries related to mercury toxicity [18]. Methylmercury concentrations are elevated by bioaccumulation and biomagnified through the food chain. The MeHg toxicity discovered in Minamata City was due to consumption of fish and shellfish contaminated with methylmercury from wastewater discharge by Chisso Corporation [19]. Methylmercury poisoning leads to developmental toxicity in the fetal and neonatal brain because MeHg can pass the placenta and cross blood-brain barrier. Prenatal mercury exposure interferes with neuron growth and cause irreversible damage to the developing central nervous system [20]. Therefore, the main objective of several researches is to protect our environment and promote human health by monitoring and detecting mercury compounds.

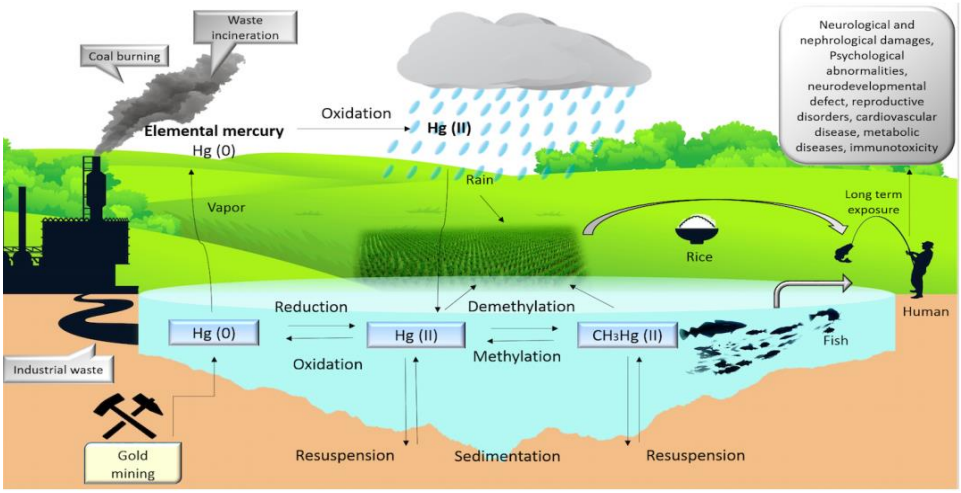

Figure 1.4 Mercury occurrence and mobility [16,17]

1.1.3 Global healthcare

Global healthcare understands complications and threats that focus on diagnosis and treatment of diseases in improving healthcare equity for worldwide populations [21]. The international healthcare goal needs to

work toward the future in prevention and early intervention rather than treatment. Humans interact with different environmental factors and affect the quality of life, healthy life, and health disparities, causing diseases.

Pandemics are large-scale disease that can significantly increase morbidity and mortality worldwide. These pandemics include coronavirus, influenza (H1N1), Ebola, plague, HIV infection, and other viral threats that address our vulnerability to widespread diseases that the world has encountered [22]. Growing concerns in the ecosystem change air, water, and soil pollution and directly affect the human population's health. Environmental pollutants are also a significant contributor to climate change, impacting people's health differently. Climate change health effects include increased respiratory, cardiovascular, malaria, cholera, viral infection due to extreme weather conditions, and geographical distribution of air and water-borne diseases [23]. Despite progress in the medical field, many communities worldwide still lack access to primary healthcare education, causing heart disease, stroke, cancer, etc. These diseases can also be attributed due to physiological and environmental factors. Agricultural practices in the environment, including irrigation, use of inorganic fertilizers and pesticides, can affect flora and fauna, making disease transmission a major concern associated at every stage of the food production and supply chain [24]. Many deals with preventive and control of diseases while addressing health threats from environmental health risks and causes of diseases. Therefore, monitoring and controlling global challenges such as environmental hazards and human disease diagnosis are essential in the environment and healthcare sector in advancing global health.

1.2 Conventional methods for monitoring environment and healthcare

Monitoring the environment and healthcare is essential in protecting ecosystems from energy crises, pollutants, diseases, and mental health.

Thus the necessity for understanding between environmental quality and public health had been a significant challenge [25]. Conventional energy resources (coal, petroleum, natural gas and nuclear) are finite but still continue to expand use even though pollution remains inevitable. However, renewable energy resources (wind, solar, tidal, and biomass) are clean and abundantly available in nature that are potential future energy resources to meet the world's energy demand [26]. Wind and biomass dominate projected growth in renewable energy generation, apart from hydropower, as reported in Annual Energy Outlook 2012, as shown in **Figure 1.5** [27]. The non-hydro renewable energy contributions to the total generation in the projection rise from 4% in 2010 to 9% in 2035.

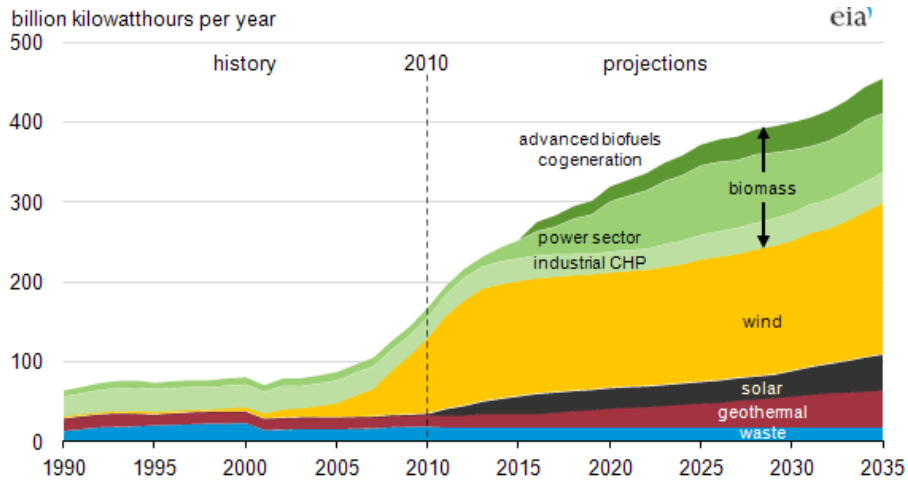

Figure 1.5 Projected (2010-2035) renewable energy generation [27]

The biomass energy production and use can greatly reduce greenhouse gas emissions, renewable resources (wind, solar and hydro) limitations, and finally support local agricultural production, agroforestry and forest-product sectors [28]. Another advantage of biomass is its ability to convert into a wide range of valuable biofuels, bioproducts, chemicals, etc. The advantages of biodiesel over other biofuel come from lower agricultural inputs and more efficient conversion of feedstocks [29]. Biodiesel is a renewable energy source derived from oils/fats consisting of long-chain fatty acid methyl esters (FAMEs) as shown in **Scheme 1.1**. Biodiesel

produced from biological resources by conventional methods include direct use and blending, pyrolysis, micro-emulsification, and transesterification reaction [30]. The transesterification process is the best choice for increasing conversion efficiency and minimizing the production cost in biodiesel production [31–33].

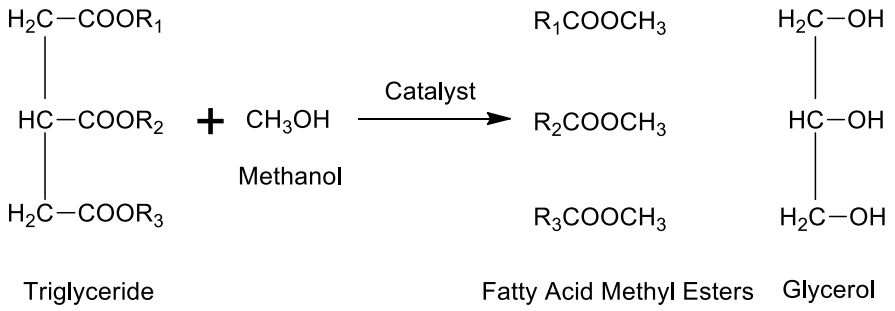

Scheme 1.1 General reaction of the transesterification reaction

The environment quality was maintained and restored by removing contaminants from the environment to prevent ecosystem and healthcare problems. Modern environmental contaminants or pollutants analysis and detection techniques include spectroscopy (UV-Vis, Fluorescence, IR), chromatography (GC, GC-MS, HPLC), and electrochemical methods [17,34,35]. Monitoring of contaminants in the environmental and human healthcare applications entails various identification and molecular imaging techniques but limited in their utility due to cost factor [36–38]. The alternate biofuels, monitoring of pollutants, and diagnosis of human diseases are essential in improving the environment and healthcare. Therefore, environmental and healthcare problems have driven many researchers to explore innovative nanotechnology solutions due to their special physical and chemical properties [39–41].

1.3 Implications of nanotechnology in environment and healthcare

Nanotechnology is the engineering and fabrication of functional structures with molecular precision at 100 nm or smaller dimensions. It has been

observed that the physical, chemical, electrical, optical, and electronic properties of some materials can change at their nanoscales [42]. Nanotechnology evolution represents an ever-increasing demand in the design, synthesis, modification, and creation of novel nanomaterials [43,44]. Organic nanomaterials such as liposomes, hybrid nanomaterial, polymer constructs, nanospheres, and micelles, were employed in the past for imaging and drug delivery applications. Inorganic nanomaterials have recently attracted the attention of many researchers in recent decade due to their unique materials and size-dependent physicochemical characteristics such as inertness, biocompatibility, chemical stability, and ease of functionalization as shown in **Figure 1.6** [45]. Emerging techniques such as nanomaterials-based finding are of future interest because of unique optical, electrical, electronic, magnetic, catalytic, and other emerging properties at this scale. Nanomaterials surface modifications provide ligand binding of molecules for specific reactivity to monitor pollutants, catalysts for energy storage, biofuel energy production, disease diagnosis, and therapy [46,47]. Therefore, these emergent properties have great potential applications in the environment, industry and medicine, and other fields.

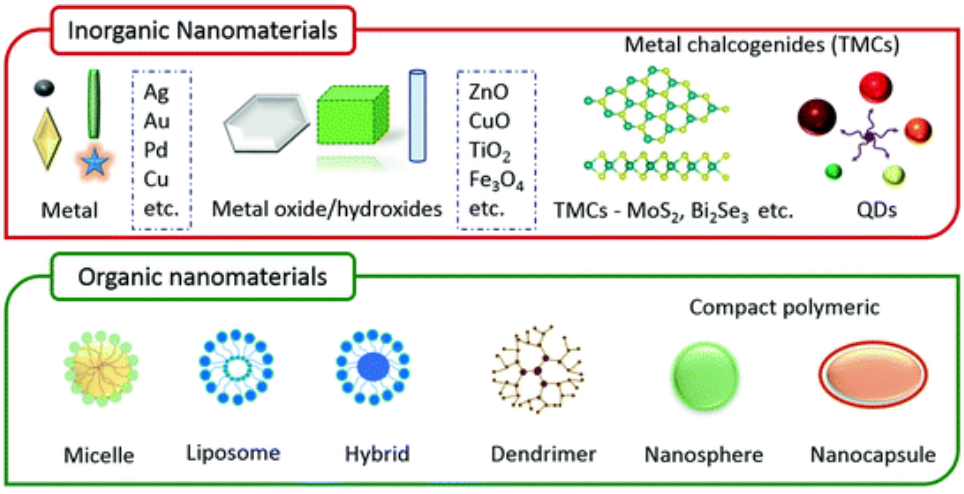

Figure 1.6 Organic and inorganic nanomaterials for environmental and healthcare applications [45]

Nanocatalyst is a functional material with either external or internal catalytic properties within nanoscale dimensions. Nanocatalyst has a high surface-to-volume ratio, which results in enhanced catalytic performance due to more active surface area and adsorption of the reactants [48]. Nanocatalysis unlocks many doors in a sustainable technology for numerous applications (**Figure 1.7**), extending from more established research areas such as oil refineries, remediation activities, and food processing to emerging research areas such as bio-refinery processes, reforming nanosensors, and energy harvestation, conversion, and storage. Catalysis is necessary in the green chemistry principles, mainly because it decreases the unit production costs, eliminates the amount of waste, and minimizes the energy use related to a chemical process. The most important nanocatalyst based organic transformations for the selective production of desired products include hydrogenations, oxidations, reductions, alkylations, coupling reactions, cyclizations, amidations, etc. [49]. Nanocatalysts have shown significant role in the production of biofuels from renewable biomass energy resources. Nanocatalysts can also create new opportunities to improve biodiesel conversion efficiency, which is considered as one of the most sustainable energies for the future.

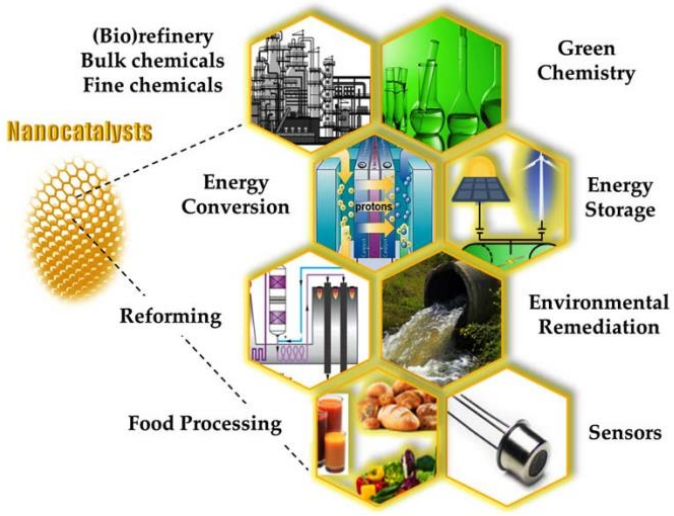

Figure 1.7 Overview of various applications of nanocatalysts [48]

The detection of trace Hg^{2+} is always a research hotspot in developing accurate and sensitive nanomaterial-based chemosensors. Several nanomaterial-based approaches have been designed and developed for the detection of heavy/toxic metals based on their properties. Among the developed detection techniques, optical detection based on fluorescence or colorimetric analysis is the most facile method by its tunable properties, and low detection limit [50]. Some advanced functional nanosystems based on nano, polymeric, AIEgens, aptamers and porous materials are used for selective detection and effective removal of mercury (II) ions [51]. The high catalysis and conductivity of noble metals, such as Au, Cu, Pt, and Ag, strengthen the response signal in biosensing reaction. Carbon materials have been widely used in the electrochemical biosensor, mainly due to their superior conductivity, immobilization of biomolecules and specific surface area [52]. The synergic effects of integrating catalysis and conductivity in a hybrid nanomaterial through chemical bonds improved the detection of mercury. Various well-established nanomaterials possess unique advantages to tackle Hg^{2+} pollution in practical purposes [53,54]. The functional nanomaterials-based mercury detection opens up a new tool wherein conjugation of specific ligands to nanomaterial was employed to detect trace amounts of mercury in the environmental, industrial, and living systems.

The engineering of materials to nanosize offers multiple properties that can be used for the designing and development of biomedical devices [55]. Nanomaterials providing multimodal detection could demonstrate great interest in biosensing and imaging applications, selective targeting, therapy, and diagnostics [56]. The use of nanostructured materials in the biomedical field offers many innovative technologies to fight against cancer, cardiovascular and neurodegenerative disorders, and infections. The nanomaterial platforms that have been widely explored for biomedical engineering applications include mostly inorganic and organic materials

[57]. Organic nanomaterials such as nanocrystals, ferritin, liposomes, dendrimers, polymers, polymer-drug conjugates, and nanogels have been extensively used as imaging and therapeutic agents. In recent times, inorganic nanomaterials such as metal, graphene, metal oxides, quantum dots (QDs), superparamagnetic iron oxide nanoparticles (SPION), upconversion nanomaterials have also attracted particular attention in nanomedicine [58,59].

1.4 Semiconductor nanomaterials

Semiconductor nanomaterials have enticed much attention due to their tunable bandgap, unique quantum size effects, linear and nonlinear optical properties. Semiconductor nanomaterial physio-chemical properties such as electrical, absorption, emission, and charge carriers' motion are explained by quantum mechanical laws obtained from the Schrödinger equation [60,61]. A detailed explanation of the electronic band structure in nanoscale dimensional solids signifies that the electron delocalized in the solid are not bound to individual atoms. Whenever the atomic size becomes comparable with de Broglie wavelength related to the particles that interact with it, a free carrier confined in this low dimensional structure will behave as a particle in a potential box.

The changes in the electronic configurations of the atoms in the nanomaterials due to size effects result in significant differences in properties from their bulk materials. When the atomic size is of the order of de Broglie wavelength, discrete electronic energy levels (**Figure 1.8e)** arise as electrons and holes are spatially quantum-confined, giving rise to the generation of electric dipoles [49,62]. The spacing between the energy levels and bandgap increases with decreasing particle size, causing changes in the nanocrystals' spatial electron energy density configurations, eventually changing the electronic and optical properties [49]. The quantum size effect for bulk (3D), quantum wells (2D), quantum wires/rods (1D), and quantum dots (QDs) (0D) in a semiconductor

material is illustrated in **Figure 1.8(a–d)**. These classes of nanomaterials exhibit quantum confinement effect in zero, one, two, and three dimensions, respectively.

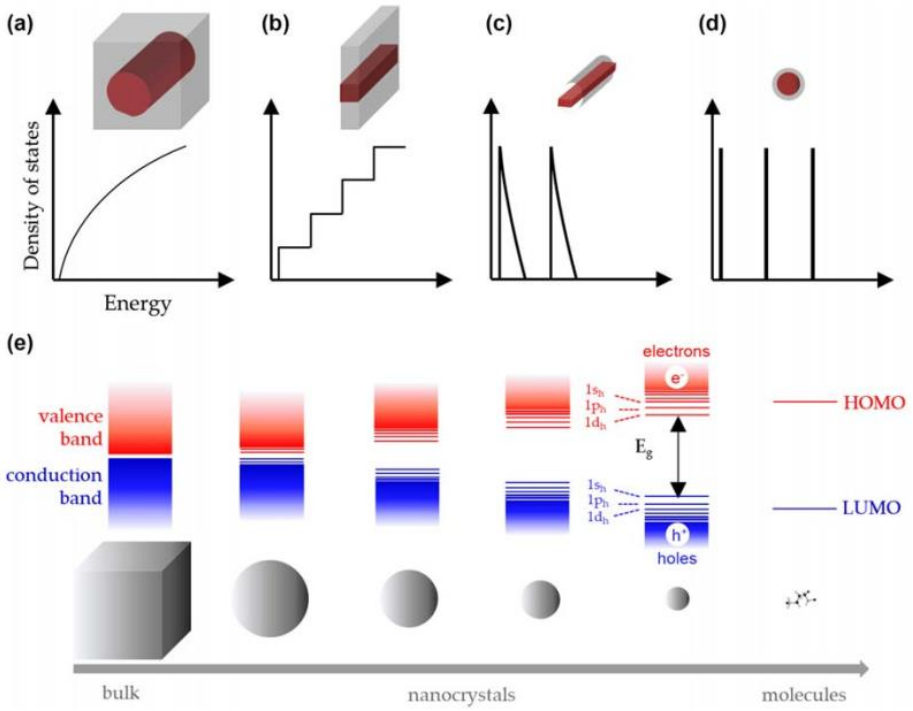

Figure 1.8 Semiconductor material **(a-d)** Quantum size effect in 3D, 2D, 1D, and 0D, **(e)** Size effects on the electronic energy levels [49]

Different semiconductor materials differ in their properties and are tunable. Semiconductors are typically formed from elements in the periodic table groups such as III–V, II-VI, I–VII, V–VI and II–V, oxides, magnetic and inorganic materials, including Si, GaN, InP, TiO_2, Fe_3O_4, ZnO, ZnS, CdSe, AlGaN and ZnSe [63,64]. Semiconductor property of the material, due to high specific surface area, improves many processes such as adsorption, catalysis, charge transfer phenomenon thereby opening avenues for its applications in catalysis, sensing, and optical devices. Metal oxide shows controllable size, shape, crystallinity, reactivity, and functionality compared to other semiconductor materials [65,66]. Therefore, metal oxide holds the potential for playing a critical role in developing materials with new catalytic and optical properties.

Additionally, they have a high probability of becoming highly competitive materials due to their morphological, chemical interfacial properties, and ability to form composite structures. Among metal oxides, TiO_2, WO_3, SnO_2, and ZnO have attracted great interest due to their electrochemical, catalytic sensitive properties and energy band alignment suitable for tunable properties. Transition metal oxides, particularly TiO_2 and ZnO, are widely used in environmental and healthcare applications because of their unique photophysical and optoelectronic properties [67–69]. Most preferentially, among different transition metal oxides, ZnO plays an important role in gas sensors, chemical sensors, bio-sensors, cosmetics, antibacterial agents, optical and electronic devices, solar cells, catalysts, bioimaging agents, and in drug delivery products.

1.5 Characteristics of ZnO nanostructures

Zinc oxide (ZnO) is a direct bandgap semiconductor material with potential applications as light-emitting devices, transparent conductors, electrodes, and sensors. It typically has the hexagonal wurtzite crystal structure, with the lattice parameters a = 3.25 Å and c = 5.21 Å [70]. Its bandgap is 3.437 eV at low temperatures and 3.37 eV at room temperature. Notably, the structural (sizes, defects, and doping) and optical parameters play an essential role in their considerable exciton binding energy (60 meV), strong luminescence properties, and high electron mobility [71,72]. Therefore, investigation of the structural parameters becomes imperative for optimizing the ZnO nanostructure's performance.

The ZnO bonding in its crystal lattice involves a sp^3 hybridization forming four equivalent orbitals, directed to the four corners of tetrahedral geometry. In the resulting crystal, the bonding sp^3 states constitute the valence band (VB), while the conduction band (CB) originates from its antibonding counterpart [73]. The resulting energy gap is 3.37 eV, i.e., in the UV region of the spectrum, which has triggered interest in ZnO as a

material for photodetectors, transparent electronics, and spintronics. Generally, this atomic arrangement of tetrahedrons may result either in a cubic zinc-blende-type or in a hexagonal wurtzite-type crystal structure, based on the stacking sequence of bi-layers. The crystal structures exhibited by ZnO include wurtzite, zinc blende, and rock salt, as shown in **Figure 1.9** [74]. Under ambient conditions, the thermodynamically stable crystal structure is that of the wurtzite phase. The zinc blende phase can be stabilized only by growth on cubic substrates, and the rocksalt crystal structure may be obtained at relatively high pressures, as in the case of GaN.

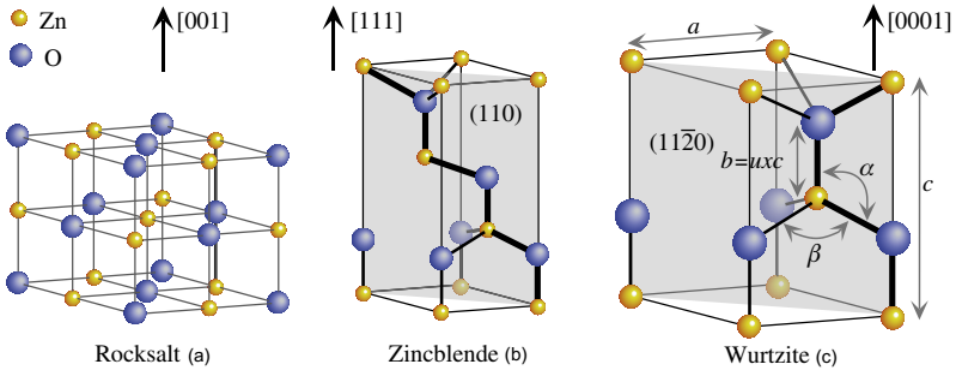

Figure 1.9 ZnO crystal structures representation by stick-and-ball model: **(a)** Rocksalt, **(b)** Zinc blende, and **(c)** Wurtzite [74].

ZnO is the leading metal oxides due to its tunable physical characteristics of wide bandgap (~3.37 eV) with typical exciton binding energy of 60 meV. Researchers have received much attention to engineer its bandgap for various applications in solar cells, sensors, optoelectronics, biomedical devices, etc. [75–77]. The literature reports that the ZnO bandgap can be tuned by either controlled crystallite size or by doping. The degree of bandgap engineering was dependent on the type of doping elements [78]. Therefore, new ZnO based nanomaterials formed by doping elements will exhibit novel properties useful for future applications [79,80].

ZnO with a wide bandgap is a suitable host material for defect centers by intrinsic and extrinsic doping. The intrinsic defects responsible for the ZnO n-type conductivity, formed during deposition, include Zn_i and V_O [81]. The ZnO's doping effect is determined by dopant formation energy, ionization energy, and solubility [82]. Impurities and intentional doping with covalent (differently charged) ions have a remarkable impact on the defect equilibrium. Dopants forming shallow donors and acceptors provide the means of controlling the material's electrical conductivity leading to environmental and healthcare applications [83]. Further, carriers can be introduced in ZnO with lower valence (introduces holes) or higher valence (introduces electrons) ions on the Zn sites [84]. Controlled introduction of doping forms the basis of p-type (acceptor-doped) and n-type (donor-doped) to control carrier confinement, carrier flow, and characteristic properties, as shown in **Figure 1.10** [85–87].

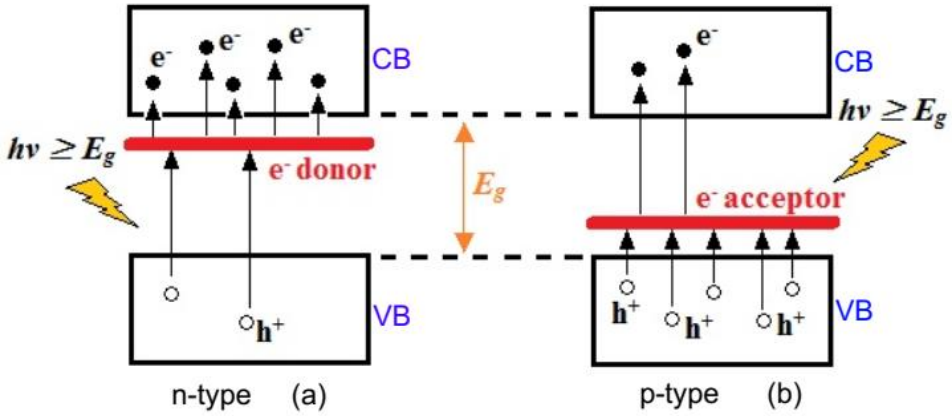

Figure 1.10 Illustration of **(a)** n- and **(b)** p-type doping in ZnO nanomaterial [85].

The n-type doping is relatively well established by substituting group III elements (Al, Ga, and In) on the Zn sites, making highly conductive n-type ZnO. Generally, Al, Ga, and In dopants on the Zn sites and Cl and I dopants on the O sites can potentially form shallow donors in ZnO [88]. For the n-type dopants, chemical elements of group III (B, Al, Ga, and In), rare earth elements in group III (Sc, Y, and La), group IV elements (Si,

Ge, and Sn), and group VII elements (F, Cl, and I) are introduced for creating defects in the ZnO [86]. These heavily doped ZnO have exhibited a systematic blueshift in the optical bandgap attributed due to the Burstein–Moss effect. Difficulties can ascend from a variety of causes to obtain p-type doping in ZnO. The reliable p-type dopants may remain a significant challenge because of compensated low-energy native defects, such as Zn_i or V_O, or residual hydrogen impurities [88,89]. Some compensation centers are held to the same energy level that depends only on the position of valence and conduction bands. There have been many p-type behaviors reports in ZnO, often with very high hole concentrations but with low mobility. The deep impurity level can also be a cause of the doping difficulty, leading to major hindrance in shallow acceptor level formation. Therefore, attainment of intentional n-type doping of ZnO based nanomaterials is relatively easy compared to p-type doping [90].

The doping can generate defects such as vacancies (V_{Zn} and V_O), self-interstitials (Zn_i and O_i), and antisites (Zn_O and O_{Zn}). Their combination introduces donor and acceptor levels in the bandgap. Some of these defective species are introduced during the growth of the material and others during the process [84,91]. Some defects may also cause self-compensation in the crystal structure of the material. Doped ZnO has rich defect chemistry due to low formation energies of various donor defects (V_O, Zn_i, and Zn_O) under normal conditions, whereas acceptor defects (O_i, V_{Zn}, and O_{Zn}) are generated under oxygen-rich conditions (**Figure 1.11**) [92,93]. The Zn_i and V_O defects form donor level in the forbidden energy gap, whereas Zn vacancies generate an acceptor level. The V_O makes deep level donor states whereas the shallow level donor energy states are due to Zn_i. In particular, the oxygen vacancy and the Zn interstitial, which act as donors, have most often been mentioned as sources of n-type conductivity in ZnO [94]. The luminescence of doped ZnO material in visible region is attributed due to various defects. Manipulation and control of doping

generates defect properties used in industrial, environmental, and biomedical applications.

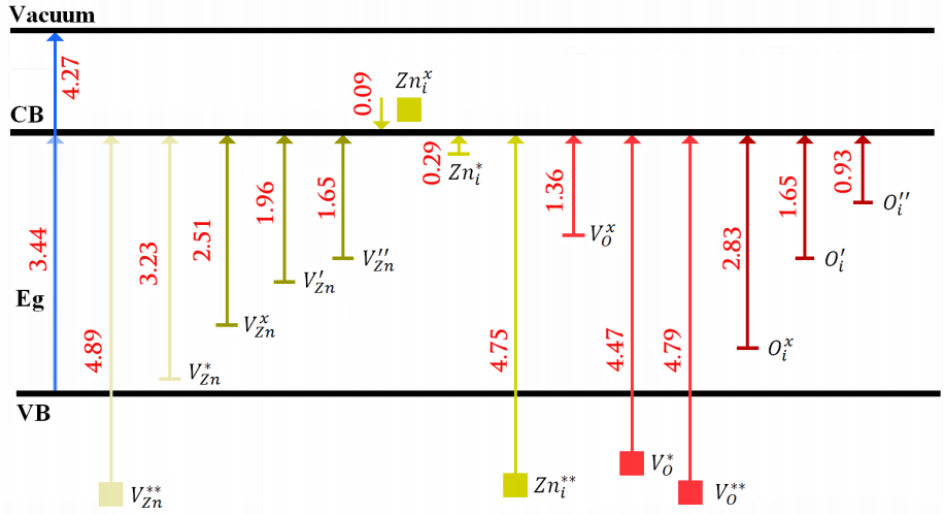

Figure 1.11 ZnO defects energy levels [92]

Photoluminescence (PL) spectra of the ZnO based materials with various nanostructures have been extensively reported. Generally, the PL emission of ZnO nanomaterials has two spectral components [95]. One is the typical exciton emission (electron-hole recombination) or near-band-edge emission (NBE), i.e., photogenerated electron recombination process with holes in traps near the valence band in the UV-Vis region from 350 to 390 nm. The other component is the visible emission region (deep-level emission, DLE), which is related to the defects, such as the peaks between 400 to 640 nm emission in the visible region [96]. ZnO has more extrinsic and intrinsic deep level defects that emit light of different colors ranging from violet to red in visible light spectrum [97,98]. Since ZnO's optical properties originated from native intrinsic and intended extrinsic defects, investigation of various defects has an essential role in tuning different optical properties for environmental and healthcare applications.

ZnO-based materials' remarkable catalytic properties are associated with surface morphology, nanostructure, defects or abilities of electron transportation [99,100]. The introduction of engineering defects improves

the activity of catalysts for industrial applications. ZnO based materials are highly important as components in heterogeneous catalysts, and the activity depends on the density of the surface's active sites [101–103]. The large amount of zinc and oxygen vacancy defects in twin brush (TB) ZnO significantly promote introduction of Au atom into the crystal lattice of ZnO for remarkably high activity in CO oxidation [104]. The dramatic enhancement in CO oxidation is attributed due to the vacancy defects in TB-ZnO. The catalytic applications that involve surface defects include photodegradation of organic compounds, solar energy conversion, biomass conversion, optoelectronics, chemosensing and bioimaging agents [105–108].

Photon (or energy) upconversion is defined as sequential absorption of photons, which yields anti-Stokes emissions. It involves the absorption of two- or more low-energy photons that emits a single photon at higher energy. These processes have been actively explored in recent years due to their exciting applications in optoelectronics, biophotonics, and multi-photon imaging [109,110]. The multiphoton imaging provides advantages of enhanced sensitivity, deep imaging of tissues due to increased penetration, and reduced phototoxicity of NIR light [111]. Therefore, exploring upconversion processes facilitated by different defects energy states with a focus on UV-Vis emissions in ZnO nanomaterials are essential. The defect-mediated photon upconversion provides different physical upconversion mechanisms as shown in **Figure 1.12** [112].

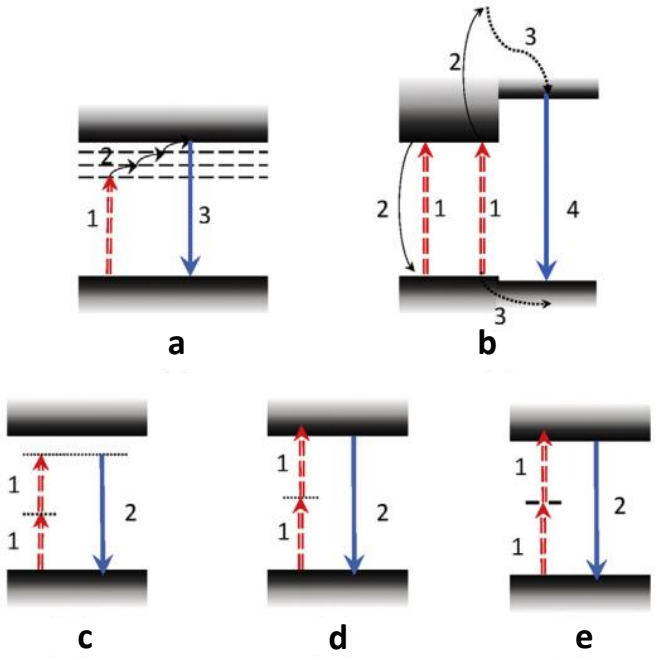

Figure 1.12 Illustration of electronic transitions in photon upconversion **(a)** phonon-assisted (TP), **(b)** auger-mediated upconversion (AM), **(c)** second harmonic generation (SHG), **(d)** two-photon absorption (TPA), and **(e)** two-step two-photon absorption (TS-TPA) [112, 115]

Figure 1.12a describe the phonon-assisted upconversion process that involves absorption of a low-energy photon (labeled 1) into real states (horizontal dashed lines) followed by a vibrational transition into higher energy states (marked 2), from which an anti-Stokes emission (labeled 3) occurs [113]. Auger mediated photon upconversion involves absorption of several photons (labelled 1), generating many electron-hole pairs located near to each other to facilitate energy transfer. The recombination of few of the photoexcited electron-hole pairs (labelled 2) with simultaneous transfer of the released energy create a highly excited (labelled 2 with curved solid arrows) carrier [114]. These carriers experience thermalization and diffusion (labelled 3) process followed by photoexcited carriers recombinations (labelled 4) at higher energy as shown in **Figure 1.12b**. The second harmonic and two-photon absorption (TPA) process

occurs due to the simultaneous absorption of two photons via an intermediate virtual state. However, the final energy state involved in the absorption process's is now a real electronic state of a conduction band (CB) state rather than a virtual state (**Figure 1.12c**) [115]. Therefore, the emitted photons in the second harmonic process have less energy than the two-photon absorption (**Figure 1.12d**) process because carriers may first relax to low-lying electronic energy levels and then contribute to radiative recombination. Defects in nanocrystal structure facilitate second harmonic upconversion nonlinear optical effects in optoelectronic applications. In contrast to TPA, TS-TPA (**Figure 1.12e**) involves real intermediate electronic energy states in consecutive absorption of two photons to produce excited carriers, resulting in recombination processes [116]. Therefore, this process offers a useful alternative for the generation of anti-Stokes emissions as it involves the advantage of relatively high conversion efficiency. The efficiency depends on the energy band gap, lifetime of the intermediate emitting state, electronic band states and defects energy levels.

The most widely utilized two-step TPA up-conversion process allows a significant gain in the photon energy and has a high energy efficiency via donor or acceptor defect states [117]. Currently, these defects states are usually introduced by deliberate doping of ZnO nanomaterials by rare-earth impurities. Utilizing defect-related TS-TPA levels represents an alternative approach for achieving defect induced photon upconversion [118]. The defect mediated photon upconversion process is potentially advantageous for ZnO-based nanomaterials in optoelectronics, industrial, and biomedical applications.

1.6 Reported work

Recently, Se doped ZnO and Se/ZnO based materials synthesis and characterization are reported for photocatalytic, antibacterial, and cholesterol oxidation applications [119–121]. However, the Se doped ZnO nanomaterials nature of defects in the nanostructure responsible for catalytic, optical, and up-conversion properties are not explored and reported in the literature. Presently, the study of multiple defects with broad UV-Vis-NIR emission and large Stokes shift for novel catalytic and optical properties in the development of alternate fuels, optical sensors, optoelectronic devices, and bio-imaging probes will spectacularly impact the environmental and healthcare applications.

1.7 Organization of the thesis

The present thesis has been summarized into five chapters to gain deep insight into the complete research work.

Chapter 1: Describes the introduction of the subject, review of the existing work, and the thesis's scope.

Chapter 2: Depicts the finding of novel defects induced base catalysis in Se doped ZnO to produce biodiesel.

Chapter 3: Describes a novel sensing probe's successful development to detect mercury using Se doped ZnO functionalized 3-mercaptopropionic acid.

Chapter 4: Deals with the study of multiple defects induced down and up optical conversion properties in Se doped ZnO nanorods for optical sensing, optoelectronics, and bioimaging applications.

Chapter 5: Describes the research summary and future scope.

1.8 References

1. Vermeulen R., Schymanski E. L., Barabási A.-L., Miller G. W., (2020), The exposome and health: Where chemistry meets biology. Science, 367, 392–396 (DOI: 10.1126/science.aay3164)

2. EIA, International energy outlook, (2019), (www.iea.org/reports/world-energy-outlook-2019)

3. EIA, World energy outlook, (2020) (www.iea.org/reports/world-energy-outlook-2020)

4. Perera F., (2017), Pollution from fossil-fuel combustion is the leading environmental threat to global pediatric health and equity: Solutions exist, Int J Environ Res Public Health, 15, 16 (DOI: 10.3390/ijerph15010016)

5. Manisalidis I., Stavropoulou E., Stavropoulos A., Bezirtzoglou E., (2020), Environmental and health impacts of air pollution: A review, Front public Heal, 8, 14 (DOI: 10.3389/fpubh.2020.00014)

6. Gielen D., Boshell F., Saygin D., Bazilian M. D., Wagner N., et al., (2019), The role of renewable energy in the global energy transformation, Energy Strateg Rev, 24, 38–50 (DOI: https://doi.org/10.1016/j.esr.2019.01.006)

7. Barinova G. M., Gaeva D. V, Krasnov E. V., (2020), Hazardous chemicals and air, water, and soil pollution and contamination - Good health and well-being, Springer International Publishing, 2020, 255–266 (DOI: 10.1007/978-3-319-95681-7_48)

8. Tran V. Van, Park D., Lee Y.-C., (2020), Indoor air pollution, related human diseases, and recent trends in the control and improvement of indoor air quality, Int J Environ Res Public Health, 17, 2927 (DOI: 10.3390/ijerph17082927)

9. Schwarzenbach R. P., Egli T., Hofstetter T. B., von Gunten U., Wehrli B., (2010), Global water pollution and human health. Annu Rev Environ Resour, 35, 109–136 (DOI: 10.1146/annurev-environ-100809–125342)

10. Balseiro-Romero M., Baveye P. C., (2018), Soil pollution: A hidden danger beneath our feet. Front Environ Sci, 6, 130 (https://www.frontiersin.org/article/10.3389/fenvs.2018.00130)

11. Häggström M., (2014), WikiJournal of Medicine (DOI: 10.15347/wjm/2014.008)

12. Prüss-Ustün A., Wolf J., Corvalán C., Neville T., Bos R., et al., (2017), Diseases due to unhealthy environments: an updated estimate of the global burden of disease attributable to environmental determinants of health, J Public Health, 39, 464–475 (DOI: 10.1093/pubmed/fdw085)

13. Tchounwou P. B., Yedjou C. G., Patlolla A. K., Sutton D. J., (2012), Heavy metal toxicity and the environment, Exp Suppl, 101, 133–164 (DOI: 10.1007/978-3-7643-8340-4_6)

14. Driscoll C. T., Mason R. P., Chan H. M., Jacob D. J., Pirrone N., (2013), Mercury as a global pollutant: sources, pathways, and effects, Environ Sci Technol, 10, 4967–4983 (DOI: 10.1021/es305071v)

15. Streets D. G., Horowitz H. M., Jacob D. J., Lu Z., Levin L., et al., (2017), Total mercury released to the environment by human activities, Environ Sci Technol, 51, 5969–5977 (DOI: 10.1021/acs.est.7b00451)

16. Siddiqi Z. M., (2018), Transport and fate of mercury (Hg) in the environment: Need for continuous monitoring, Springer International Publishing, 20 (DOI: 10.1007/978-3-319-58538-3_56-

1)

17. Nurfatini B., Amir S., (2018), Recent advances in mercury detection; towards enabling a sensitive and rapid point-of-check measurement, J Toxicol Risk Assess, 4, 1–10 (DOI: 10.23937/2572-4061.1510010)

18. Rice K. M., Walker Jr E. M., Wu M., Gillette C., Blough E. R., (2014), Environmental mercury and its toxic effects, J Prev Med Public Health, 47, 74–83 (DOI: 10.3961/jpmph.2014.47.2.74)

19. Harada M., (1995), Minamata disease: Methylmercury poisoning in japan caused by environmental pollution. Crit Rev Toxicol, 25, 1–24 (DOI: 10.3109/10408449509089885)

20. Grandjean P., Weihe P., White R. F., Debes F., Araki S., et al., (1997), Cognitive deficit in 7-year-old children with prenatal exposure to methylmercury, Neurotoxicol Teratol, 19, 417–428 (DOI: https://doi.org/10.1016/S0892-0362(97)00097-4)

21. Braithwaite J., Mannion R., Matsuyama Y., Shekelle P. G., Whittaker S., et al., (2018), The future of health systems to 2030: A roadmap for global progress and sustainability, Int J Qual Heal Care, 30, 823–831 (DOI: 10.1093/intqhc/mzy242)

22. Jamison D. T., Laxminarayan R. (2017), Disease control priorities: improving health and reducing poverty, World bank Publications, (DOI: 10.1596/978-1-4648-0527-1)

23. Hathaway J., Maibach E. W., (2018), Health implications of climate change: A review of the literature about the perception of the public and health professionals, Curr Environ Heal, 5, 197–204 (DOI: 10.1007/s40572-018-0190-3)

24. Rohr J. R., Barrett C. B., Civitello D. J., Craft M. E., Delius B., et al., (2019), Emerging human infectious diseases and the links to

global food production, Nat Sustain, 2, 445–456 (DOI: 10.1038/s41893-019-0293-3)

25. Seymour V., (2016), The Human–nature relationship and its impact on health: A critical review, Front Public Heal, 4, 260 (DOI: 10.3389/fpubh.2016.00260)

26. Popp J., Lakner Z., Harangi-Rákos M., Fári M., (2014), The effect of bioenergy expansion: Food, energy, and environment. Renew Sustain Energy Rev, 32, 559–578 (DOI: 10.1016/j.rser.2014.01.056)

27. IEA, Annual energy outlook, (2012), (www.iea.org/reports/world-energy-outlook-2012)

28. Owusu P. A., Asumadu-Sarkodie S., (2016), A review of renewable energy sources, sustainability issues and climate change mitigation, Cogent Eng, 3, 1167990 (DOI: 10.1080/23311916.2016.1167990)

29. Hill J., Nelson E., Tilman D., Polasky S., Tiffany D., (2006), Environmental, economic, and energetic costs and benefits of biodiesel and ethanol biofuels, Proc Natl Acad Sci, 103, 11206 LP–11210 (DOI: 10.1073/pnas.0604600103)

30. Knothe G., Krahl J., Van Gerpen J. B. T.-T. B. H., (2010), Biodiesel production, Second eds, IAOCS Press, 31–96 (DOI: 10.1016/B978-1-893997-62-2.50009-7)

31. Leung D. Y. C., Wu X., Leung M. K. H., (2010), A review on biodiesel production using catalyzed transesterification, Appl Energy, 87, 1083–1095 (DOI: 10.1016/j.apenergy.2009.10.006)

32. Encinar J. M., González J. F., Rodríguez J. J., Tejedor A., (2002), Biodiesel fuels from vegetable oils: Transesterification of cynara cardunculus L. oils with ethanol, Energy & Fuels, 16, 443–450 (DOI: 10.1021/ef010174h)

33. Meher L. C., Sagar D. V., Naik S. N., (2006), Technical aspects of biodiesel production by transesterification — a review, Renew & Sust Ener Revie 10, 248–268 (DOI: 10.1016/j.rser.2004.09.002)

34. Paterson B., Cowie C. E., Jackson P. E., (1996), Determination of phenols in environmental waters using liquid chromatography with electrochemical detection, J Chromatogr A, 731, 95–102 (DOI: 10.1016/0021-9673(95)01192-7)

35. Hussain C. M., Keçili R., (2020), Spectroscopic Techniques for Environmental Analysis, Elsevier, 6, 133–161 (DOI: 10.1016/B978-0-12-816934-6.00006-0)

36. Hussain C. M., Keçili R. (2020), Quality assurance and control for environmental analysis, Elsevier, 12, 323–341. (DOI: 10.1016/B978-0-12-816934-6.00012-6)

37. Cedillo-Pozos A., Ternovoy S. K., Roldan-Valadez E., (2020), Imaging methods used in the assessment of environmental disease networks: A brief review for clinicians, Insights Imaging, 11, 18 (DOI: 10.1186/s13244-019-0814-7)

38. Prado Bert P., Mercader E. M. H., Pujol J., Sunyer J., Mortamais M., (2018), The effects of air pollution on the brain: A review of studies interfacing environmental epidemiology and neuroimaging, Curr Environ Heal reports, 5, 351–364 (DOI: 10.1007/s40572-018-0209-9)

39. Roco M. C., Mirkin C. A., Hersam M. C., (2011), Nanotechnology research directions for societal needs in 2020: Summary of international study, J Nanoparticle Res, 13, 897–919 (DOI: 10.1007/s11051-011-0275-5)

40. Kanwar R., Rathee J., Salunke D. B., Mehta S. K., (2019), Green nanotechnology-driven drug delivery assemblies, ACS Omega, 4,

8804–8815 (DOI: 10.1021/acsomega.9b00304)

41. Mady M. F., Kelland M. A., (2020), Review of nanotechnology impacts on oilfield scale management, ACS Appl Nano Mater, 3, 7343–7364 (DOI: 10.1021/acsanm.0c01391)

42. Shevchenko D. V. T. and E. V., (2016), Introduction: Nanoparticle chemistry, Chem Rev, 116, 10343–10345 (DOI: 10.1021/acs.chemrev.6b00566)

43. Kagan C. R., Fernandez L. E., Gogotsi Y., Hammond P. T., Hersam M. C., et al., (2016), Nano day: Celebrating the next decade of nanoscience and nanotechnology, ACS Nano, 10, 9093–9103 (DOI: 10.1021/acsnano.6b06655)

44. Bayda S., Adeel M., Tuccinardi T., Cordani M., Rizzolio F., (2019), The history of nanoscience and nanotechnology: From chemical-physical applications to nanomedicine, Molecules, 25, 112 (DOI: 10.3390/molecules25010112)

45. Kumar N., Sinha Ray S., (2007), Synthesis and functionalization of nanomaterials processing of polymer-based nanocomposites, Springer International Publishing, 15–55. (DOI: 10.1007/978-3-319-97779-9_2)

46. Moku G., Gopalsamuthiram V. R., Hoye T. R., Panyam J., (2019), Surface modification of nanoparticles: Methods and applications, Surf Modif Polym, 31, 317–346 (DOI: 10.1002/9783527819249.ch11)

47. Lowry G. V, Gregory K. B., Apte S. C., Lead J. R., (2012), Transformations of nanomaterials in the environment, Environ Sci Technol, 46, 6893-6899 (DOI: 10.1021/es300839e)

48. Gao Z., Qin Y., (2017), Design and properties of confined nanocatalysts by atomic layer deposition. Acc Chem Res, 50, 2309–

2316 (DOI: 10.1021/acs.accounts.7b00266)

49. Prinsen P., Luque R., (2019), Nanoparticle design and characterization for catalytic applications in sustainable chemistry. RSC, 1, 1–36. (DOI: 10.1039/9781788016292-00001)

50. El-Safty S. A., Shenashen M. A., El-Safty S. A., (2012), Mercury-ion optical sensors, TrAC Trends Anal Chem, 38, 98–115 (DOI: 10.1016/j.trac.2012.05.002)

51. Dai D., Yang J., Wang Y., Yang Y.-W., (2020), Recent progress in functional materials for selective detection and removal of mercury(II) ions, Adv Funct Mater, 31, 2006168 (DOI: 10.1002/adfm.202006168)

52. Liu T., Chu Z., Jin W., (2019), Electrochemical mercury biosensors based on advanced nanomaterials, J Mater Chem B, 7, 3620–3632 (DOI: 10.1039/C9TB00418A)

53. Yang J., Hou B., Wang J., Tian B., Bi J., et al., (2019), Nanomaterials for the removal of heavy metals from wastewater. Nanomater , 9, 1–12, (DOI: 10.3390/nano9030424)

54. Willner M. R., Vikesland P. J., (2018), Nanomaterial enabled sensors for environmental contaminants, J Nanobiotechnology, 16, 95 (DOI: 10.1186/s12951-018-0419-1)

55. De Crozals G., Bonnet R., Farre C., Chaix C., (2016), Nanoparticles with multiple properties for biomedical applications: A strategic guide, Nano Today, 11, 435–463 (DOI: 10.1016/j.nantod.2016.07.002)

56. Gagner J. E., Shrivastava S., Qian X., Dordick J. S., Siegel R. W., (2012), Engineering nanomaterials for biomedical applications requires understanding the nano-bio interface: A perspective, J Phys Chem Lett, 3, 3149–3158 (DOI: 10.1021/jz301253s)

57. Ramos A. P., Cruz M. A. E., Tovani C. B., Ciancaglini P., (2017), Biomedical applications of nanotechnology, Biophys Rev, 9, 79–89 (DOI: 10.1007/s12551-016-0246-2)

58. Kim D., Kim J., Park Y. Il, Lee N., Hyeon T., (2018), Recent development of inorganic nanoparticles for biomedical imaging, ACS Cent Sci, 4, 324–336 (DOI: 10.1021/acscentsci.7b00574)

59. Duan C., Liang L., Li L., Zhang R., Xu Z. P., (2018), Recent progress in upconversion luminescence nanomaterials for biomedical applications, J Mater Chem B, 6, 192–209 (DOI: 10.1039/C7TB02527K)

60. Parak W. J., Manna L., Nann T., (2010), Fundamental principles of quantum dots, Nanotechnology, 2010, 73–96 (DOI: 10.1002/9783527628155.nanotech004)

61. Nanda K. K., Kruis F. E., Fissan H., (2001), Energy levels in embedded semiconductor nanoparticles and nanowires, Nano Lett, 1, 605–611 (DOI: 10.1021/nl0100318)

62. Rabouw F. T., de Mello Donega C., (2016), Excited-state dynamics in colloidal semiconductor nanocrystals, Top Curr Chem, 374, 58 (DOI: 10.1007/s41061-016-0060-0)

63. Kumar C. S. S. R., (2010), Semiconductor nanomaterials, Wiley, 6, (ISBN: 978-3-527-32166-7)

64. Qi K., Selvaraj R., Wang L., (2020), Functionalized inorganic semiconductor nanomaterials: Characterization, properties, and applications, Front Chem, 8, 1085 (DOI: 10.3389/fchem.2020.616728)

65. Jolivet J.-P., Cassaignon S., Chanéac C., Chiche D., Durupthy O., et al., (2010), Design of metal oxide nanoparticles: Control of size, shape, crystalline structure and functionalization by aqueous

chemistry, Comptes Rendus Chim, 13, 40–51 (DOI: 10.1016/j.crci.2009.09.012)

66. Jun Y., Choi J., Cheon J., (2006), Shape control of semiconductor and metal oxide nanocrystals through nonhydrolytic colloidal routes, Angew Chemie Int Ed, 45, 3414–3439 (DOI: 10.1002/anie.200503821)

67. Lewicka Z. A., Yu W. W., Oliva B. L., Contreras E. Q., Colvin V. L., (2013), Photochemical behavior of nanoscale TiO_2 and zno sunscreen ingredients, J Photochem Photobiol A Chem, 263, 24–33 (DOI: 10.1016/j.jphotochem.2013.04.019)

68. Collins T. C., Hauenstein R. J., (2011), Fundamental properties of ZnO mater electron optoelectron device applications, Wiley, 25, 1–28 (DOI: 10.1002/9781119991038.ch1)

69. Zhang Y., Nayak T. R., Hong H., Cai W., (2013), Biomedical applications of zinc oxide nanomaterials, Curr Mol Med, 13, 1633–1645 (DOI: 10.2174/15665240130666131111130058)

70. Zhou H., Wu L., Wang H.-Q., Zheng J.-C., Zhang L., et al., (2017), Interfaces between hexagonal and cubic oxides and their structure alternatives, Nat Commun, 8, 1474 (DOI: 10.1038/s41467-017-01655-5)

71. Wang Z. L., (2004), Zinc oxide nanostructures: Growth, properties and applications, J Phys Condens Matter, 16, R829–R858 (DOI: 10.1088/0953-8984/16/25/r01)

72. Look D. C., (2001), Recent advances in ZnO materials and devices, Mater Sci Eng B, 80, 383–387 (DOI: 10.1016/S0921-5107(00)00604-8)

73. Geurts J., (2010), Crystal structure, chemical binding, and lattice properties of zinc oxide, Springer Berlin Heidelberg, 7–37 (DOI:

10.1007/978-3-642-10577-7_2)

74. Özgür Ü., Avrutin V., Morkoç H., (2018), Zinc oxide materials and devices grown by molecular beam epitaxy, Elsevier, 16, 343–375 (DOI: 10.1016/B978-0-12-812136-8.00016-5)

75. Srikant V., Clarke D. R., (1998), On the optical band gap of zinc oxide, J Appl Phys, 83, 5447–5451 (DOI: 10.1063/1.367375)

76. Djurišić A. B., Ng A. M. C., Chen X. Y., (2010), ZnO nanostructures for optoelectronics: Material properties and device applications, Prog Quantum Electron, 34, 191–259 (DOI: 10.1016/j.pquantelec.2010.04.001)

77. Zhu P., Weng Z., Li X., Liu X., Wu S., et al., (2016), Biomedical applications of functionalized ZnO nanomaterials: From biosensors to bioimaging, Adv Mater Interfaces, 3, 1500494 (DOI: 10.1002/admi.201500494)

78. Kamarulzaman N., Kasim M. F., Rusdi R., (2015), Band gap narrowing and widening of ZnO nanostructures and doped materials, Nanoscale Res Lett, 10, 346 (DOI: 10.1186/s11671-015-1034-9)

79. Lee J., Sorescu D. C., Deng X., (2016), Tunable lattice constant and band gap of single- and few-layer ZnO, J Phys Chem Lett, 7, 1335–1340 (DOI: 10.1021/acs.jpclett.6b00432)

80. Pawar V., Jha P. K., Panda S. K., Jha P. A., Singh P., (2018), Band-gap engineering in zno thin films: A combined experimental and theoretical study, Phys Rev Appl, 9, 54001 (DOI: 10.1103/PhysRevApplied.9.054001)

81. Liu L., Mei Z., Tang A., Azarov A., Kuznetsov A., et al., (2016), Oxygen vacancies: The origin of n-type conductivity in ZnO, Phys Rev B, 93, 235305 (DOI: 10.1103/PhysRevB.93.235305)

82. Gai Y., Tang G., (2014), Effects of hydrostatic pressures on the ionization and formation energies of dopants in ZnO and ZnTe, Phys Lett A, 378, 82–85 (DOI: 10.1016/j.physleta.2013.10.041)

83. Kennedy J., Markwitz A., Li Z., Gao W., Kendrick C., et al., (2006), Modification of electrical conductivity in RF magnetron sputtered zno films by low-energy hydrogen ion implantation, Curr Appl Phys, 6, 495–498 (DOI: 10.1016/j.cap.2005.11.046)

84. Schmidt-Mende L., MacManus-Driscoll J. L., (2007), ZnO–nanostructures, defects, and devices, Mater Today, 10, 40–48 (DOI: 10.1016/S1369-7021(07)70078-0)

85. Sahal M., Mollar M., Marí B. (2016), p- and n-Type Doping of zinc oxide through electrochemical methods, IRSEC conference, 2016, 11–15. (DOI: 10.1109/IRSEC.2016.7984057)

86. Ellmer K., Bikowski A., (2016), Intrinsic and extrinsic doping of ZnO and ZnO alloys, J Phys D Appl Phys, 49, 413002 (DOI: 10.1088/0022-3727/49/41/413002)

87. Norton D. P., Heo Y. W., Ivill M. P., Ip K., Pearton S. J., et al., (2004), ZnO: Growth, doping & processing, Mater Today, 7, 34–40 (DOI: 10.1016/S1369-7021(04)00287-1)

88. Morkoç H., Özgür H. M. Ü., (2009), Doping of ZnO, Zinc oxide: fundamentals, materials and device technology, Wiley, 14, 245–275 (DOI: 10.1002/9783527623945.ch4)

89. Thomas M. A., Cui J. B., (2010), Electrochemical route to p-type doping of ZnO nanowires, J Phys Chem Lett, 1, 1090–1094 (DOI: 10.1021/jz100246e)

90. Monfort O., Plesch G., (2018), Bismuth vanadate-based semiconductor photocatalysts: A short critical review on the efficiency and the mechanism of photodegradation of organic

pollutants, Environ Sci Pollut Res, 25, 19362–19379 (DOI: 10.1007/s11356-018-2437-9)

91. McCluskey M. D., Jokela S. J., (2009), Defects in ZnO, J Appl Phys, 106, 71101 (DOI: 10.1063/1.3216464)

92. Przezdziecka E., Guziewicz E., Jarosz D., Snigurenko D., Sulich A., et al., (2020), Influence of oxygen-rich and zinc-rich conditions on donor and acceptor states and conductivity mechanism of ZnO films grown by ald—experimental studies, J Appl Phys, 127, 75104 (DOI: 10.1063/1.5120355)

93. Al-Hilli S., Willander M., (2009), The pH response and sensing mechanism of n-type ZnO/electrolyte interfaces, Sensors, 9, 7445–7480 (DOI: 10.3390/s90907445)

94. Janotti A., Van de Walle C. G., (2011), Native point defects and doping in ZnO, Zinc oxide materials electron optoelectron device applications, Wiley, 2011, 113–134 (DOI: 10.1002/9781119991038.ch5)

95. He H., Yang Q., Liu C., Sun L., Ye Z., (2011), Size-dependent surface effects on the photoluminescence in ZnO nanorods, J Phys Chem C, 115, 58–64 (DOI: 10.1021/jp106990a)

96. Samavati A., Samavati Z., Ismail A. F., Othman M. H. D., Rahman M. A., et al., (2017), Structural, optical and electrical evolution of al and Ga co-doped ZnO/SiO_2/glass thin film: Role of laser power density, RSC Adv, 7, 35858–35868 (DOI: 10.1039/C7RA04963C)

97. Alvi N. H., ul Hasan K., Nur O., Willander M., (2011), The origin of the red emission in n-ZnO nanotubes/p-GaN white light emitting diodes, Nanoscale Res Lett, 6, 1–7 (DOI: 10.1186/1556-276X-6-130)

98. Vempati S., Mitra J., Dawson P., (2012), One-step synthesis of ZnO

nanosheets: A blue-white fluorophore, Nanoscale Res Lett, 7, 1–10 (DOI: 10.1186/1556-276X-7-470)

99. Kumar S. G., Rao K. S. R. K., (2015), Zinc oxide based photocatalysis: Tailoring surface-bulk structure and related interfacial charge carrier dynamics for better environmental applications, RSC Adv, 5, 3306–3351 (DOI: 10.1039/C4RA13299H)

100. Sun Y., Chen L., Bao Y., Zhang Y., Wang J., et al., (2016), The applications of morphology controlled ZnO in catalysis, Catalyst, 5, 3306–3351 (DOI: 10.3390/catal6120188)

101. Habibi D., Nasrollahzadeh M., (2012), ZnO as an effective and reusable heterogeneous catalyst for the synthesis of arylaminotetrazoles, Synth Commun, 42, 2023–2032 (DOI: 10.1080/00397911.2010.548620)

102. Toulhoat H., (2010), Heterogeneous catalysis: Use of density functional theory, Elsevier, 2010, 1–7. (DOI: 10.1016/B978-008043152-9.02243-0)

103. Semwal S., Arora A. K., Badoni R. P., Tuli D. K., (2011), Biodiesel production using heterogeneous catalysts, Bioresour Technol, 102, 2151–2161 (DOI: 10.1016/j.biortech.2010.10.080)

104. Liu M.-H., Chen Y.-W., Liu X., Kuo J.-L., Chu M.-W., et al., (2016), Defect-mediated gold substitution doping in ZnO mesocrystals and catalysis in CO oxidation, ACS Catal, 6, 115–122 (DOI: 10.1021/acscatal.5b02093)

105. Eixenberger J. E., Anders C. B., Wada K., Reddy K. M., Brown R. J., et al., (2019), Defect engineering of ZnO nanoparticles for bioimaging applications, ACS Appl Mater Interfaces, 11, 24933–24944 (DOI: 10.1021/acsami.9b01582)

106. Liu D., Lv Y., Zhang M., Liu Y., Zhu Y., et al., (2014), Defect-related photoluminescence and photocatalytic properties of porous zno nanosheets, J Mater Chem A, 2, 15377–15388 (DOI: 10.1039/C4TA02678K)

107. Xie W., Yang Z., Chun H., (2007), Catalytic properties of lithium-doped ZnO catalysts used for biodiesel preparations, Ind Eng Chem Res, 46, 7942–7949 (DOI: 10.1021/ie070597s)

108. Tulus, Olthof S., Marszalek M., Peukert A., Muscarella L. A., et al., (2019), Control of surface defects in ZnO nanorod arrays with thermally deposited au nanoparticles for perovskite photovoltaics, ACS Appl Energy Mater, 2, 3736–3748 (DOI: 10.1021/acsaem.9b00452)

109. Catellani A., Ruini A., Calzolari A., (2015), Optoelectronic properties and color chemistry of native point defects in Al:ZnO transparent conductive oxide. J Mater Chem C, 3, 8419–8424 (DOI: 10.1039/C5TC01699A)

110. Raghavendra A. J., Gregory W. E., Slonecki T. J., Dong Y., Persaud I., et al., (2018), Three-photon imaging using defect-induced photoluminescence in biocompatible ZnO nanoparticles, Int J Nanomedicine, 13, 4283–4290 (DOI: 10.2147/IJN.S165201)

111. Centonze V. E., White J. G., (1998), Multiphoton excitation provides optical sections from deeper within scattering specimens than confocal imaging, Biophys J, 75, 2015–2024 (DOI: 10.1016/S0006-3495(98)77643-X)

112. Buyanova I. A., Chen W. M., (2018), Photon upconversion promoted by defects, Low-dimensional semiconductor nanostructures, Woodhead Publishing, 7, 189–210. (DOI: 10.1016/B978-0-08-102053-1.00007-7)

113. Suyver J. F., Grimm J., van Veen M. K., Biner D., Krämer K. W., et al., (2006), Upconversion spectroscopy and properties of $NaYF_4$ doped with Er^{3+}, Tm^{3+} and/or Yb^{3+}, J Lumin, 117, 1–12 (DOI: 10.1016/j.jlumin.2005.03.011)

114. Makarov N. S., Lin Q., Pietryga J. M., Robel I., Klimov V. I., (2016), Auger up-conversion of low-intensity infrared light in engineered quantum dots, ACS Nano, 10, 10829–10841 (DOI: 10.1021/acsnano.6b04928)

115. Chen S. L., Stehr J., Reddy N. K., Tu C. W., Chen W. M., et al., (2012), Efficient upconversion of photoluminescence via two-photon absorption in bulk and nanorod ZnO, Appl Phys B Lasers Opt, 108, 919–924 (DOI: 10.1007/s00340-012-5138-y)

116. Asahi S., Teranishi H., Kusaki K., Kaizu T., Kita T., (2017), Two-step photon up-conversion solar cells. Nat Commun, 8, 14962 (DOI: 10.1038/ncomms14962)

117. Ye C., Zhou L., Wang X., Liang Z., (2016), Photon upconversion: from two-photon absorption (TPA) to triplet–triplet annihilation (TTA), Phys Chem Chem Phys, 18, 10818–10835 (DOI: 10.1039/C5CP07296D)

118. Layek A., Banerjee S., Manna B., Chowdhury A., (2016), Synthesis of rare-earth doped ZnO nanorods and their defect-dopant correlated enhanced visible-orange luminescence, RSC Adv, 6, 35892–35900 (DOI: 10.1039/c6ra02278b)

119. Majeed A., Javed F., Akhtar S., Saleem U., Anwar F., et al. (2020), Green synthesized selenium doped zinc oxide nano-antibiotic: Synthesis, characterization and evaluation of antimicrobial, nanotoxicity and teratogenicity potential, J Mater Chem B, 8, 8444–8458 (DOI: 10.1039/D0TB01553A)

120. Nenavathu B. P., Krishna Rao A. V. R., Goyal A., Kapoor A., Dutta R. K., (2013), Synthesis, characterization and enhanced photocatalytic degradation efficiency of Se doped ZnO nanoparticles using trypan blue as a model dye, Appl Catal A Gen, 459, 106–113 (DOI: 10.1016/j.apcata.2013.04.001)

121. Nenavathu B. P., Sharma A., Dutta R. K., (2018), Se doped ZnO nanoparticles with improved catalytic activity in degradation of cholesterol, 3, 289–300 (DOI: 10.22090/jwent.2018.04.002)

Chapter 2

Role of oxygen defects in the basicity of Se doped ZnO nanocatalyst for enhanced triglyceride transesterification in biodiesel production

2.1 Introduction

Unlike other living organisms, human beings have a desire to improve the quality of life. This inherent instinct has caused an unimaginable explosion of life amenities, lifestyle changes, improved living standards, and life expectancy. Energy resources are required to fulfill the ever-increasing human needs and to maintain a safe and clean ecosystem. Understanding the necessity and adapting to current energy changes has led to maintaining a global energy outlook.

International energy outlook forecasts that the marketed global energy consumption will rapidly increase through 2050 on an average for all fuels. Much of the world energy demand increases with economic growth, structural transformations, and growing populations, which will actively contribute to total world energy utilization [1]. Due to the depletion of non-renewable energy resource-based fuels and ever-increasing energy demand, unconventional renewable energy sources have attracted attention [2]. Several alternative renewable energy resources such as solar, wind, geothermal, hydroelectric and biomass are widely used, but still, they are in the developmental stage due to limiting environmental factors. Biodiesel production has increased rapidly in recent times, making it one of the fastest-growing sustainable clean and green renewable energy sources closer to realization to meet future energy demands [3].

Biodiesel, defined as a mixture of fatty acid methyl esters (FAME), produced from transesterification, yields high-quality biofuel due to its facile synthesis, continuous process, and low cost of production that meets

biodiesel fuel standards [4]. Biodiesel, produced by transesterification, is becoming an appealing biofuel in many countries across the world due to its high energy balance and reduced greenhouse gas emissions compared to other alternative fuels.

Transesterification of oils with methanol produces renewable, biodegradable, and non-toxic biodiesel in the presence of suitable acid, base, or enzyme catalysts [5–7]. For commercial biodiesel production, homogeneous acid (sulfuric, phosphoric, hydrochloric, and organic sulfonic acids) and base (NaOH, KOH, and sodium methoxide) catalysts are commonly employed [8]. Despite the higher activity and cost-effectiveness of homogenous catalyst in industries, the biofuel recovery remains challenging in biodiesel production due to complicated saponification and neutralization procedures. Therefore, heterogeneous catalysts are economically feasible for biodiesel production due to simplified purification, easy separation, and catalyst reusability in batch and continuous processes [9,10]. Moreover, the heterogeneous base catalysts show better catalytic activity than heterogeneous acid catalysts in transesterification reactions because of the formation of strongly alkaline alkoxide ion on the solid surface [7,11]. On top of that, nanocatalyst attracted much attention due to their relatively high surface to volume ratio, basic strength, and low solubility in methanol.

One of the most important challenges of the 21st century is the use of engineered nanomaterial properties in the design and development of new catalysts for sustainable and renewable energy production processes [12,13]. Nanocatalysts have a high surface to volume ratio and more reactive sites on the catalyst surface, leading to high catalytic efficiency. Among the most studied nanocatalysts, metal oxides, pure alkaline earth metal oxides, and their mixed metal oxide nanomaterials offer interesting catalytic activity in transesterification, but leaching of Ca^{+2} and Mg^{+2} ion limit their catalytic reusability [14–16] Recently, alkali metal (Li, Na, K

and Cs) doped alkaline earth metal oxides have also been investigated for transesterification, with their enhanced basicity attributed to the substitution of lattice M^{2+} ion with M^{+} alkali cation that leads to the formation of oxygen vacancy defect centers [17,18]. Transition metal oxides like ZnO, TiO_2, and other composite materials have low solubility, and hence their application in transesterification of oils may solve the problem associated with the leaching of metal ions [19,20].

ZnO is reported as stable, reusable, eco-friendly, and functions as an active heterogeneous catalyst in various catalytic reactions. Chemically, ZnO nanocatalyst has higher selectivity toward monoglycerides due to its amphoteric (Zn^{2+}: acidic sites and O^{2-}: basic sites) nature in the transesterification reaction. Therefore, ZnO based materials (nanoparticles, nanorods, doped ZnO) are used for transesterification reactions [21–25]. However, its increased basicity may improve its reactivity towards triglycerides as well [26]. Furthermore, it has been established that ZnO shows superior catalytic activity in transesterification reaction when basicity is enhanced either intrinsically or by doping with appropriate metals [27,28]. In addition to that, Se and Se based materials tune optoelectronic properties by the genesis of surface defects in the crystal structure of nanomaterials [29–31].

Therefore, in this chapter, selenium metal doping (Se) into ZnO to fine-tune surface defects and enhance catalytic activity in the transesterification reaction are described. The surface defects play an essential role in generating surface-active base sites involved in the catalytic conversion of oil to FAME. Se metal, with its natural anti-oxidative properties has also been used to improve the quality of biodiesel by enhancing its oxidative stability [32]. Overall, it would be of great interest to develop a new heterogeneous base catalyst that could be used to improve the economic production of biodiesel in an industrial process.

2.2 Results and Discussion

2.2.1 Nanocatalyst characterization

XRD diffraction studies of Se doped ZnO and ZnO NRs were carried out to investigate the effect of doping on the crystal structure, and these are well aligned with ZnO hexagonal wurtzite phase, as shown in **Figure 2.1a**. The decreased XRD intensity in Se doped ZnO sample in comparison to ZnO sample without any traces of additional peaks confirms the incorporation of Se into ZnO crystal lattice. The Se doped ZnO showed photoluminescence emission compared to undoped ZnO, as shown in **Figure 2.1b**. The PL is due to the presence of defects in the Se doped ZnO nanorods. A detailed characterization of Se doped ZnO sample for Se incorporation, defects generation, and optical properties by XRD, XPS and PL are described in chapter 3 and chapter 4 [31,33].

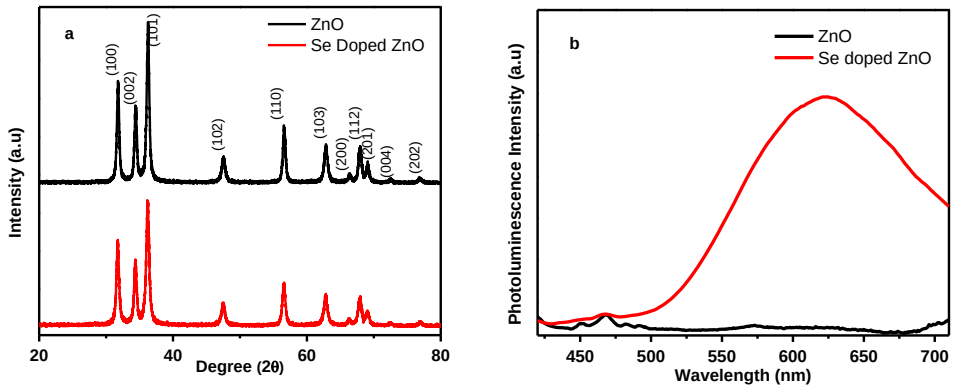

Figure 2.1 (a) XRD pattern and **(b)** PL spectrum of Se doped and undoped ZnO NRs

In brief, during the preparation of Se doped ZnO nanorods by a mechanothermal method, the selenium (Se) metal dopant, and annealing temperature plays an essential role in producing oxygen defects (V_O and O_i). During the preparation and annealing process, the Se incorporation into the crystal structure facilitates oxygen atom to dissociate from crystal lattice forming oxygen vacancy (V_O) and diffuse oxygen atom into

interstitial sites generating oxygen interstitial (O_i) defects due to the difference in the atomic size and charge compensation [31]. Simultaneously, during annealing, the oxygen molecule adsorbed on the surface dissociates and diffuses into interstitial sites of nanomaterial oxygen interstitial (O_i) defects. EPR spectroscopy studies were further carried out to obtain a better understanding of surface defects such as oxygen vacancies and oxygen interstitials in Se doped ZnO as shown in **Figure 2.2**. EPR spectrum ascertain g-factor values as g = 2.005 and g = 1.962 attributed to the presence of oxygen vacancy (V_o^+) and interstitial (O_i^-) defects in the crystal structure of the nanomaterial [34].

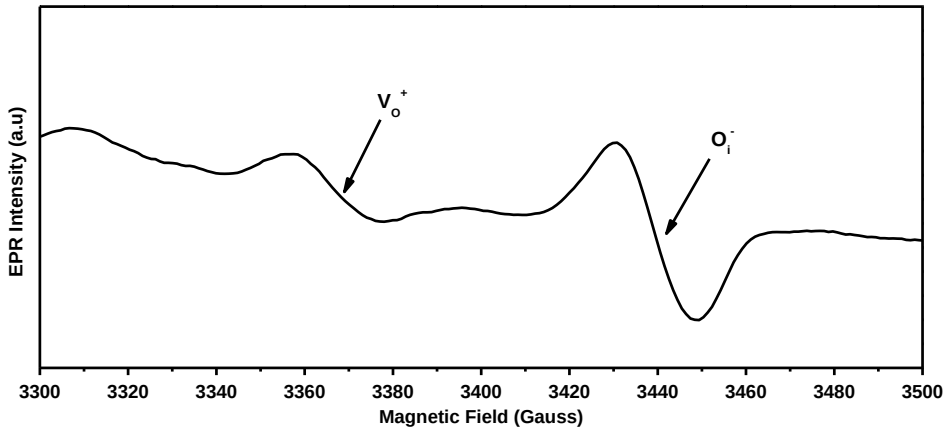

Figure 2.2 EPR spectrum of Se doped ZnO NRs show O_i and V_O defects

The morphology of Se doped ZnO NRs was analyzed using FE-SEM and HR-TEM, which confirms that Se doped ZnO nanoparticles self-assembled into a rod-shaped structure with an average diameter of 50 nm as shown in **Figures 2.3a** and **2.3b,** respectively [31]. Because of the formation of nanorods, the aspect ratio of the surface increases. Consequently, the absolute number of active basic sites increases in the NRs structure. These active sites in Se doped ZnO were used as a basic site to check the nanocatalyst activity in transesterification of triglycerides for biodiesel production.

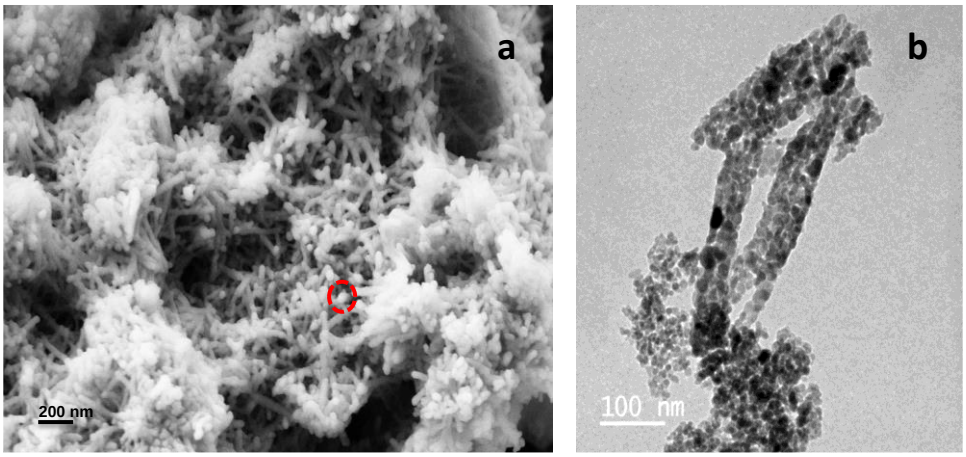

Figure 2.3 (a) FE-SEM and **(b)** HR-TEM images of Se doped ZnO NRs

2.2.2 Plausible mechanism of basicity in Se doped ZnO for biodiesel production

The impact of selenium doping on biodiesel production and its associated catalytic activity was estimated through defects enhanced basicity. The defects associated with V_o and O_i generate substantial surface basic sites in Se doped ZnO which are responsible for enhanced base catalytic activity leading to high FAME yield [28]. The formation of these basic sites was proposed to result from an electron transfer from Se metal to oxygen followed by ionization of Se atom. It is anticipated that the oxygen around zinc vacancies (V_{Zn}) and oxygen vacancies (V_o) leads to the formation of low coordination O^{2-} (strongly basic) sites. Moreover, oxygen interstitials (O_i) attracts considerable additional electron density from its nearest regular O^{2-} ions, which perhaps makes Se doped ZnO nanomaterial a base catalyst [35]. The delocalization of electrons released through defects formation induces an increased electronic density on Se doped ZnO, increasing their basicity [28]. Thus, it can be proposed that an optimum amount of selenium doping increases oxygen interstitials and vacancies with an increase in O^{2-} base sites that can help in proton abstraction from methanol to generate methoxide ion, which will be

stabilized by Zn^{2+} counterions. Next, the nucleophilic attack of methoxide ion at the ester carbonyl group of triglyceride (oil) generates a tetrahedral intermediate, from which fatty acid methyl ester and the corresponding oxyanion of the diglyceride are formed. The methoxide ion catalyst is regenerated by deprotonation of another molecule of methanol by the diglyceride oxyanion to begin another catalytic cycle. Eventually, diglycerides and monoglycerides are converted by the same transesterification mechanism to form respective FAME [36,37]. The proposed mechanism of transesterification of vegetable oil to fatty acid methyl esters over Se doped ZnO base catalyst is shown in **Scheme 2.1**.

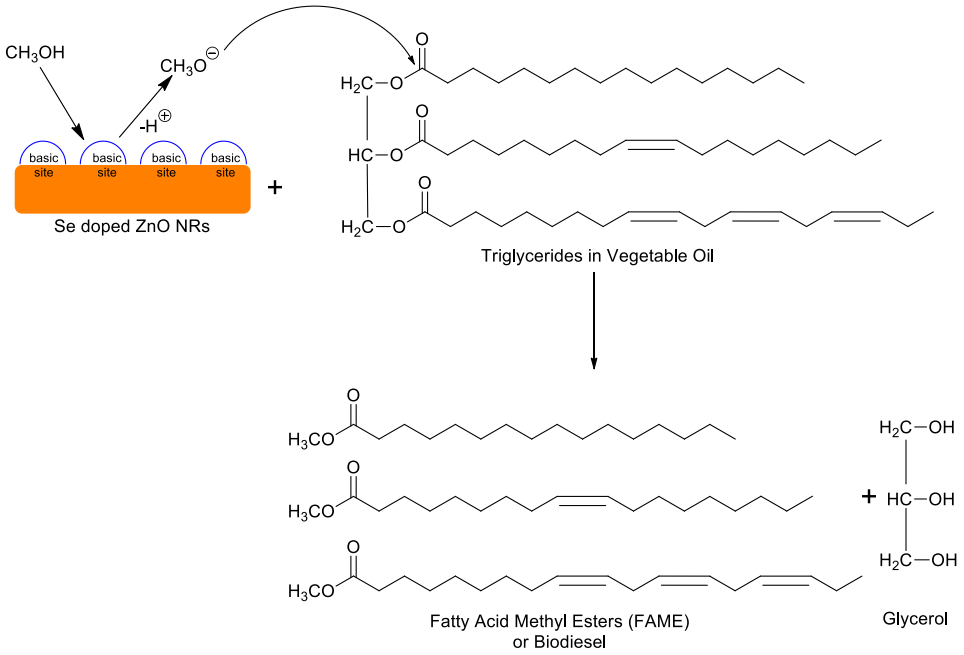

Scheme 2.1 Mechanism for transesterification of vegetable oil to form fatty acid methyl esters over Se doped ZnO base nanocatalyst

Se doped ZnO NRs were explored experimentally by performing vegetable oil (Composition is listed in **Table 2.1**) transesterification as a useful probe reaction to assess the heterogeneous catalytic performance towards biodiesel production.

Table 2.1 Fatty acid composition of sunflower oil

Common Name	IUPAC Name	Saturated/ Unsaturated	Notation
Palmitic Acid	Hexadecanoic acid	Saturated	C16:0
Stearic Acid	Octadecanoic acid	Saturated	C18:0
Oleic Acid	Octadec-9-enoic acid	Monounsaturated	C18:1
Linoleic Acid	9,12-Octadecadienoic acid	Polyunsaturated	C18:2
Behenic acid	Docosanoic acid	Saturated	C22:0

2.2.3 Optimization of transesterification reactions

2.2.3.1 Effect of reaction time

The effect of reaction time on the yield of biodiesel production using Se doped ZnO catalyst was estimated by variation of FAME conversion with respect to different reaction times (1, 3, 5, 7, and 10 h), keeping all other reaction parameters constant (reaction temperature, 65 °C; oil to methanol ratio, 1:20; catalyst load 5 wt.%). From **Figure 2.4a** (red-colored plot), it can be deduced that the conversion was very low (40.45%) during the first hour due to limited surface contact with oil and the presence of fewer mass transfer systems [38]. The reaction reaches a maximum yield of 94.7 % at 3 h and thereafter conversion of biodiesel reduced slightly for the reaction time of 5, 7, and 10 h with 80.4, 65.1, and 57.2 % FAME yields, respectively. A longer reaction time is required for better surface contact and mass transfer. On the contrary, yield decreases after 3 h owing to a reversible transesterification reaction [39]. According to these observations, 3 h reaction time was considered high FAME yielding

duration for optimization of other reaction parameters in biodiesel production.

2.2.3.2 Effect of reaction temperature

The influence of temperature on FAME yield was estimated at different temperatures (25, 45, 65, 85, and 105 °C) with a constant catalyst (5 wt.%) loading and oil to methanol (1:20) volume ratio. As indicated in **Figure 2.4b** (blue colored plot), the FAME yield of biodiesel had a considerable increase with increased temperature, resulting in a maximum yield of 94.7% at 65 °C. The transesterification reaction was partially complete at 25 °C and 45 °C with lower FAME yields of 33.6% and 43.8%, respectively. The low solubility and minimal diffusion rate of solvent into oil at lower temperatures provide a possible explanation for the experimental observation [40,41]. At 65 °C, the kinetic energy increases sufficiently to favor equilibrium shift in a forward direction in transesterification reaction, which eventually results in higher FAME yield. However, further increase in temperature to 85 °C and 105 °C was detrimental, resulting in lower FAME yields of 73.4% and 38.7%, respectively, mostly due to reduced methanol-oil contact. Hence, 65 °C was found to be the most favorable temperature for high conversion of triglycerides to FAME and employed as one of the most vital factors affecting biodiesel production.

2.2.3.3 Effect of methanol:oil volume ratio

The effect of methanol: oil volume ratio is another significant parameter that needs to be optimized to improve biodiesel production. The FAME yield was examined as a function of various methanol: oil volume ratio at 5 wt.% catalysts loading at 65 °C for 3 h as illustrated in **Figure 2.4c** (pink-colored plot). It was observed that the FAME yield was merely 28.2 and 43.6% with 5:1 and 10:1 methanol: oil volume ratio, respectively. According to our mechanistic explanation, methoxy anion at every

surface center drives the reaction in the forward direction. Higher methanol to oil ratio produces more reaction centers at the surface of the catalyst leading to a maximum FAME yield of 94.7% at 20:1 methanol: oil ratio [42]. However, further increase in methanol: oil volume (ratio of 30:1 and 40:1) poses a dilution effect resulting in lower yields of 73.87% and 62.98%, respectively. Hence, methanol to oil volume ratio of 20:1 was selected as optimum for better transesterification yield in further experiments.

2.2.3.4 Effect of catalyst loading

It was found that Se doped ZnO possesses basic surface sites, which makes them highly efficient in the catalytic process during transesterification reaction. The amount of Se doped ZnO catalyst loaded into the reaction mixture was varied from 0.5 to 10 wt.% by keeping other optimized parameters constant. It was found that the FAME yield increases (44.3, 49.9, 77.4, and 94.7%) significantly with an increase in the amount of catalyst loading (0.5, 1, 3, and 5 wt.%) and found to reach a maximum yield of 94.7% at 5 wt.% load of catalyst as shown in **Figure 2.4d** (orange-colored plot). This improved yield can be attributed to an increased number of available basic sites within the reaction system. However, increasing viscosity poses a challenge beyond this optimal catalytic load percentage, and the FAME yield decreased to 54.4% when 10 wt.% catalyst was used for the conversion reaction [43]. Therefore, in further experiments, 5 wt.% of selenium doped ZnO nanocatalyst was adopted as the optimum catalyst load required for efficient biodiesel production.

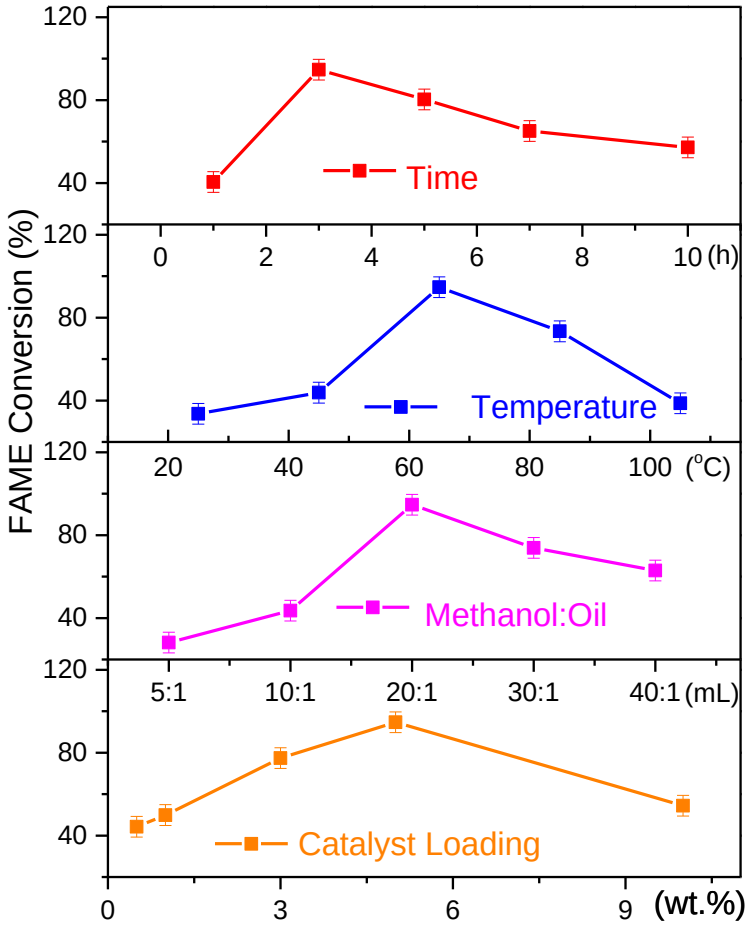

Figure 2.4 Influence of **(a**) reaction time, **(b)** reaction temperature, **(c)** methanol:oil volume ratio, and **(d)** catalyst load in the production of biodiesel or FAME

2.2.4 Control experiments

After obtaining excellent FAME yields with Se doped ZnO nanocatalyst under optimized reaction conditions in transesterification reaction, a series of control experiments were carried out to describe the superiority of our nanocatalyst. Undoped ZnO produced moderate FAME yields of 69.9% under optimized transesterification reaction conditions. In another essential control experiment, where no catalyst was employed, keeping all other reaction parameters constant, only a marginal FAME yield of 22% was observed (**Figure 2.5a**). The apparent enhancement in FAME yields

while using our nano-engineered catalyst can be chiefly attributed to the presence of defect generated basic sites in Se doped ZnO catalyst.

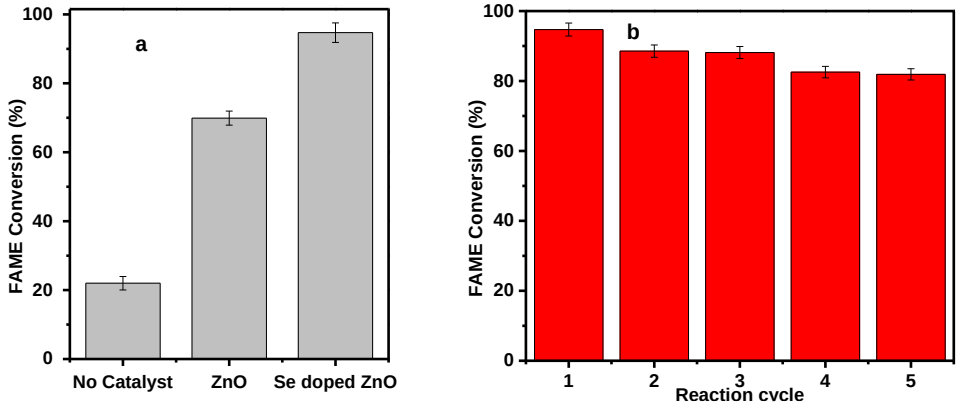

Figure 2.5 FAME production in **(a)** absence, presence of undoped ZnO, Se doped ZnO nanocatalysts, and **(b)** reusability of Se doped ZnO nanocatalyst

2.2.5 Nanocatalyst reusability

Catalyst reusability is one of the most important features of heterogeneous catalysts that offer advantages in industrial-scale biodiesel production. After the first cycle, the catalyst was collected and dried for examination in successive reaction cycles with fresh reactants every time under standard reaction conditions. The FAME yields, shown in **Figure 2.5b**, demonstrate that the yield was more than 80% in five consecutive cycles of reusability of the catalyst, suggesting that the reactivated heterogeneous catalyst's activity tends to remain stable and efficient in transesterification reactions.

2.2.6 GC-MS analysis of biodiesel

Gas Chromatography (GC) coupled with Mass Spectroscopy (MS) is a viable analytical method used to study fatty acid methyl esters. The chromatogram in **Figure 2.6** shows fatty acid methyl ester peaks which are compared and identified with the available NIST mass spectra library of fatty methyl esters. The FAME compositions obtained during biodiesel

production from vegetable oil using engineered Se doped ZnO nanocatalyst are listed and identified by GC-MS in **Table 2.2**. The maximum biodiesel obtained from vegetable oil using our nanocatalyst was confirmed by the presence of ~94.7% FAME and compared with those of literature methods, as shown in **Table 2.3**.

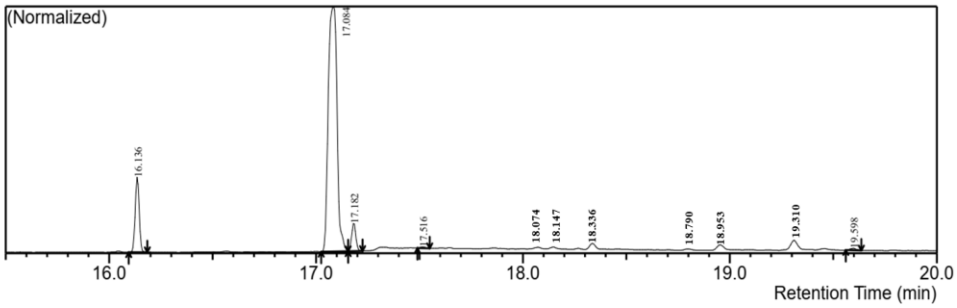

Figure 2.6 GC–MS chromatogram for FAME formation with optimized parameters in the presence of Se doped ZnO nanocatalyst

Table 2.2 FAME composition of biodiesel during transesterification of vegetable oil using Se doped ZnO nanocatalyst

Retention Time (min)	Common Name	C:D	% FAME
16.136	Palmitic acid methyl ester	C16:0	10.89
17.084	Oleic acid methyl ester	C18:1	77.96
17.182	Stearic acid methyl ester	C18:0	4.32
17.516	Linoleic acid methyl ester	C18:2	0.19
18.074	Cyclopropaneoctanoic acid, 2-hexyl-, methyl ester	C18:0	0.32
18.147	Cyclopentadecanone, 2-hydroxy	C15:0	0.36
18.336	14-Methyl-8-hexadecyn-1-ol	C17:1	1.20
18.790	Glyceryl trilinoleate	C57:6	0.15

18.953	Linoleic acid methyl ester	C18:2	1.20
19.310	14-Methyl-8-hexadecyn-1-ol	C17:1	2.25
19.598	Behenic acid methyl ester	C22:0	0.41

Table 2.3 Comparison of results between different catalytic systems

Catalyst	**Oil**	**Reaction Conditions**				**FAME (%)**	**Reference**
		Methanol: oil ratio	% wt. Catalyst	Temperature (^oC)	Time (h)		
Se doped ZnO	Sunflower	20:1	5	65	3	94.7	This work
Ag doped ZnO	Razma seeds	9:1	1.5	64	2	83	[24]
Ni doped ZnO	Castor	8:1	11	55	1	95.2	[22]
ZnO	Cocklebur crop seed	7:1	0.2	60	0.7	93.3	[23]
ZnO NRs	Olive	6:1	5	150	4	95	[21]
ZnO-TiO_2	Palm	6:1	2	60	5	92.2	[25]

2.3 Conclusion

The synthesized Se doped ZnO NRs with high surface area and defects generated basic sites are useful for enhanced heterogeneous nanocatalyst activity in biodiesel production from vegetable oil. A remarkable

improvement in FAME yield (94.7%) is attributed to the presence of oxygen defects induced basic sites in Se doped ZnO nanocatalyst. Moreover, the base catalyst was reused in five consecutive transesterification reaction cycles without any significant loss of FAME yield, which demonstrates that Se doped ZnO nanocatalyst is highly stable and active. Hence, our Se doped ZnO nanocatalyst has potential applications as a base nanocatalyst in large-scale biodiesel production.

2.4 Experimental section

2.4.1 Materials and methods

Zinc acetate dihydrate $Zn(CH_3COO)_2 \cdot 2H_2O$ and oxalic acid ($C_2H_2O_4$) were purchased from Merck Millipore, India. Selenium metal powder was procured from Acros Organics, India. Sunflower oil was obtained from Fortune foods, India. All other chemicals were used without further purification unless otherwise specified.

2.4.2 Synthesis of Se doped ZnO nanocatalyst

Se doped ZnO nanorods were synthesized by a mechanothermal method. In a typical synthesis, $Zn(CH_3COO)_2$ $2H_2O$ (0.685 g, 3.12 mmol) oxalic acid (0.472 g, 3.74 mmol) and 5 wt.% selenium (0.030 g, 0.39 mmol) mixture were ground for 20 min and subjected to heat treatment in a muffle furnace at 450 °C for 30 min. While preparing pure ZnO nanocatalyst, the same method was used without addition of Se metal into zinc acetate and oxalic acid mixture. The catalyst was washed with MQ water and ethanol for 4-5 times and dried in a hot air oven for overnight at 70 °C. Finally, samples were characterized by XRD, EPR, FE-SEM and PL spectrophotometry techniques.

2.4.3 Characterization of Se doped ZnO nanocatalyst

The morphology of Se doped ZnO was characterized by field emission scanning electron microscopy (FE-SEM). XRD patterns of Se doped and

undoped ZnO were recorded on a Rigaku Smart Lab, Automated Multipurpose X-ray Diffractometer with a Cu K_α source (the wavelength of X-ray was 1.541 Å). To further examine the defects in Se doped ZnO catalyst, X-band (frequency = 9.45 GHz) EPR spectra were analyzed by electron paramagnetic resonance (EPR) spectroscopy (Bruker) at room temperature. PL spectrum of ZnO and Se doped ZnO were obtained on a Fluoromax-4 Spectrofluorimeter (HORIBA Jobin Yvon, Model FM-100) with an excitation wavelength of 365 nm.

2.4.4 FAME production by using Se doped ZnO nanocatalyst

Transesterification reactions were carried out in a sealed round-bottom flask with constant stirring using a magnetic pellet. The desired amount of oil was transferred into a reaction vessel and was preheated to the required temperature followed by addition of required amount of nanocatalyst dispersed in dry methanol. The transesterification reaction was carried out by varying oil:methanol ratio (1:5, 1:10, 1:20, 1:30 and 1:40 v:v), catalyst load (0.5, 1, 3, 5 and 10 wt.%), temperature (25, 45, 65, 85 and 105 °C) and reaction time (1, 3, 5, 7 and 10 h). After the completion of the reaction, the catalyst was separated by centrifugation at 8000 rpm for 10 min. The solvent methanol was removed under reduced pressure, and the crude reaction mixture was dissolved in distilled hexane to quantify the FAME content by GC-MS analysis. The catalyst deactivated from each catalytic cycle was washed with hexane and acetone to remove residues and dried in a hot air oven at 70 °C for 10-12 h prior to use in successive cycles.

2.5 References

1. IEO (2019), International energy outlook (IEO) 2019 www.eia.gov/pressroom/presentations/capuano_07242018.pdf

2. Ellabban O., Abu-Rub H., Blaabjerg F. (2014), Renewable energy resources: Current status, future prospects and their enabling technology, Renew Sustain Energy Rev, 39, 748–764 (DOI: 10.1016/j.rser.2014.07.113)

3. Popp J., Lakner Z., Harangi-Rákos M., Fári M. (2014), The effect of bioenergy expansion: Food, energy, and environment. Renew Sustain Energy Rev, 32, 559–578 (DOI: 10.1016/j.rser.2014.01.056)

4. Abbaszaadeh A., Ghobadian B., Omidkhah M. R., Najafi G. (2012), Current biodiesel production technologies: A comparative review, Energy Convers Manag, 63, 138–148 (DOI: 10.1016/j.enconman.2012.02.027)

5. Avhad M. R., Marchetti J. M. (2016), Innovation in solid heterogeneous catalysis for the generation of economically viable and ecofriendly biodiesel: A review. Catal Rev - Sci Eng, 58, 157–208 (DOI: 10.1080/01614940.2015.1103594)

6. Rizwanul Fattah I. M., Ong H. C., Mahlia T. M. I., Mofijur M., Silitonga A. S., et al. (2020), State of the art of catalysts for biodiesel production, Front Energy Res, 8, 1–17 (DOI: 10.3389/fenrg.2020.00101)

7. Lam M. K., Lee K. T., Mohamed A. R. (2010), Homogeneous, heterogeneous and enzymatic catalysis for transesterification of high free fatty acid oil (waste cooking oil) to biodiesel: A review,. Biotechnol Adv, 28, 500–518 (DOI:

10.1016/j.biotechadv.2010.03.002)

8. Leung D. Y. C., Wu X., Leung M. K. H. (2010), A review on biodiesel production using catalyzed transesterification, Appl Energy, 87, 1083–1095 (DOI: 10.1016/j.apenergy.2009.10.006)

9. Lee A. F., Bennett J. A., Manayil J. C., Wilson K. (2014), Heterogeneous catalysis for sustainable biodiesel production *via* esterification and transesterification, Chem Soc Rev, 43, 7887–7916 (DOI: 10.1039/C4CS00189C)

10. Tran-Nguyen P. L., Ong L. K., Go A. W., Ju Y. H., Angkawijaya A. E. (2020), Non-catalytic and heterogeneous acid/base-catalyzed biodiesel production: recent and future developments, Asia-Pacific J Chem Eng, 15, (DOI: 10.1002/apj.2490)

11. Albuquerque M. C. G., Azevedo D. C. S., Cavalcante C. L., Santamaría-González J., Mérida-Robles J. M., et al. (2009), Transesterification of ethyl butyrate with methanol using MgO/CaO catalysts, J Mol Catal A Chem, 300, 19–24 (DOI: 10.1016/j.molcata.2008.10.033)

12. Ramsurn H., Gupta R. B. (2013), Nanotechnology in solar and biofuels, ACS Sustain Chem Eng, 1, 779–797 (DOI: 10.1021/sc400046y)

13. Akia M., Yazdani F., Motaee E., Han D., Arandiyan H. (2014), A review on conversion of biomass to biofuel by nanocatalysts. Biofuel Res J, 1, 16–25 (DOI: 10.18331/BRJ2015.1.1.5)

14. Chang F., Zhou Q., Pan H., Liu X. F., Zhang H., et al. (2014), Solid mixed-metal-oxide catalysts for biodiesel production: A review, Energy Technol, 2, 865–873 (DOI: 10.1002/ente.201402089)

15. Tahvildari K., Anaraki Y. N., Fazaeli R., Mirpanji S., Delrish E.

(2015), The study of CaO and MgO heterogenic nano-catalyst coupling on transesterification reaction efficacy in the production of biodiesel from recycled cooking oil, J Environ Heal Sci Eng, 13, 73 (DOI: 10.1186/s40201-015-0226-7)

16. Singh D., Bhoi R., Ganesh A., Mahajani S. (2014), Synthesis of biodiesel from vegetable oil using supported metal oxide catalysts, Energy & Fuels, 28, 2743–2753 (DOI: 10.1021/ef500045x)

17. Matsuhashi H., Oikawa M., Arata K. (2000), Formation of superbase sites on alkaline earth metal oxides by doping of alkali metals, Langmuir, 16, 8201–8205 (DOI: 10.1021/la000346n)

18. Montero J. M., Wilson K., Lee A. F. (2010), Cs promoted triglyceride transesterification over MgO nanocatalysts, Top Catal, 53, 737–745 (DOI: 10.1007/s11244-010-9461-4)

19. Singh A. K., Fernando S. D. (2008), Transesterification of soybean oil using heterogeneous catalysts, Energy & Fuels, 22, 2067–2069 (DOI: 10.1021/ef800072z)

20. Ikenaga K., Hamada A., Inoue T., Kusakabe K. (2017), Biodiesel production using metal oxide catalysts under microwave heating, Int Jour of Bio & Rene, 6, 23–26 (http://myjms.moe.gov.my/index.php/ijbr/article/view/4448)

21. Nambo A., Miralda C. M., Jasinski J. B., Carreon M. A. (2015), Methanolysis of olive oil for biodiesel synthesis over ZnO nanorods, React Kinet Mech Catal, 114, 583–595 (DOI: 10.1007/s11144-014-0802-3)

22. Baskar G., Aberna Ebenezer Selvakumari I., Aiswarya R. (2018), Biodiesel production from castor oil using heterogeneous Ni doped ZnO nanocatalyst, Bioresour Technol, 250, 793–798 (DOI:

10.1016/j.biortech.2017.12.010)

23. Ullah K., Jan H. A., Ahmad M., Ullah A. (2020), Synthesis and structural characterization of biofuel from cocklebur sp., using zinc oxide nano-particle: A novel energy crop for bioenergy industry, Front Bioeng Biotechnol, 8, 1–17 (DOI: 10.3389/fbioe.2020.00756)

24. Yadav L. S. R., Pratibha S., Manjunath K., Shivanna M., Ramakrishnappa T., et al. (2019), Green synthesis of Ag-ZnO nanoparticles: Structural analysis, hydrogen generation, formylation and biodiesel applications, J Sci Adv Mater Devices, 4, 425–431 (DOI: 10.1016/j.jsamd.2019.03.001)

25. Madhuvilakku R., Piraman S. (2013), Biodiesel synthesis by TiO_2–ZnO mixed oxide nanocatalyst catalyzed palm oil transesterification process, Bioresour Technol, 150, 55–59 (DOI: 10.1016/j.biortech.2013.09.087)

26. Ma H., Li S., Wang B., Wang R., Tian S. (2008), Transesterification of rapeseed oil for synthesizing biodiesel by K/KOH/γ-Al_2O_3 as heterogeneous base catalyst, J Am Oil Chem Soc, 85, 263–270 (DOI: 10.1007/s11746-007-1188-4)

27. Xie W., Yang Z., Chun H. (2007), Catalytic properties of lithium-doped ZnO catalysts used for biodiesel preparations, Ind Eng Chem Res, 24, 7942–7949 (DOI: 10.1021/ie070597s)

28. Drouilly C., Krafft J. M., Averseng F., Lauron-Pernot H., Bazer-Bachi D., et al. (2013), Role of oxygen vacancies in the basicity of ZnO: From the model methylbutynol conversion to the ethanol transformation application, Appl Catal A Gen, 453, 121–129 (DOI: 10.1016/j.apcata.2012.11.045)

29. Nenavathu B. P., Krishna Rao A. V. R., Goyal A., Kapoor A., Dutta

R. K. (2013), Synthesis, characterization and enhanced photocatalytic degradation efficiency of Se doped ZnO nanoparticles using trypan blue as a model dye, Appl Catal A Gen, 459, 106–113 (DOI: 10.1016/j.apcata.2013.04.001)

30. Qin J., Qiu G., Jian J., Zhou H., Yang L., et al. (2017), Controlled growth of a large-size 2D selenium nanosheet and its electronic and optoelectronic applications, ACS Nano, 11, 10222–10229 (DOI: 10.1021/acsnano.7b04786)

31. Rao A. V. R. K., Reddy R. B., Sengupta S., Chelvam V. (2018), Efficient ``turn-on'' nanosensor by dual emission-quenching mechanism of functionalized Se doped ZnO nanorods for mercury (II) detection, Appl. Nanosci. 8, 1973–1987 (DOI: 10.1007/s13204-018-0875-9)

32. Fallen B. D., Pantalone V. R., Sams C. E., Kopsell D. A., Vaughn S. F., et al. (2011), Effect of soybean oil fatty acid composition and selenium application on biodiesel properties, J Am Oil Chem Soc, 88, 1019–1028 (DOI: 10.1007/s11746-010-1746-z)

33. Rao A. V. R. K., Chelvam V. (2020), Defects induced multicolor down- and up-conversion fluorescence in Se doped ZnO nanorods by single wavelength excitation. Opt Mater, 107, 110122 (DOI: 10.1016/j.optmat.2020.110122)

34. Pöppl A., Völkel G. (1990), ESR and photo-ESR investigations of the V centre in ZnO raw material and Li-doped ZnO ceramic powder, Phys status solidi, 121, 195–204 (DOI: 10.1002/pssa.2211210123)

35. Brudevoll T., Kotomin E. (1996), Interstitial-oxygen-atom diffusion in MgO, Phys Rev B - Condens Matter Mater Phys, 53, 7731–7735 (DOI: 10.1103/PhysRevB.53.7731)

36. Lee D. W., Park Y. M., Lee K. Y. (2009), Heterogeneous base catalysts for transesterification in biodiesel synthesis, Catal Surv from Asia, 13, 63-77 (DOI: 10.1007/s10563-009-9068-6)

37. Schuchardt U., Sercheli R., Matheus R. (1998), Transesterification of vegetable oils : A review, J Braz Chem Soc, 9, 199–210 (DOI: 10.1590/S0103-50531998000300002)

38. Klaewkla R., Arend M., Hoelderich W. F. (2011), A review of mass transfer controlling the reaction rate in heterogeneous catalytic systems, Mass Transf - Adv Asp, 667–684 (DOI: 10.5772/22962)

39. Elkady M. F., Zaatout A., Balbaa O. (2015), Production of biodiesel from waste vegetable oil *via* KM micromixer, Journal of Chemistry 2015, 1–9 (DOI:10.1155/2015/63016)

40. Zhou H., Lu H., Liang B. (2006), Solubility of multicomponent systems in the biodiesel production by transesterification of jatropha curcas L . oil with methanol, J Chem Eng Data, 51, 1130–1135 (DOI: 10.1021/je0600294)

41. Meher L. C., Sagar D. V., Naik S. N. (2006), Technical aspects of biodiesel production by transesterification-A review, Renew Sust Energ Rev, 10, 248–268 (DOI: 10.1016/j.rser.2004.09.002)

42. Bo X., Guomin X., Lingfeng C., Ruiping W., Lijing G. (2007), Transesterification of palm oil with methanol to biodiesel over a KF/Al_2O_3 heterogeneous base catalyst, Energy & Fuels, 21, 3109–3112 (DOI: 10.1021/ef7005035)

43. Bilgin A., Gülüm M., Koyuncuoglu İ., Nac E., Cakmak A. (2015), Determination of transesterification reaction parameters giving the lowest viscosity waste cooking oil biodiesel, Procedia - Soc Behav Sci, 195, 2492–2500 (DOI: 10.1016/j.sbspro.2015.06.318)

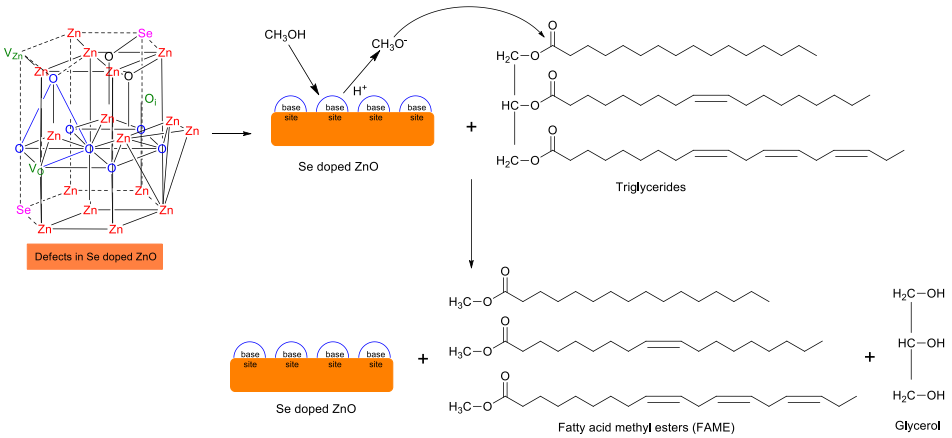

Schematic diagram showing mechanism of transesterification reaction by Se doped ZnO base nanocatalyst

Chapter 3

Efficient “turn-on” nanosensor by dual emission-quenching mechanism of functionalized Se doped ZnO nanorods for mercury (II) detection

3.1 Introduction

Environmental contamination is one of the critical concerns that the world is confronting today, and it is increasing with each passing year, leading to harmful effects. Heavy metals, particularly mercury is a toxic pollutant in trace amounts and exist in various forms as elemental, inorganic, and organic [1]. Mercury released from natural, anthropogenic and industrial sources has become a critical issue globally due to accumulation and toxic effects in the ecosystem [2,3]. Natural sources of mercury include volcanic eruptions, deposits of coal, and hydrothermal vents. Anthropogenic emissions contain mercury released from mining and fossil fuel combustion. Industrial sources of mercury include non-ferrous metals, cement, battery, and fluorescent lamp production [4]. These elevated levels of mercury are driven, in large part, by the long-range transport of mercury in the atmosphere. They may have significant adverse effects on humans and ecosystems. Persistent mercury substances enter into living organisms either directly or through the ecological food chain via bio-magnification, which is biologically dangerous even at low concentration [5,6].

Understanding the transport and effect of mercury in the ecosystem plays a crucial role in assessing present and future risks for humans and ecosystems. Exposure and accumulation of mercury and mercury-containing compounds in human continues to have adverse effects on nervous, cardiovascular, pulmonary, digestive, renal, and immune systems, thereby causing memory loss, tremors, impairment,

cardiomyopathy, visual, anemia, pulmonary fibrosis, abdominal pain, indigestion, tubular necrosis, allergic disease, and arthritis [7–9]. Hence there is an ever-growing demand to develop Hg^{2+} sensors that are simple, cost-effective, and rapid in detection to meet the required environmental health criteria of detection up to ~2 ppb. Traditional mercury detection analytical methods, including cold vapor atomic fluorescence spectrometry (CVAFS) [10], atomic fluorescence spectrometry[11], inductively coupled plasma mass spectrometry (ICP-MS) [12,13], gas chromatography (GC) [14] and nuclear magnetic resonance (NMR) [15,16] are highly expensive and requires multistep pre-treatment of samples which are labor-intensive for their realistic applications. Therefore, it is pertinent to develop facile, inexpensive, highly selective, and sensitive mercury-responsive nanosensors that could be used for environmental and biological applications.

In recent years, nanotechnology-based strategies have paid more attention to the development of novel nanosensors to detect Hg^{2+} ions. In general, fluorescence turn-on and turn-off probes, which exhibit fluorescence enhancement and quenching in the presence of Hg^{2+} ions, depends on size, shape, surface charge, electron transfer phenomenon, the interaction of mercury with functionalized nanomaterials, aggregation, and anti-aggregation properties. Metals [17,18], quantum dots [19,20], carbonaceous [21], upconversion [22], composite [23], and metal oxide [24,25] nanomaterials have been reported for mercury detection based on analyte induced emission or quenching PL. However, these nanomaterials-based methods are expensive and toxic to the environment. Therefore, semiconductor-based ZnO nanomaterials were very useful for detecting mercury present in the environment due to their ease of synthesis, non-toxicity, biocompatibility [26], chemical stability and appreciable tunable optical properties [27,28]. Doping and functionalization of nanomaterial formation play an important role in tuning optical signals by changing

surface properties and generating defects [29,30]. Doping is one of the simple and efficient methods for tuning morphology, band-gap, and charge carriers that enhance optoelectronic properties in ZnO nanomaterials for designing optical sensors. Doped ZnO-based nanomaterials for mercury detection have not been explored, even though few direct and indirect methods were already employed to detect mercury [31–33].

In our study, selenium metal is chosen because Se doped ZnO nanoparticles induce fluorescence emission by forming surface defect oxygen vacancies [34]. Earlier, selenium and selenium-based materials were also used for mercury capture and removal from the environment because of an extremely high binding affinity of selenium for mercury ions [35–37]. Although a few successful methods have been reported, it would be of great interest to develop new material for efficient and direct detection of Hg^{2+} ions in solutions with high sensitivity below the allowed permissible limit of ~2 ppb, which is practically very challenging in real-world applications. Therefore, in this chapter, 3-mercaptopropionic acid (MPA) functionalized Se-doped ZnO nanoprobe is proposed and described for the first time for detection of mercury by dual turn on-turn off fluorescence mechanism as shown in **Scheme 3.1**

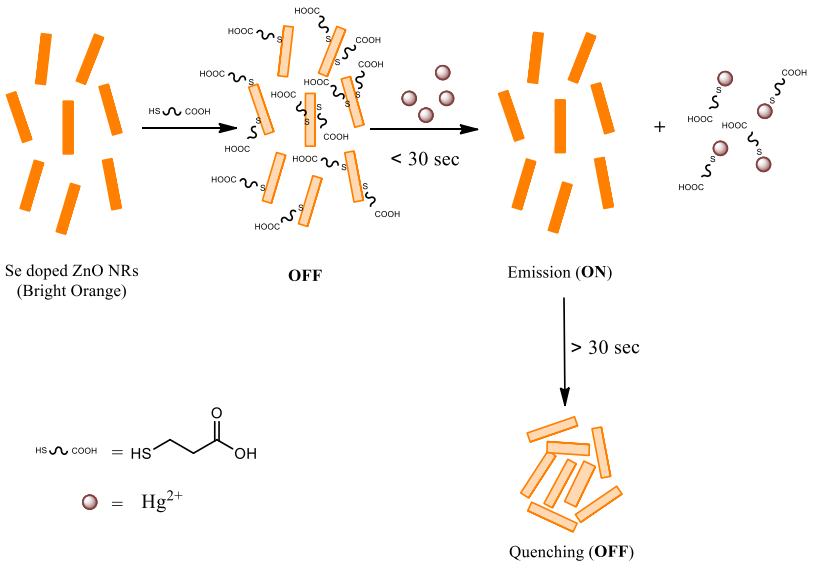

Scheme 3.1 A Schematic illustration of dual 'turn-on' and 'turn-off' mechanism of MPA functionalized Se doped ZnO nanoprobe for detection of Hg^{2+} ions

3.2 Results and Discussion

3.2.1 Characterization of Se doped ZnO

Examination of the XRD diffraction pattern of Se doped ZnO nanomaterials shows that XRD peak positions are similar to typical ZnO wurtzite structure (JCPDS card No: 5-0664). Also, it was found that the intensities of XRD peaks of differently doped ZnO with Se decrease slightly with an increase in % wt. of Se (1, 3, 5, and 10%) without the formation of any additional peaks, as shown in **Figure 3.1**.

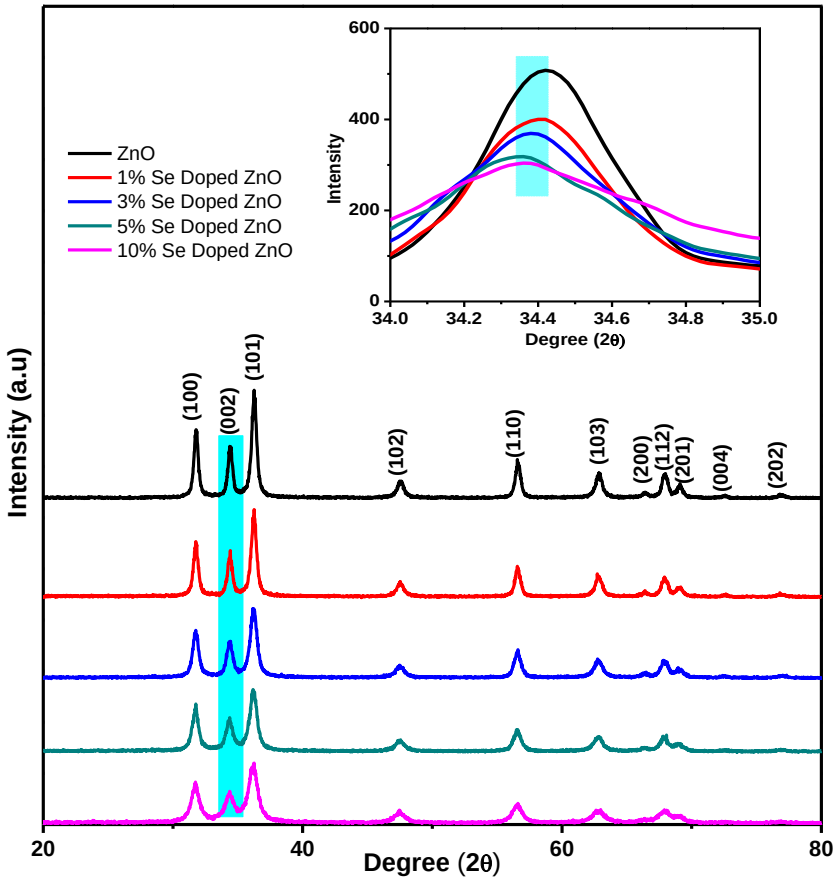

Figure 3.1 XRD spectra of undoped and Se (0, 1, 3, 5 or 10%) doped ZnO. The inset shows a peak shift of the (002) plane

To measure the Se doping effect on the crystalline structure of ZnO, XRD diffraction peak (002) of pure ZnO with Se doped ZnO nanomaterials were compared as shown in **Figure 3.1** (inset). Figure 3.1 shows a slight shift of Se doped ZnO XRD reflection peak (002) to lower 2θ values relative to that of undoped ZnO. This is due to the introduction of selenium into the crystal structure causing distortion in the crystal lattice. The distortion is proportional to the amount of dopant and increases with % wt. of Seas shown in the inset of **Figure 3.1**. The values of lattice parameters, a and c, for hexagonal crystal lattice were calculated using the following equation.

$$\frac{1}{d^2_{(hkl)}} = \frac{4}{3}\left(\frac{h^2 + hk + k^2}{a^2}\right) + \frac{l^2}{c^2}$$

Figure 3.2 shows that the lattice parameters, a and c, also increases with the increase in %wt. of Se due to the incorporation of Se into ZnO crystal lattice (**Table 3.1**).

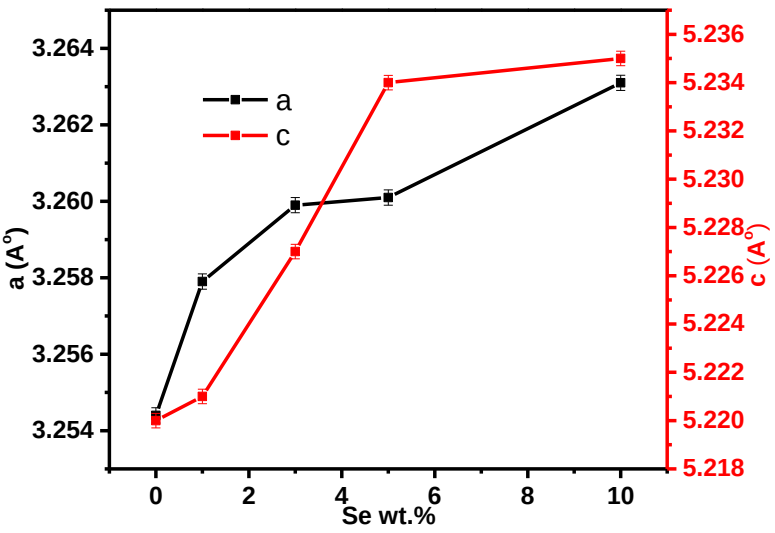

Figure 3.2 Variation of lattice parameters, a and c, with Se wt.%

These results suggest that during the annealing process, the oxygen vacancies (V_o) and oxygen interstitials (Oi) defects are formed by possible incorporation of selenium into the ZnO crystal structure. Thus, the crystal lattice expansion occurs due to the formation of more oxygen interstitials resulting in orange-red fluorescence of the doped nanomaterial. After adding 5 or 10% wt. of Se to ZnO, the doping has little effect on 2θ values, lattice parameters, and strain in the crystal lattice (**Figure 3.2**). The average lattice strain (ε) along the c-axis oriented in Se doped ZnO is calculated using the following expression.

$$\varepsilon = \left(\frac{C - C_0}{C_0}\right)$$

where C_0 is the lattice of bulk ZnO.

Table 3.1 Variation of lattice parameter c, lattice strain of pure ZnO and Se doped ZnO nanorods

Sample Name	**(hkl)**	**2θ (Degree)**	**d Spacing**	**c (Å)**	**Strain (%)**
Pure ZnO	002	34.423	2.6100	5.205	0.093
1 wt.% Se doped ZnO	002	34.415	2.6106	5.212	0.113
3 wt.% Se doped ZnO	002	34.377	2.6133	5.215	0.228
5 wt.% Se doped ZnO	002	34.325	2.6172	5.227	0.362
10 wt.% Se doped ZnO	002	34.324	2.6173	5.226	0.381

After Se incorporation, the Se-O bond formation occurs due to the transfer of an electron from Se to O, suggesting that selenium is an n-type dopant. The XPS spectra of Se doped ZnO shows peaks at 1044, 1021, 530.24, 59.3, and 54.3 eV's (shown in **Figure 3.3**) corresponds to the spin-orbital binding energies of $Zn2p_{1/2}$, $Zn2p_{3/2}$, O1s, $Se3d_{3/2}$, and $Se3d_{5/2}$ states

respectively due to the presence of Zn(II), O^{2-}, SeO_x and Se in Se doped ZnO NRs that confirmed the existence of selenium as a doping element in ZnO [34].

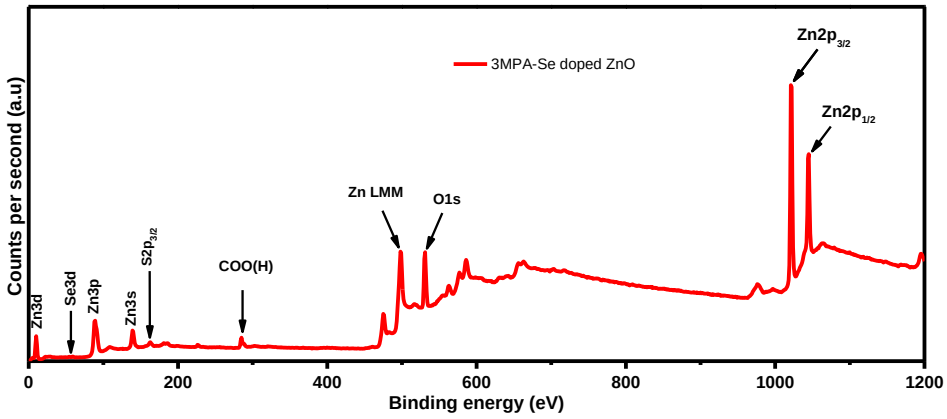

Figure 3.3 A survey XPS spectra of 3MPA-Se doped ZnO nanoprobe

The XPS spectra of Se doped ZnO shows a lower BE peak at 54.3 eV and a higher BE peak at 59.3eV, associated with 3d orbitals of Se and SeO_x [38] present in the crystal structure of doped nanomaterial (**Figure 3.4a**). These BE peaks suggest the incorporation of Se into ZnO crystal structure with the formation of Se-O bond supported by the shift of XRD peaks. The O1s spectrum shown in **Figure 3.4b** was Gaussian fitted and shows peaks at 530.16, 531.26, and 532.48 eV, which are attributed to the presence of lattice oxygen (O_L), oxygen vacancies (V_o), and oxygen interstitials (O_i), respectively, in Se doped ZnO NRs [39]. These oxygen defects are responsible for the observed fluorescence emission of Se doped ZnO NRs in agreement with photoluminescence studies.

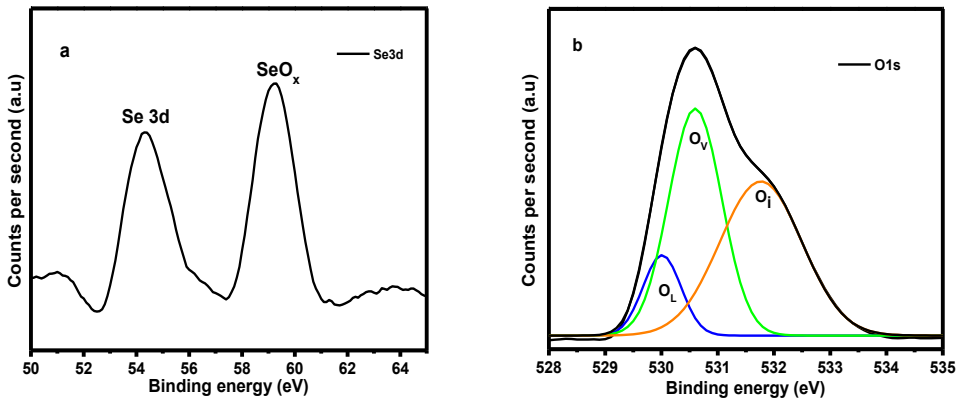

Figure 3.4 XPS spectra of **(a)** Se 3d and **(b)** O1s in Se doped ZnO

Interestingly, during the preparation of Se doped ZnO nanorods by mechanothermal method, O_2 adsorbed on the surface of nanomaterial promotes negative charging of nanostructure up to –2. The adsorbed oxygen molecule dissociates into interstitial sites of a nanomaterial as charged species called oxygen interstitial (O_i), leading to defects [40]. Therefore, the split oxygen can be regarded as two interstitial oxygen (O_i) atoms associated with an overall negative charge in Se doped ZnO crystal structure [41]. So, Se doped ZnO nanorods possess negative zeta potential (–17.06 mV), which is due to the presence of negatively charged oxygen interstitial defects. These defects also promote lattice expansion over the c axis of Se doped ZnO, which supports our XRD data (**Figure 3.1**).

The morphology of Se doped ZnO NRs was also analyzed using FE-SEM, which confirms that Se doped ZnO nanomaterial was formed in a rod shape with an average diameter of nanorods around 50 nm, as shown in **Figure 3.5a**. Various factors like lattice mismatch, temperature, annealing rate, surface energy, and defects also play an essential role in forming nanorods and their self-assembly [42,43]. Thus, a high heating rate at the higher temperature (450 °C) produces fewer nucleation sites that are favorable for crystal growth along one direction of ZnO's hexagonal structure, resulting in the formation of nanorods [44]. The spherically

shaped dots present at the end of Se doped ZnO NRs shown within the dashed circle in **Figure 3.5a** perhaps provide the required nucleation sites for nanorod formation [45].

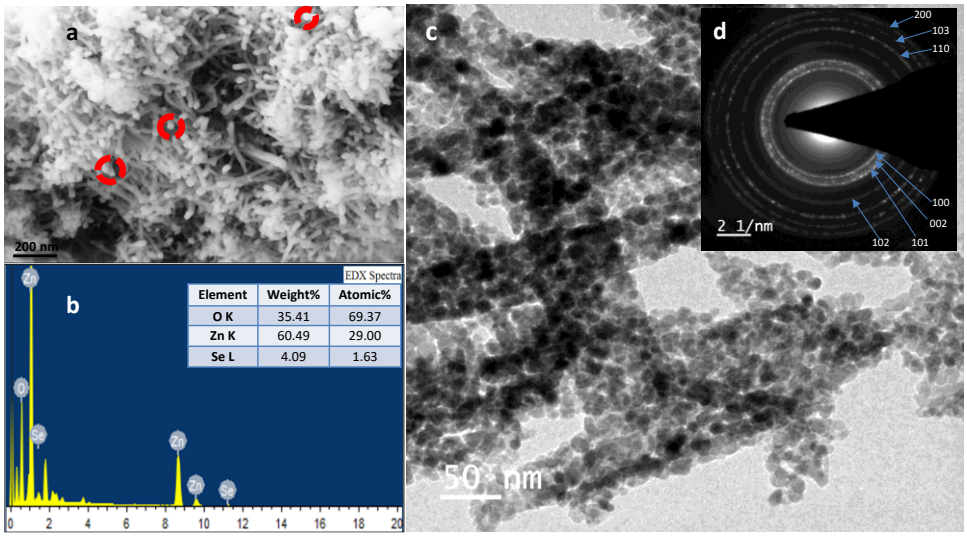

Figure 3.5 Analysis of Se doped ZnO NRs by **(a)** FE-SEM, **(b)** EDX, **(c)** HRTEM and **(d)** SAED pattern

Nanorods prepared by our methodology possess well-defined crystalline nature suggesting that the crystal growth mechanism involves a terminating zinc atom [46]. The elemental composition of Se doped ZnO NRs was determined by energy-dispersive X-ray (EDX) spectrum, which clearly shows that selenium is part of doped ZnO NRs material (**Figure 3.5b**). Finally, from HR-TEM analysis, it was clearly found that the nanoparticles are assembled into rod-shaped structures, as shown in **Figure 3.5c**. These results suggest that the spherical end of Se doped ZnO nanorods is due to nanoparticle assembly. Moreover, the selected area electron diffraction (SAED) pattern obtained from HRTEM analysis of Se doped ZnO nanomaterial match with the crystal planes expected for hexagonal wurtzite-structure from XRD analysis (**Figure 3.5d**).

Previously it was reported that Se doped ZnO nanoparticles show a strong green fluorescence emission at 565 nm due to the presence of oxygen

vacancies and zinc interstitial defect centers [34]. Whereas photoluminescence spectrum of our newly synthesized Se doped ZnO NRs, annealed in the presence of excess oxygen, show strong orange-red fluorescence emission at 625 nm, perhaps, due to oxygen interstitials and oxygen vacancy defects in the crystal lattice [28,47,48]. It was also observed that during the formation of nanorods, the aspect ratio of the prepared nanorod surface increases. Consequently, the absolute number of oxygen interstitials and vacancies present in the Se doped ZnO NRs also increases, resulting in enhancement of photoluminescence, which is further supported by the morphological studies of nanorods using FE-SEM [49].

Quantum yield (QY) of Se doped ZnO nanorods was also calculated from the PL integrated intensity using DAPI as a standard dye, as shown in **Figure 3.6**. The QY of Se doped ZnO (Φ) was found to be 0.148 from the following formula.

$$\Phi = \Phi_R \frac{I}{I_R} \frac{A_R}{A} \frac{n^2}{n_R^2}$$

where Φ is the quantum yield, I is the integrated intensity, A is the optical density, and n is the refractive index of the solvent. The subscript R refers to the standard reference dye DAPI of known quantum yield (Φ_R= 0.043).

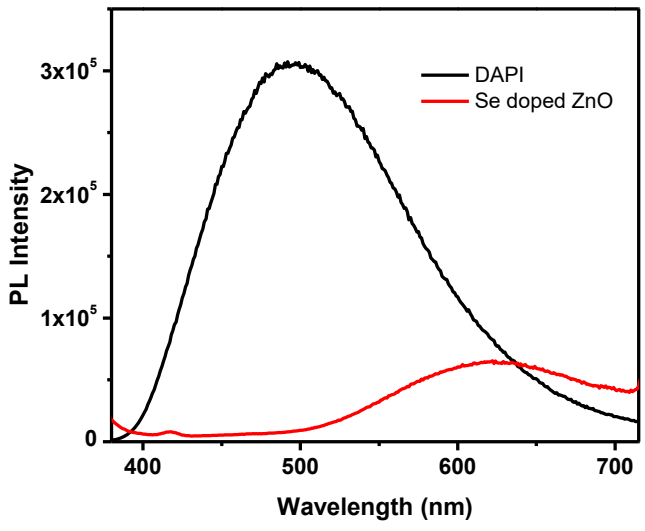

Figure 3.6 PL spectra of DAPI and Se doped ZnO NRs at 365 nm excitation

3.2.2 Characterization of 3MPA-Se doped ZnO Nanoprobe

XRD diffraction analysis of MPA-Se doped ZnO NRs was carried out to study the effect of MPA capping on the crystal structure and compared with Se doped ZnO NRs as shown in **Figure 3.7a**. The peak positions of MPA capped Se doped ZnO NRs are identical to that of Se doped ZnO NRs. However, the MPA capped Se doped ZnO NRs shows a slight decrease in the intensity of the diffraction peaks. This is probably due to the reduction of crystalline nature and surface structure distortion effect, thereby suggesting that Se doped ZnO NRs are functionalized with MPA ligand [50]. The absence of significant changes in the XRD pattern of MPA capped Se doped ZnO NRs reveals that MPA ligand was capped without affecting the nanoprobe's crystal structure. Moreover, the peak width of MPA capped and uncapped Se doped ZnO diffraction patterns remains the same, indicating that both the materials should have a similar crystallite size [51].

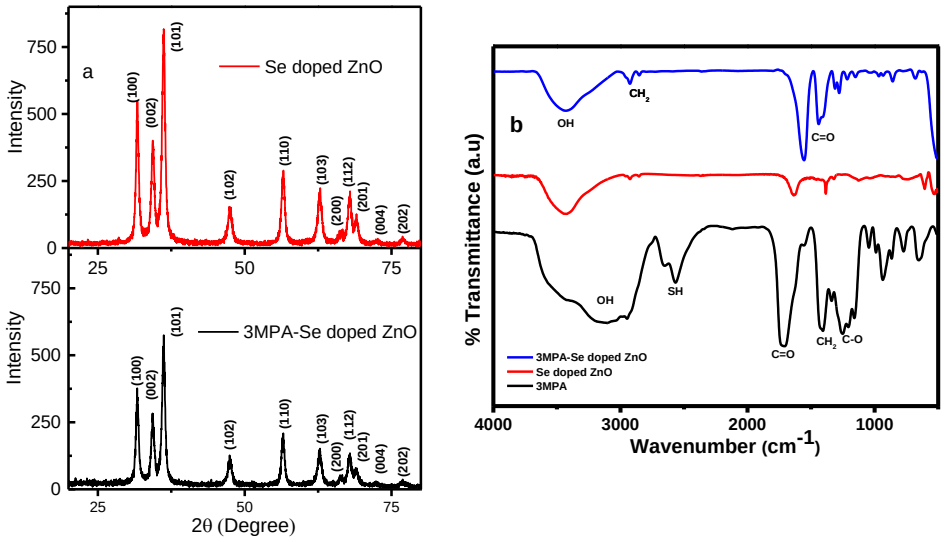

Figure 3.7 (a) XRD patterns of newly synthesized Se doped ZnO NRs and 3MPA functionalized Se doped ZnO NRs, **(b)** FTIR spectra of 3-MPA, Se doped ZnO NRs, and MPA-Se doped ZnO NRs

The surface nature of Se doped ZnO NRs and their interaction with 3-mercaptopropionic acid (MPA) was further examined by using FTIR and ATR techniques. **Figure 3.7b** shows the presence of thiol stretching vibration of MPA at 2566 cm^{-1}. In contrast, its absence in MPA capped Se doped ZnO NRs reveal covalent attachment of –SH functional group to Zn atoms on the surface of nanoprobe [52,53]. However, only a few carboxylic acid groups in MPA are converted to COO^- ion, whose presence is confirmed by the appearance of peaks at 1558 and 1395 cm^{-1}. This is due to partial dissociation of the acid group of MPA at pH 5.5 [54].

From XPS studies of MPA capped Se doped ZnO NRs, the $S2p_{3/2}$ peak shown in **Figure 3.8a** indexed at 162.6 eV was attributed to the presence of covalently bound sulfur atoms of MPA to Zn metal ions in Se doped ZnO NRs. Further, the lack of additional peaks in the binding region above 164 eV confirms the absence of the unbound –SH group (B.E 165 eV) [55]. The binding energy at 285.3 eV can be ascribed to the carbon atoms in the COO(H) moiety of mercaptopropionic acid [56]. These results confirm beyond speculation that MPA ligand is bound to Se doped ZnO NRs through thiol (SH) group. Interestingly the strong orange-red fluorescence emission at 625 nm in Se doped ZnO NRs was observed to be quenched during surface capping with MPA due to passivation of surface defects present in the nanorods (see **Figure 3.8b**). This phenomenon is utilized in our methodology as a basis for mercury detection by fluorescence “turn on” mechanism.

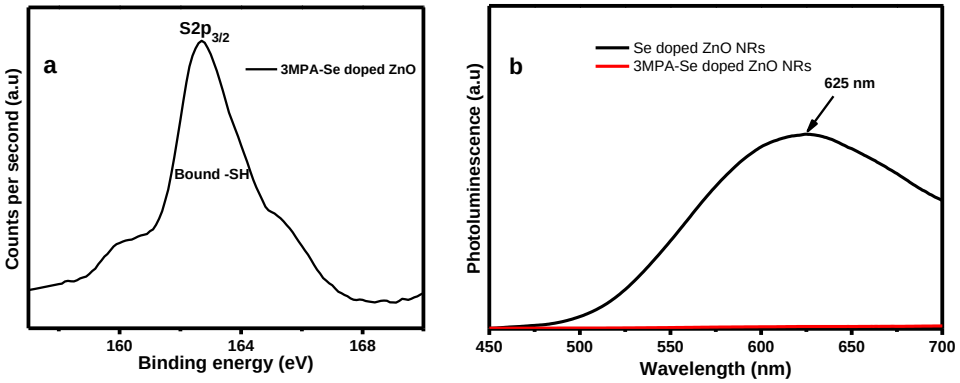

Figure 3.8 **(a)** XPS spectra of S $2p_{3/2}$ transitions in 3MPA-Se doped ZnO nanoprobe, **(b)** PL spectra of Se doped ZnO nanorods, and 3MPA capped Se doped ZnO NRs

The effect of nanoprobe PL at various pH (2.0–12.0), temperatures (10 °C to 80 °C), and shelf life (1-day to 6 months) were studied using a fluorescence spectrometer. Below pH 7.0 (i.e., at pH 5 and 2), the deprotonated thiol and carboxylate moieties of MPA were protonated, and the MPA ligands detach from nanoprobe due to dissolution of Se doped ZnO nanorods in an acidic medium [20]. Also, the residual photoluminescence intensity of the nanoprobe at pH 7.0 becomes obsolete as the pH decreases from 7 to 2 (**Figure 3.9a**), rendering the probe unsuitable for detection of mercury.

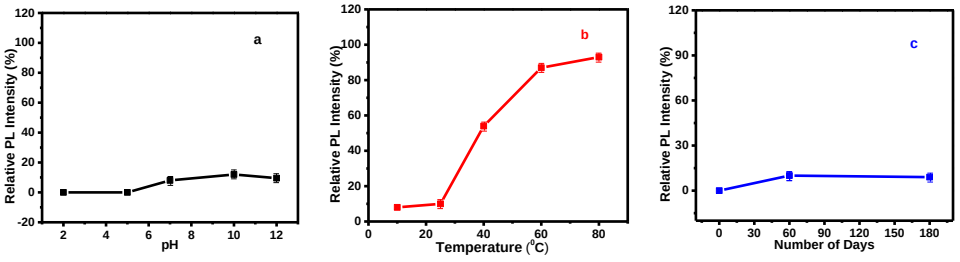

Figure 3.9 Effect of **(a)** pH, **(b)** temperature, and **(c)** stability of nanoprobe

Although the relative emission intensity of the nanoprobe solution at pH 10 and 12 increases slightly than at pH 7, the formation of metal hydroxides under strongly alkaline conditions becomes an undesirable

chemical transformation for the nanoprobe's sensing performance (**Figure 3.9a**). MPA-functionalized Se doped ZnO nanoprobe does not show any major change in PL intensity between 0 ℃ and 25 ℃. As the temperature is raised to 40 ℃, the nanoprobes PL intensity increases drastically due to the detachment of MPA ligands from the nanoprobe surface. This effect is more pronounced at 60 ℃ and 80 ℃, indicating that the nanoprobe is unfavorable for sensing at higher temperatures (**Figure 3.9b**). However, the PL intensity of the nanoprobe solution at the different aging times, over a period of 6-months, remains the same (**Figure 3.9c**). These results suggest that the nanoprobe has good stability and usability for a period of 6-months at room temperature and physiological pH.

3.2.3 Mercury sensitivity of nanoprobe in aqueous solutions

The newly synthesized nanoprobe was next examined for the detection of Hg^{2+} ions in an aqueous solution. MPA coated on the nanomaterial acts as a hydrophilic ligand and enhances the solubility of Se doped ZnO nanoprobe. The thiol group present in the nanoprobe interacts with Hg^{2+} ions due to the high affinity of sulfur to Hg^{2+} ions, resulting in a stable Hg–S bond [57]. As the concentration of Hg^{2+} ions increases from 100-500 nM (100, 200, 300, 400, and 500 nM), the PL of the quenched nanoprobe is restored gradually during the first 30 secs followed by a decrease in PL emission after 30 secs as shown in **Figure 3.10a** and **3.10b**, respectively. In the initial 30 secs, there is an enhancement in PL emission intensity due to MPA ligands detachment from Se doped ZnO NRs. These uncapped Se doped ZnO NRs are only stable for a short period of 30 secs in the solution, and they further aggregate due to interparticle H-bonding interactions, leading to PL quenching.

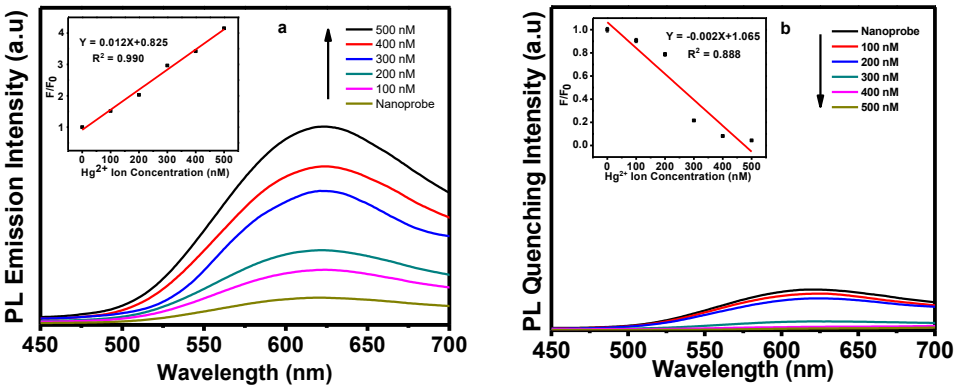

Figure 3.10 (a) PL emission spectra of MPA-coated Se doped ZnO NRs in aqueous solution in the presence of different amounts of Hg^{2+} ions (100–500nM) by excitation at 365 nm in the first 30 sec of measurement. **(b)** PL quenching spectra of nanoprobe after 30 (30-60) sec of measurement. Linear fit analysis for emission and quenching mechanisms were shown in the inset of 3a and 3b, respectively

The efficiency of the proposed turn-on and turn-off mechanism, PL spectra of nanoprobe for detecting various concentrations of Hg^{2+} ions (100, 200, 300, 400, and 500 nM) at 625 nm were analyzed using a linear regression plot. The linear regression analysis suggests that mercury detection was highly effective, rapid, and consistent with PL emission (R^2=0.99) rather than quenching (R^2=0.888) mechanism in concurrence with our proposed mechanism as shown in **Figure 3.10a** (inset) and **3.10b** (inset). FE-SEM images further confirmed the proposed PL emission (turn-on) and quenching (turn-off) mechanism induced by the anti-aggregation and aggregation effect. FE-SEM images of nanoprobe recorded in initial 30 sec of the addition of Hg^{2+} ions show highly dispersed nanorods **(Figure 3.11a),** whereas, after a min, the nanorods aggregate together **(Figure 3.11b)**.

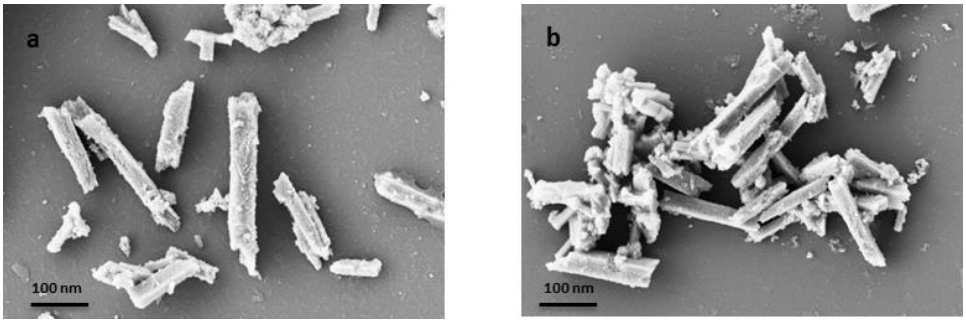

Figure 3.11 FE-SEM images of 100 μM nanoprobe solution in initial 30 sec **(a)**, and **(b)** after 1 min of reaction time with 300 nM Hg^{2+} ions

The samples required for acquiring FE-SEM images were prepared by spotting a drop of reaction mixture withdrawn during the initial 30 seconds and after a minute of the addition of Hg^{2+} sample to nanoprobe on two different glass slides. The droplet on the glass slides was further dried at 90 °C on a preheated hot plate for a few minutes until the vaporization of water. The proposed mechanism of PL quenching by aggregation effect is also confirmed by measuring the absorption spectrum of samples after 30 secs of the addition of Hg^{2+} sample (**Figure 3.12**).

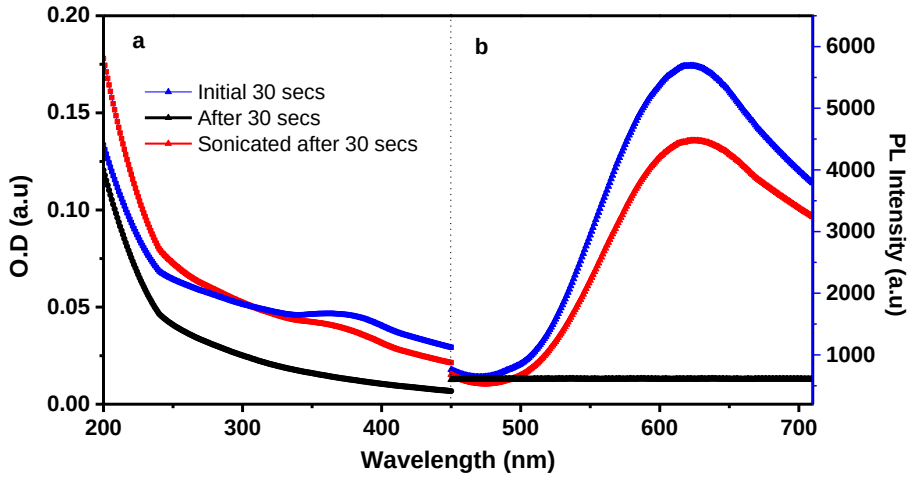

Figure 3.12 (a) Absorption and **(b)** Photoluminescence spectra of dispersed, aggregated and sonicated nanoprobe samples

It is evident from **Figure 3.12a** that the absorption peak of nanoprobe is minimum after 30 secs, which is restored to original absorption intensity

after a brief sonication of the aggregated nanoprobe. In the case of PL emission studies, PL is maximum during the initial 30 secs of the addition of Hg^{2+} sample. It reaches a minimum after 30 secs due to aggregation of MPA uncapped nanoprobe. In contrast, PL restoration is more prominent on a sonicated sample obtained after 30 secs of the addition of Hg^{2+} (**Figure 3.12b**). These results clearly suggest that the PL quenching is due to the aggregation of the NRs and the phenomenon is described later in Fig. 3.14.

The proposed mechanism was further probed by measuring photoluminescence of Se doped ZnO NR's during the first 30 secs and after 30 secs of the addition of Hg^{2+} ions. This experiment also shows that the PL emission of nanoprobe increases during the first 30 secs followed by a steep decrease during 0.5-5 min (**Figure 3.13a**). In the initial 30 secs, the increase in PL emission is due to the detachment of MPA ligand from nanoprobe surface which is caused by a very strong interaction of Hg^{2+} ions present in test solutions and the thiol group of MPA ligand coated on nanoprobe [58]. From 0.5 to 5 min time, the NRs start aggregating due to a significant increase in the H-bonding interactions between nanorods resulting in decreased PL intensity.

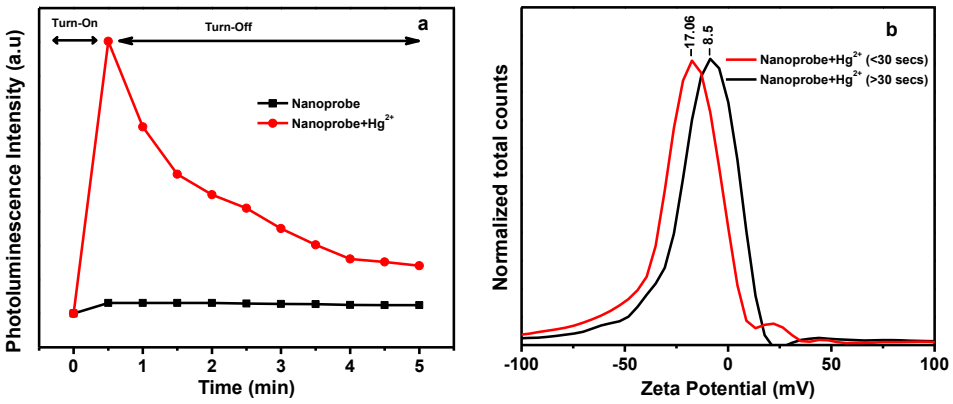

Figure 3.13 (a) Photoluminescence studies at various time points from 0 sec to 5 min after the addition of Hg^{2+} ions and **(b)** Zeta potential of 100

μM MPA-Se doped ZnO nanoprobe before and after 30 secs in the presence of 300 nM Hg^{2+} ions

Moreover, zeta potential measurements (**Figure 3.13b**) show that the NRs are dispersed before 30 secs with higher (–17.06 mV) charges. In contrast, after 30 secs (0.5–5 min), the zeta potential decreases to –8.5 mV due to the aggregation of NRs. This provides unequivocal evidence for the proposed mechanism of "turn-on" and "turn- off" during the detection of Hg^{2+} ions. Further, the lowest mercury detection limit in test solutions of different concentrations (0.001 to 100 nM) of Hg^{2+} ions using our nanoprobe was found to be 1 pM, as shown in **Figure 3.14**.

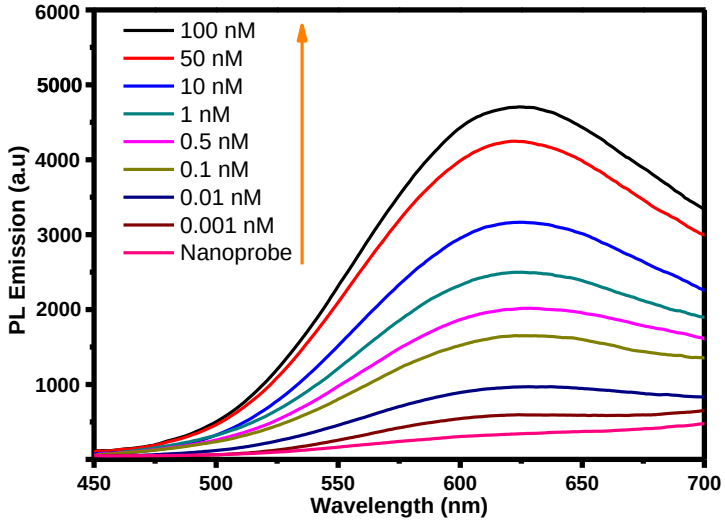

Figure 3.14 Sensitivity or limit of detection (LOD) of nanoprobe for detection of Hg^{2+} ions: PL spectra of MPA-coated Se doped ZnO NRs in aqueous solution in the presence of Hg^{2+} ions (0.001–100 nM) by excitation at 365 nm

The validity of mercury detection methodology was also verified using UV–Vis spectroscopy over a range of Hg^{2+} ion concentration (0.001 nM–100 nM) as shown in **Figure 3.15a**. Measurement of absorption spectra shows that the optical density (O.D) of the nanoprobe increases with an increase in Hg^{2+} concentration due to the detachment of 3MPA ligands,

and the LOD was found to be 1 pM. Moreover, the detection was linear in the range of 0.001 nM–1 nM of Hg^{2+} ions with the best correlation of 0.992 as shown in **Figure 3.15b**.

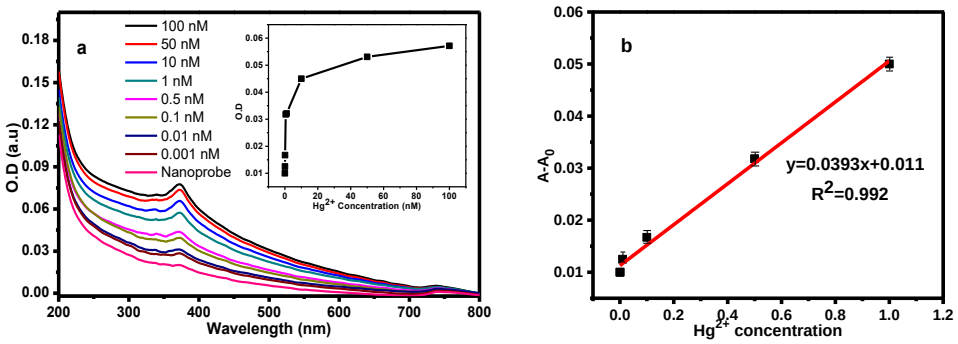

Figure 3.15 (a) UV–Vis absorption spectra for detecting Hg^{2+} with nanoprobe and a plot of O.D versus concentrations of Hg^{2+}(inset). **(b)** Linear fit analysis in the detection range from 0.001 nM–1 nM

An AND logic gate (**Figure 3.16a**) based on Se-doped ZnO NRs using $Hg^{2+,}$ and 3MPA coated Se-doped ZnO NRs as inputs and the photoluminescence signal as an output was also designed. This logic gate could be used to detect trace amounts of $Hg^{2+,}$ as shown in the truth table. In the AND logic gate operation, the presence of both inputs (1/1) would cause a fluorescence enhancement in 625 nm (output = 1). In contrast, the presence of either input (0/1, 1/0) or the absence of both inputs (0/0), the detection system would give a low or weak photoluminescence signal (output = 0) (**Figure 3.16b**). Accordingly, it was found that the output is "1" (enhanced PL at 625 nm) only when both nanoprobe and Hg^{2+} ions were added into the system (input = 1/1), and it is "0" (weak PL) when only one of them or neither was added (input = 1/0, 0/1, 0/0) (**Figure 3.16c**).

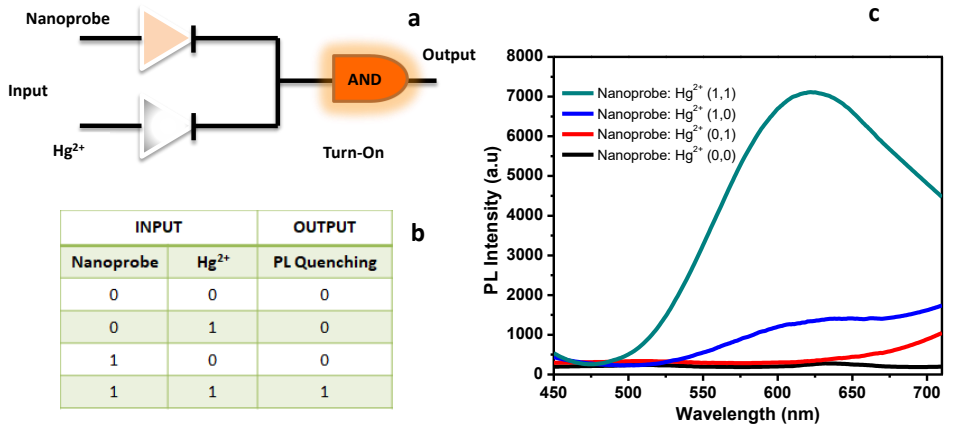

INPUT		OUTPUT
Nanoprobe	Hg^{2+}	PL Quenching
0	0	0
0	1	0
1	0	0
1	1	1

Figure 3.16 Proposed turn-on mechanism for Hg^{2+} detection based on **(a)** AND logic gate, **(b)** truth table and **(c)** PL emission

3.2.4 Selectivity for Mercury Ions

Finally, to investigate the selectivity of our effective turn-on mercury sensing method, PL emission of Se doped ZnO nanoprobe (50 µM solution) was examined in the presence of several other heavy metal (M^{n+}) ions, including Hg^{2+}, Ca^{2+}, Zn^{2+}, Na^{+}, K^{+}, Fe^{3+}, Mn^{2+}, Co^{2+}, Cd^{2+}, Cu^{2+} and Ag^{+} (25µM). These metal ions, except Hg^{2+}, separately do not show any significant enhancement in fluorescence due to the presence of any nonspecific interaction with the nanoprobe thiol group, as shown in **Figure 3.17** (black bar). The binding and interference interactions of other metal ions (45 µM) were further evaluated by PL spectra of nanoprobe (50 µM) in the presence of Hg^{2+} (5 µM) ions. The relative PL of nanoprobe shown in **Figure 3.17** (red bar) demonstrates a significant increase in emission intensity when a low concentration (5 µM) of Hg^{2+} ions is added to the reaction mixture containing a higher concentration of other metal ions (45µM). These results indicate that MPA-Se doped ZnO nanoprobe is insensitive to other metal ions and highly selective for detecting Hg^{2+} ions.

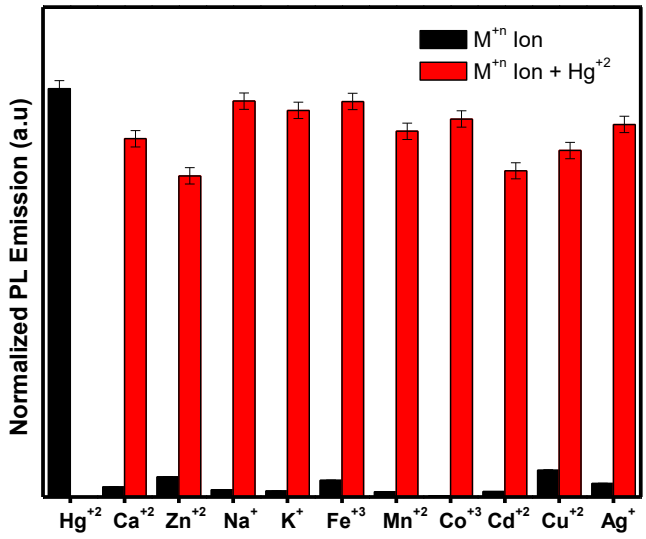

Figure 3.17 Relative PL intensity histogram of 3MPA–Se doped ZnO nanosensor in selective binding of metal ions (Hg^{2+}, Ca^{2+}, Zn^{2+}, Na^{+}, K^{+}, Fe^{3+}, Mn^{2+}, Co^{2+}, Cd^{2+}, Cu^{2+} and Ag^{+}) in the absence and presence of mercury ions (denoted by red bar).

Additionally, to demonstrate the applicability of our method in environmental samples, different concentrations of Hg^{2+} (0, 100, 200, 300, 400, and 500 nM) were spiked into tap water, and the samples were analyzed using our nanoprobe. A linear correlation was found to exist between Hg^{2+} concentrations and PL intensity of standard samples in Milli–Q water and samples spiked in tap water (**Figure 3.18**).

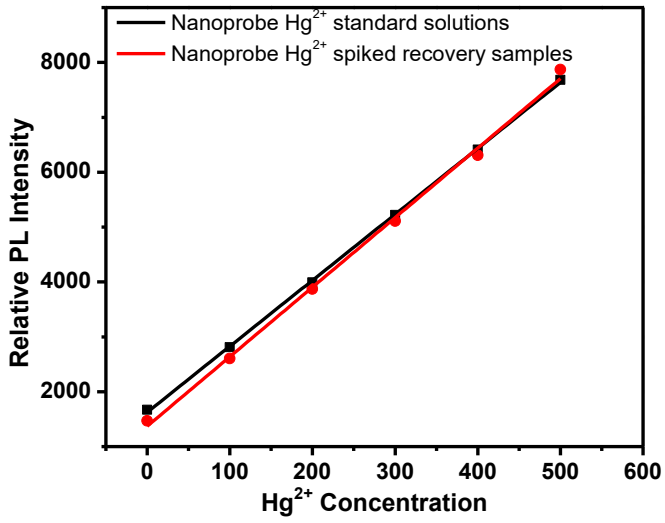

Figure 3.18 A plot of Hg^{2+} concentration vs. PL intensity for standard Hg^{2+} solutions (black) and spiked tap water samples (red)

After analysis, spiked percentage recovery for samples of various concentrations is calculated and found to be within the acceptable range of 93-99%, as shown in **Table 3.2**. These results demonstrate that the nanoprobe is applicable for the practical analysis of Hg^{2+} in real samples.

Table 3.2 Determination of Hg^{2+} ions in spiked tap water samples using MPA–Se doped ZnO nanoprobe

Sample	**Spiked Hg^{2+} (nM)**	**Detected Hg^{2+} (nM)**	**Recovery (%)**
Tap Water	0	ND	---
Tap Water	100	98.7	98.7
Tap Water	200	192.2	96.1
Tap Water	300	293.1	97.7
Tap Water	400	397.5	99.3
Tap Water	500	483.9	96.7

3.3 Conclusion

In this study, defects (oxygen interstitials and zinc vacancy) induced orange-red photoluminescence emission of Se doped ZnO nanomaterial was functionalized by MPA and used as a nanoprobe for detection of Hg^{2+} ions in aqueous solutions. In the presence of Hg^{2+} ions, this nanoprobe exhibit consistent PL “turn-on” emission a direct phenomenon achieved

by the detachment of MPA from Se doped ZnO surface over indirect "turn off" mechanism, which may be attributed due to the aggregation of nanorods. The turn-on emission is more effective and takes place within 30 seconds because of the strong binding affinity of Hg^{2+} ions towards the bound MPA thiol group. The sensitivity of chemosensor for selective detection of Hg^{2+} ions is demonstrated to be very effective up to a detection limit of 1 pM concentration of Hg^{2+} ions. Moreover, nanoprobe selectivity is also very high to detect Hg^{2+} ions in the presence of other heavy metal ions. Thus, our chemosensor based on Se doped ZnO nanomaterial eliminates the need to use complex conventional instruments (ICP-MS, GC, NMR, etc.), expensive noble metals, and toxic quantum dots for the detection of mercury. The proposed approach will offer a great potential to fabricate a direct and efficient mercury sensor that can be employed for environmental and health applications.

3.4 Experimental section

3.4.1 Chemicals

Zinc acetate dihydrate and oxalic acid were purchased from Merck Millipore, India. Selenium metal powder and 3-mercaptopropionic acid (3MPA) were procured from Acros Organics, India. Mercury chloride was obtained from Sigma Aldrich, India. Other metal (Hg^{2+}, Ca^{2+}, Zn^{2+}, Na^{+}, K^{+}, Fe^{3+}, Mn^{2+}, Co^{2+}, Cd^{2+}, $Cu^{2+,}$ and Ag^{+}) ion stock solutions were prepared from their respective salts in Millipore water. All other chemicals were used without further purification unless and otherwise specified.

3.4.2 Preparation of Se doped ZnO nanorods

Se doped ZnO nanorods were synthesized by modification of the previously reported method.[34] In a typical synthesis, $Zn(CH_3COO)_2 \cdot 2H_2O$ (0.685 g, 3.12 mmol) oxalic acid (0.472 g, 3.74 mmol) and selenium (% wt. = 0, 1, 3, 5 or 10) mixture were ground for 20 min and subjected to

heat treatment in a muffle furnace at 450 °C for 30 min. The product was washed with Milli-Q water and ethanol 4–5 times and dried in a hot air oven overnight at 70 °C. Finally, the Se doped ZnO NRs sample was characterized by powder XRD, FE-SEM, HRTEM, photoluminescence spectrophotometry, and further surface functionalization of nanorods were carried out using 3-mercaptopropionic acid (MPA) as described below.

3.4.3 Preparation of 3MPA functionalized Se doped ZnO nanosensor

Se doped ZnO nanorods (50 mg, 0.615 mmol based on ZnO) were dispersed in the aqueous medium (5 mL, pH 7) by sonication in an ultrasonic bath for 20 min. 3MPA (9.5 µl, 0.11 mmol) was added to the above mixture, and the final pH of the solution is measured to be 5.5. The mixture was continuously stirred using a magnetic stirrer for 10–15 h at room temperature. The resultant product was collected and repeatedly washed with water (5 mL × 3) and acetone (5 mL × 3). Finally, the sample was dried at 40 °C in a hot air oven for 4–5 h and used further for surface characterization and mercury detection.

3.4.4 Characterization of Se doped ZnO and 3MPA-Se doped ZnO nanosensor

The morphology of Se doped ZnO was characterized by Field Emission Scanning Electron Microscopy (Carl Zeiss Supra 55) and Field Emission Gun-Transmission Electron Microscopy 300 kV (Tecnai G2, F30). Powder XRD patterns of 3MPA capped and uncapped Se doped ZnO were determined on a Rigaku SmartLab, Automated Multipurpose X-ray Diffractometer with a Cu K_α source (the wavelength of X-ray is 1.541 Å). FT-IR spectra of samples were recorded in KBr using Fourier Transform Infrared-Attenuated Total Reflection (FTIR-ATR) Spectrometer, Bruker (Tensor-27) over a range of 500–4000 cm^{-1}. X-ray photoelectron spectroscopy (XPS) data was collected on Multilab 2000 Photoelectron

Spectrometer (Thermo VG Scientific MultiLab) chemical analysis probe using Al K_α X-ray (1486.6 eV, 75 W) as an exciting source for the identification of bound 3MPA to Se doped ZnO samples. Photoluminescence spectrum of Se doped ZnO and 3MPA-Se doped ZnO were recorded using Fluoromax-4 Spectrofluorimeter (HORIBA Jobin Yvon, model FM-100) at an excitation wavelength of 365 nm. The zeta potential measurements of nanoprobe in the presence of Hg^{2+} ions were performed using a NanoPlus (Micromeritics Instrument Corporation, USA).

3.4.5 Examination of mercury sensitivity of nanoprobe in aqueous solutions

For detection of mercury, stock solutions of 3MPA-Se doped ZnO nanoprobe (10 mM, 100 µM) and Hg^{2+} ions solution (10 mM and 100 µM from $HgCl_2$ salt) were prepared in Milli–Q water and dilutions (1 mM, 10 µM, 1 µM, 0.01 µM, and 0.001 µM) of various concentrations of Hg^{2+} ions were prepared from stock solutions as per requirement. The dual emission-quenching efficiency of nanoprobe (100 µM solution) in the presence of various concentrations of Hg^{2+} ions (100, 200, 300, 400, and 500 nM) were recorded at 625 nm in PL spectrophotometer by using an excitation wavelength of 365 nm. The sensitivity and limit of detection (LOD) of nanoprobe (50 µM) were measured by recording the fluorescence emission spectra at 625 nm as well as UV-Vis absorption spectra for various concentrations of Hg^{2+} ions in the range 0.001–100 nM (0.001, 0.01, 0.1, 1, 10, 50 and 100 nM).

3.4.6 Investigation of the feasibility of the logic gates

To investigate the detection mechanism by Boolean logic gates principle, stock solutions of 3MPA-Se doped ZnO nanoprobe (10 mM, 100 µM and 10 µM) and Hg^{2+} ions solution (10 mM) were prepared in Milli–Q water. The final concentration of nanoprobe (100 µM) and Hg^{2+} (300 nM) were

prepared from stock solutions as per requirement. PL spectra of the nanoprobe at 625 nm was measured by using an excitation wavelength of 365 nm with AND logic table combinations.

3.4.7 Selectivity of Hg^{2+} sensing studies

The selectivity of Hg^{2+} detection using 3MPA-Se doped ZnO nanorods was studied by performing the PL studies of 3MPA-Se doped ZnO nanosensor in the presence of other metal ions including Hg^{2+}, Ca^{2+}, Zn^{2+}, Na^{+}, K^{+}, Fe^{3+}, Mn^{2+}, Co^{2+}, Cd^{2+}, $Cu^{2+,}$ and Ag^{+}. The potential interference of other metal ions (25 µM) during the detection of Hg^{2+} ions with nanoprobe (50 µM) was examined by performing the experiment in the absence of Hg^{2+} ions. In a similar way, the selectivity of Hg^{2+} ions to nanoprobe (50 µM) solution was also determined by the addition of other metal ions (45 µM) in the presence of Hg^{2+} ions (5 µM). Interference and selective affinity studies for nanoprobe were analyzed by recording fluorescence emission spectra at 625 nm on blank, other metal ions, and in the presence of mercury ions with different metal ions.

3.4.8 Spiked recovery

Stock solutions of MPA-Se doped ZnO nanoprobe (10 mM) and Hg^{2+} ions solution (1 µM) were prepared in tap water. The final concentration of nanoprobe (100 µM) and Hg^{2+} (100–500 nM) were prepared from stock solutions as per the requirements. Then Hg^{2+} recovery was evaluated by measuring PL at 625 nm for different concentrations (100–500 nM) of spiked Hg^{2+} ions.

3.5 References

1. Gonzalez-Raymat H., Liu G., Liriano C., Li Y., Yin Y., et al. (2017), Elemental mercury: Its unique properties affect its behavior and fate in the environment, Environ Pollut, 229, 69–86 (DOI: 10.1016/j.envpol.2017.04.101)

2. Nolan E. M., Lippard S. J. (2008), Tools and tactics for the optical detection of mercuric ion, Chem Rev, 108, 3443–3480 (DOI: 10.1021/cr068000q)

3. Liang S., Wang Y., Cinnirella S., Pirrone N. (2015), Atmospheric mercury footprints of nations, Environ Sci Technol, 49, 3566–3574 (DOI: 10.1021/es503977y)

4. Driscoll C. T., Mason R. P., Chan H. M., Jacob D. J., Pirrone N. (2013), Mercury as a global pollutant: Sources, pathways, and effects, Environ Sci Technol, 47, 4967−4983 (DOI: 10.1021/es305071v)

5. Fitzgerald W. F., Lamborg C. H., Hammerschmidt C. R. (2007), Marine biogeochemical cycling of mercury marine biogeochemical cycling of mercury, Public Health, 107, 641–662 (DOI: 10.1021/cr050353m)

6. Clayden M. G., Kidd K. a, Wyn B., Kirk J. L., Muir D. C. G., et al. (2013), Mercury biomagnification through food webs is affected by physical and chemical characteristics of lakes, Environ Sci Technol, 47, 12047–12053 (DOI: 10.1890/02-3114.(5))

7. Hong Y.-S., Kim Y.-M., Lee K.-E. (2012), Methylmercury exposure and health effects, J Prev Med public Heal, 45, 353–363 (DOI: 10.3961/jpmph.2012.45.6.353)

8. Rice K. M., Walker E. M., Wu M., Gillette C., Blough E. R. (2014),

Environmental mercury and its toxic effects, J Prev Med Public Heal, 47, 74–83 (DOI: 10.3961/jpmph.2014.47.2.74)

9. Fernandes Azevedo B., Barros Furieri L., Peçanha F. M., Wiggers G. A., Frizera Vassallo P., et al. (2012), Toxic effects of mercury on the cardiovascular and central nervous systems, J Biomed Biotechnol, 2012, 1–11 (DOI: 10.1155/2012/949048)

10. Ebdon L., Foulkes M. E., Le Roux S., Muñoz-Olivas R. (2002), Cold vapour atomic fluorescence spectrometry and gas chromatography-pyrolysis-atomic fluorescence spectrometry for routine determination of total and organometallic mercury in food samples, Analyst, 127, 1108–1114 (DOI: 10.1039/B202927H)

11. Sánchez-Rodas D., Corns W. T., Chen B., Stockwell P. B. (2010), Atomic fluorescence spectrometry: A suitable detection technique in speciation studies for arsenic, selenium, antimony and mercury, J Anal At Spectrom, 25, 933 (DOI: 10.1039/b917755h)

12. Passariello B., Barbaro M., Quaresima S., Casciello A., Marabini A. (1996), Determination of mercury by inductively coupled plasma - mass spectrometry, Microchem J, 54, 348–354 (DOI: 10.1006/mchj.1996.0110)

13. Allibone J., Fatemian E., Walker P. J. (1999), Determination of mercury in potable water by ICP-MS using gold as a stabilising agent, J Anal At Spectrom, 14, 235–240 (DOI: 10.1039/a806193i)

14. Berzas Nevado J. J., Martín-Doimeadios R. C. R., Guzmán Bernardo F. J., Jiménez Moreno M. (2005), Determination of mercury species in fish reference materials by gas chromatography-atomic fluorescence detection after closed-vessel microwave-assisted extraction, J Chromatogr A, 1093, 21–28 (DOI: 10.1016/j.chroma.2005.07.054)

15. Clo H., Helm M. L., Helton G. P., Vanderveer D. G., Grant G. J. (2005), Mercury-199 NMR studies of thiacrown and related macrocyclic complexes : The crystal structures of [Hg ($18S_6$)](PF_6)$_2$ and [Hg($9N_3$)$_2$] (ClO_4)$_2$, Inorg Chem, 44, 5696–5705 (DOI: 10.1021/ic050500z)

16. Dairaku T., Furuita K., Sato H., Šebera J., Yamanaka D., et al. (2015), Direct detection of the mercury–nitrogen bond in the thymine–Hg^{II}–thymine base-pair with ^{199}Hg NMR spectroscopy, Chem Commun, 51, 8488–8491 (DOI: 10.1039/C5CC02423D)

17. James J. Z., Lucas D., Koshland C. P. (2012), Gold nanoparticle films as sensitive and reusable elemental mercury sensors, Environ Sci Technol, 46, 9557–9562 (DOI: 10.1021/es3005656)

18. Song C., Yang B., Zhu Y., Yang Y., Wang L. (2017), Ultrasensitive sliver nanorods array SERS sensor for mercury ions, Biosens Bioelectron, 87, 59–65 (DOI: 10.1016/j.bios.2016.07.097)

19. Ding X., Qu L., Yang R., Zhou Y., Li J. (2015), A highly selective and simple fluorescent sensor for mercury (II) ion detection based on cysteamine-capped CdTe quantum dots synthesized by the reflux method, Luminescence, 30, 465–471 (DOI: 10.1002/bio.2761)

20. Ke J., Li X., Shi Y., Zhao Q., Jiang X. (2012), A facile and highly sensitive probe for Hg(II) based on metal-induced aggregation of ZnSe/ZnS quantum dots, Nanoscale, 4, 4996–5001 (DOI: 10.1039/c2nr31238g)

21. Gao X., Xing G., Yang Y., Shi X., Liu R., et al. (2008), Detection of trace Hg^{2+} via induced circular dichroism of DNA wrapped around single-walled carbon nanotubes, J Am Chem Soc, 130, 9190–9191 (DOI: 10.1021/ja801793k)

22. Gu B., Zhou Y., Zhang X., Liu X., Zhang Y., et al. (2016), Thiazole derivative-modified upconversion nanoparticles for Hg^{2+} detection in living cells, Nanoscale, 8, 276–282 (DOI: 10.1039/C5NR05286F)

23. Miao P., Tang Y., Wang L. (2017), DNA modified Fe_3O_4@Au magnetic nanoparticles as selective probes for simultaneous detection of heavy metal ions, ACS Appl Mater Interfaces, 9, 3940–3947 (DOI: 10.1021/acsami.6b14247)

24. Chamier J., Crouch A. M. (2012), Improved photoelectrochemical detection of mercury (II) with a TiO_2-modified composite photoelectrode, Mater Chem Phys, 132, 10–16 (DOI: 10.1016/j.matchemphys.2011.06.041)

25. Kaur N., Singh J., Raj P., Singh N., Singh H., et al. (2016), ZnO decorated with organic nanoparticles based sensor for the ratiometric selective determination of mercury ions, New J Chem, 40, 1529–1534 (DOI: 10.1039/C5NJ03099D)

26. Li Z., Yang R., Yu M., Bai F., Li C., et al. (2008), Cellular level biocompatibility and biosafety of ZnO nanowires cellular level biocompatibility and biosafety of ZnO nanowires. 112, 20114–20117 (DOI: 10.1021/jp808878p)

27. Malandrino G., Blandino M., Fragala M. E., Losurdo M., Bruno G. (2008), Relationship between nanostructure and optical properties of ZnO thin films, J Phys Chem C, 112, 9595–9599 (DOI: 10.1021/jp8001492)

28. Djurišić A. B., Leung Y. H., Tam K. H., Ding L., Ge W. K., et al. (2006), Green, yellow, and orange defect emission from ZnO nanostructures: Influence of excitation wavelength, Appl Phys Lett, 88, 1–3 (DOI: 10.1063/1.2182096)

29. Wang Y. S., Thomas P. J., Brien P. O. (2006), Optical properties of ZnO nanocrystals doped with Cd, Mg, Mn, and Fe ions, J Phys Chem B, 110, 21412–21415 (DOI: 10.1021/jp065441521412–21415)

30. Cao Y., Galoppini E., Ivano P., Duan Z., Lu Y. (2012), Morphology effects on the biofunctionalization of nanostructured ZnO, Langmuir, 28, 7947–7951 (DOI: 10.1021/la3006037)

31. Chey C., Ibupoto Z., Khun K., Nur O., Willander M. (2012), Indirect determination of mercury ion by inhibition of a glucose biosensor based on ZnO nanorods, Sensors, 12, 15063–15077 (DOI: 10.3390/s121115063)

32. Bhanjana G., Dilbaghi N., Kumar R., Kumar S. (2015), Zinc oxide quantum dots as efficient electron mediator for ultrasensitive and selective electrochemical sensing of mercury, Electrochim Acta, 178, 361–367 (DOI: 10.1016/j.electacta.2015.07.113)

33. Sharma S. K., Kaur N., Singh J., Singh A., Raj P., et al. (2016), Salen decorated nanostructured zno chemosensor for the detection of mercuric ions (Hg^{2+}), Sensors Actuators, B Chem, 232, 712–721 (DOI: 10.1016/j.snb.2016.04.017)

34. Nenavathu B. P., Krishna Rao A. V. R., Goyal A., Kapoor A., Dutta R. K. (2013), Synthesis, characterization and enhanced photocatalytic degradation efficiency of Se doped ZnO nanoparticles using trypan blue as a model dye, Appl Catal A Gen, 459, 106–113 (DOI: 10.1016/j.apcata.2013.04.001)

35. Yoneda S., Suzuki K. T. (1997), Detoxification of mercury by selenium by binding of equimolar Hg–Se complex to a specific plasma protein, Toxicol Appl Pharmacol, 143, 274–280 (DOI: 10.1006/taap.1996.8095)

36. Sugiura Y., Tamai Y., Tanaka H. (1978), Selenium protection against mercury toxicity: high binding affinity of methylmercury by selenium-containing ligands in comparison with sulfur-containing ligands, Bioinorg Chem, 9, 167–180 (DOI: 10.1016/S0006-3061(00)80288-4)

37. Ralston N. V. C., Raymond L. J. (2010), Dietary selenium's protective effects against methylmercury toxicity, Toxicology, 278, 112–123 (DOI: 10.1016/j.tox.2010.06.004)

38. Shenasa M., Sainkar S., Lichtman D. (1986), XPS study of some selected selenium compounds. J Electron Spectros Relat Phenomena, 40, 329–337 (DOI: 10.1016/0368-2048(86)80043-3)

39. Chen M., Wang X., Yu Y. H., Pei Z. L., Bai X. D., et al. (2000), X-ray photoelectron spectroscopy and auger electron spectroscopy studies of Al-doped ZnO films, Appl Surf Sci, 158, 134–140 (DOI: 10.1016/S0169-4332(99)00601-7)

40. Gorai P., Ertekin E., Seebauer E. G. (2016), Surface-assisted defect engineering of point defects in ZnO, Appl Phys Lett, 108, 241603 (DOI: 10.1063/1.4953878)

41. Erhart P., Klein A., Albe K. (2005), First-principles study of the structure and stability of oxygen defects in zinc oxide, Phys Rev B, 72, 85213 (DOI: 10.1103/PhysRevB.72.085213)

42. Farhat O. F., Halim M. M., Abdullah M. J., Ali M. K. M., Allam N. K. (2015), Morphological and structural characterization of single-crystal ZnO nanorod arrays on flexible and non-flexible substrates, Beilstein J Nanotechnol, 6, 720–725 (DOI: 10.3762/bjnano.6.73)

43. Solís-Pomar F., Martínez E., Meléndrez M. F., Pérez-Tijerina E. (2011), Growth of vertically aligned ZnO nanorods using textured

ZnO films, Nanoscale Res Lett, 6, 524 (DOI: 10.1186/1556-276X-6-524)

44. Londono-calderon A., Jurado-lasso F. F., Romero-salazar J. D., Jurado-lasso N., Jurado J. F. (2014), Vibrational order, structural properties, and optical gap of ZnO nanostructures sintered through thermal decomposition, Journal of Nanomaterials, 2014, 1–6 (DOI: 10.1155/2014/340384)

45. Han X., Wang G., Zhou L., Hou J. G. (2006), Crystal orientation-ordered ZnO nanorod bundles on hexagonal heads of ZnO microcones: epitaxial growth and self-attraction, Chem Commun, 2, 212–214 (DOI: 10.1039/b512259g)

46. Gao P. X., Wang Z. L. (2004), Substrate atomic-termination-induced anisotropic growth of ZnO nanowires/nanorods by the VLS process, J Phys Chem B, 108, 7534–7537 (DOI: 10.1021/jp049657n)

47. Ahn C. H., Kim Y. Y., Kim D. C., Mohanta S. K., Cho H. K. (2009), A comparative analysis of deep level emission in ZnO layers deposited by various methods, J Appl Phys, 105, 1–5 (DOI: 10.1063/1.3054175)

48. Greene L. E., Law M., Goldberger J., Kim F., Johnson J. C., et al. (2003), L Low-temperature wafer-scale production of ZnO nanowire arrays, Angew Chem-Int Ed, 42, 3031–3034 (DOI: 10.1002/anie.200351461)

49. Studenikin S. A., Golego N., Cocivera M. (1998), Fabrication of green and orange photoluminescent, undoped ZnO films using spray pyrolysis, J Appl Phys, 84, 2287–2294 (DOI: 10.1063/1.368295)

50. Jayalakshmi G., Saravanan K., Balasubramanian T. (2012), Surface functionalization of ZnO films by thiol, Proc SPIE, 8461, 1–7 (DOI: 10.1117/12.929489)

51. Jiménez-Hernández L., Estévez-Hernández O., Hernández-Sánchez H., Díazc A. J., Farías- Sánchez M., et al. (2016), 3-mercaptopropionic acid surface modification of Cu-doped ZnO nanoparticles: Their properties and peroxidase conjugation, Colloids Surfaces A Physicochem Eng Asp, 489, 351–359 (DOI: 10.1016/j.colsurfa.2015.11.010)

52. Zhao X., Li F., Zhang Q., Li Z., Zhou Y., et al. (2015), Mn-doped ZnS quantum dots with a 3-mercaptopropionic acid assembly as a ratiometric fluorescence probe for the determination of curcumin, RSC Adv, 5, 21504–21510 (DOI: 10.1039/C5RA01412C)

53. Bhadra P., Shajahan M. S., Bhattacharya E., Chadha A. (2015), Studies on varying n-alkanethiol chain lengths on a gold-coated surface and their effect on antibody–antigen binding efficiency, RSC Adv, 5, 80480–80487 (DOI: 10.1039/C5RA11725A)

54. Shambetova N., Chen Y., Xu H., Li L., Solandt J., et al. (2016), Acid dissociation of 3-mercaptopropionic acid-coated CdSe–CdS/$Cd_{0.5}Zn_{0.5}S$/ZnS core–multishell quantum dot and strong ionic interaction with Ca^{2+} ion, 120, 3519–3529, J Phys Chem C (DOI: 10.1021/acs.jpcc.5b11023)

55. Ishida T., Choi N., Mizutani W., Tokumoto H., Kojima I., et al. (1999), High-resolution X-ray photoelectron spectra of organosulfur monolayers on Au(111): S(2p) spectral dependence on molecular species, Langmuir, 15, 6799–6806. (DOI:10.1021/la9810307)

56. Šimšíková M., Antalík M., Kaňuchová M., Škvarla J. (2013),

Cytochrome C conjugated to ZnO-MAA nanoparticles: The study of interaction and influence on protein structure, Int J Biol Macromol, 59, 235–241 (DOI: 10.1016/j.ijbiomac.2013.04.064)

57. Wang H., Chen Y., Li Y., Zhang H., Cao J. (2015), A rapid, sensitive and label-free sensor for Hg(II) ion detection based on blocking of cysteine-quenching of fluorescent poly(thymine)-templated copper nanoparticles, RSC Adv, 5, 94099–94104 (DOI: 10.1039/C5RA18906C)

58. Ke J., Li X., Zhao Q., Hou Y., Chen J. (2014), Ultrasensitive quantum dot fluorescence quenching assay for selective detection of mercury ions in drinking water, Sci Rep, 4, 4–9 (DOI: 10.1038/srep05624)

Chapter 4

Defects induced multicolor down- and up-conversion fluorescence in Se doped ZnO nanorods by single wavelength excitation

4.1 Introduction

Photoluminescence is the emission of light that involves the conduction band, valence band, and various defects after absorption of one or more photons. The photon cascade phenomenon involves the absorption of photons of either high or low energy with subsequent emission of lower or higher energy photons through one- and two-photon processes. In down-conversion, single-photon excitation under UV-Vis light gives photoluminescence emission peaks in the visible-NIR region. Whereas in the up-conversion process, multi-photons of NIR was involved with UV-visible emission due to anti-stokes effects [1]. Indeed energy upconversion recently attracted significant advances in photonics [2], and biomedical engineering [3] due to low excitation energy and visible emission with unique nonlinear optical properties [4]. Down-and up-conversion nanomaterials with single [5,6] color emissions have been explored to a large extent, whereas multicolor [7,8] emissions are limited. Single or multicolor emissions are induced mostly due to defect or defects generation during the nanostructure formation. Therefore, understanding the defect's role and their electronic transition in controlling multicolor emissions in nanomaterials by one and two-photon dependent processes leads to the discovery of interesting optoelectronic and biomedical applications.

Introducing defects into nanomaterials has been widely explored because of the generation of unique properties like charge carrier modifications [9], broad emissions, large Stokes shifts [10], and down- and up-

conversion [11] processes. The defects influence the optical properties of materials, and understanding the defects, induced luminescence behavior is essential for optimum use of single and two-photon processes. Defects found in nanostructures are closely related to photon excited electronic transitions between different energy levels [12], which will subsequently influence UV-Vis-NIR emissions. With the rise of multicolor properties in optoelectronic [13], and biomedical [14,15], up-conversion nanomaterials [16] have received intensive attention to develop nanomaterials with new defects. Multicolor emission from nanostructures is possible by overlap [17] of defect transitions based on the combination of defects in the nanostructure. Reports suggest that doping [18,19] is an efficient and straightforward method for defects generation. Understanding the origin of defects, which introduces intermediate state and multicolor emissions in nanomaterials, has great scope for optoelectronic and biomedical applications. Therefore, semiconductors such as ZnO, exhibiting excellent stability and biocompatibility with broad UV-Vis-NIR absorption, could be ideal for one and two-photon processes.

Enormous efforts have been exerted to prepare ZnO based nanomaterials for tuning optoelectronic properties with remarkable inter-band recombination of charge carriers. Additionally, recent reports on the effect of defect centers in ZnO, leading to single color emission, highlights the benefits of using single- and multi-photon sources at room temperature. The defect induced up-conversion luminescence in lanthanide ions (Yb^{3+}, Er^{3+}, and Tm^{3+}) doped ZnO [20,21] nanostructure was explained to intra-4f electronic transitions. Due to their long-lived electronic transitions, rare-earth ions doped ZnO are considered essential nanomaterials not only for photon up-conversion but also for the down-conversion process. Single and two-photon single color emissions in the visible region due to various defect centers in doped and undoped ZnO nanomaterials are extensively studied for different applications. Only limited research has been carried

out on multicolor emissions [22] induced by defects in transition metal-doped ZnO nanomaterials through one and two-photon processes. Therefore, it is essential to understand and fully characterize defects induced down and up-conversion multicolor emission processes in doped ZnO for better optoelectronic and biomedical applications.

In the present chapter, selenium metal is chosen because Se incorporation in ZnO nanostructure induces fluorescence emission by forming various zinc and oxygen defect centers [23] Specific identification of defects for luminescence in the visible region is well studied in Se doped ZnO NRs. However, the origin of luminescence in Se doped ZnO through a two-photon process is not yet reported. Moreover, the mechanism of selenium doped ZnO defects generation and subsequent photoluminescence emission by down- and up-conversion was not explored thoroughly and herein, the mechanism of multicolor emission is explained. In this chapter, the role of defects in Se doped ZnO nanostructure to mediate large Stokes shift, broad emission, photon down-conversion, and up-conversion phenomenon has been investigated.

4.2 Results and Discussion

Se doped ZnO nanorods samples were characterized by XRD, FE-SEM, XPS, and HR-TEM, as reported by our research group very recently [23]. The defects generation in the nanorods under a controlled rate of nucleation and growth during the annealing process was studied from photoluminescence emissions. The possible defects formed if the nucleation rate is faster than crystal growth [24] in Se doped ZnO annealed at 450 °C. This leads to a remarkable increase in the adequate number of defects since annealing at 450 °C induces coalescence and self-assembled ZnO nanoparticles into an NR structure. These Se doped ZnO NRs would provide better insight to understand radiative and non-radiative processes with defect centers. Therefore the role of defects in

optical properties of newly synthesized Se doped ZnO NRs by single and two-photon absorption and emission studies has been investigated in this chapter.

4.2.1 One photo down-conversion optical properties

In a one-photon optical response study, the absorption and emission maxima of Se doped ZnO nanorods were λ_{abs} = 368 nm and λ_{em} = 625 nm with large Stokes shifts of about 250 nm as shown in **Figure 4.1**. The photoluminescence (PL) emission spectrum exhibits a weak ultraviolet emission at 388 nm and a strong, broad visible emission in the region (∼500−800 nm) around 625 nm. The ultraviolet (UV) emission corresponds to free exciton recombination, and a broad visible emission is associated with the generation of extrinsic defects by Se doping. The energy transfer from ZnO defect levels and overlapping [17] of various defects trapped energy states (degenerated states) are responsible for broadband emission in the visible region. Large Stokes shifts and broad PL have originated due to charge transfer and fast relaxation [25] of defect-related trapping sites in the self-assembled [26] nanoparticles. One-photon down-conversion is a predominant mechanism to produce single color emission that has been explored to a large extent with limited defects. Therefore, knowledge about the origin of multiple defects and their corresponding broad visible emission is essential in ZnO NRs for multicolor optical and bioimaging applications.

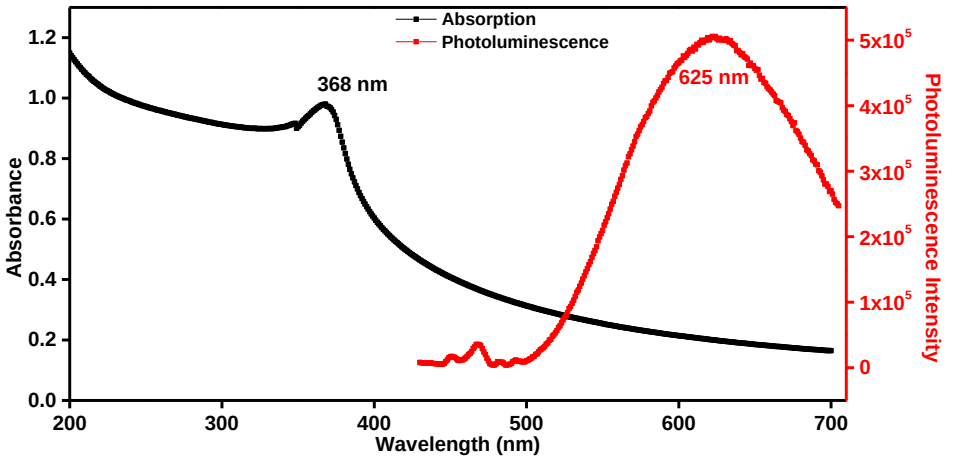

Figure 4.1 UV-Vis absorption and fluorescence spectra of ZnO NRs

Se doped ZnO NRs showed a broad photoluminescence emission peak at 380-720 nm which is due to various energy states [27]. These energy states contain different shallow and deep level defects generated by incorporating Se metal into the ZnO matrix. These defects are generated either due to lattice mismatch creating zinc and oxygen vacancies or due to the Zn and O atoms charge imbalance in the ZnO nanostructure [28].

4.2.2 Multiple defects induced multicolor emissions

The emission peak in **Figure 4.2a** shows a deconvoluted PL spectrum with different emission colors attributed to various kinds of defects in the Se doped ZnO. A maximum of orange-red emission around 625 nm in Se doped ZnO NRs was found to coexist with red, green, and blue emissions. Thus, our results indicate that blue, green, and orange-red emissions are likely to originate from different defect-related [29–31] transitions in agreement with reported literature, as shown in **Figure 4.2b**. These emission colors are consistent with de-convoluted PL emission obtained from PL data showing visible blue (465 nm), green (555 nm), orange-red (625 nm), and red (700 nm) emissions, as shown in **Figure 4.2a**. The mechanism of various (blue, green, orange-red, and red) emissions associated with different defects are related to their transition levels that

are explained based on the full-potential linear muffin-tin orbital method as shown in **Figure 4.2b**. To explore photon excitation conditions in Se doped ZnO, it is likely to create a strong re-absorption effect in the self-assembled nanoparticles that depends on defects that should be illuminated.

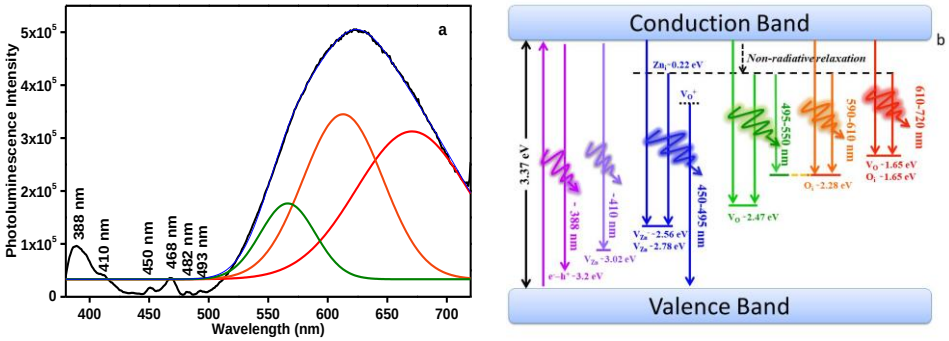

Figure 4.2 (a) Deconvoluted PL spectrum **(b)** Energy levels of defect states in Se doped ZnO NRs bandgap.

The near band, UV-violet emission at 388 nm from Se doped ZnO NRs is due to excitonic state transitions that lie below conduction band (CB) minima. The PL spectrum at 410 nm (violet emission) corresponds to transitions from the CB to shallow zinc vacancy (V_{Zn}) [32] acceptor levels (i.e., CB→ V_{Zn}). The blue emission from 450-495 nm is associated with different electronic transitions from various defects present in the Se doped ZnO NRs. A transition from singly ionized Zn interstitial (Zn_i^+) defects at 0.22 eV below the CB to V_{Zn} levels (i.e., $Zn_i^+ \rightarrow V_{Zn}$) [33] would lead to emission centered at 450 nm. PL emission at 468 nm is due to an electronic transition from CB to singly ionized zinc vacancy (V_{Zn}^-) defects [34] (i.e., CB→V_{Zn}^-). The emission band at 482 nm is due to a radiative transition of an electron from Zn_i donor level to V_{Zn} acceptor level [35]. The PL emission peak at 493 nm is attributed to arise from the defects associated with singly charged oxygen vacancy (V_O^+) [33]. It has also been suggested that green emission from 495–550 nm is generally associated with transition levels of oxygen-related defects (V_O and O_i),

i.e., CB→V_O [36], CB→V_O^{++} [37], and CB→O_i [38] transitions. Orange emission around 590–610 nm has been suggested to originate from radiative de-excitation from deep level doubly ionized $V_O^{++,}$ and O_i states (i.e., CB→O_i and Zn_i→V_O^{++}) transitions [39,40]. Interestingly, orange-red [30] emission centered at 625 nm because of deep level oxygen interstitials (O_i) induced transitions was also observed. Red emission [41] from 620–720 nm arises from radiative de-excitation from Zn_i states to V_O^{++} and O_i states that participate as in orange emission.

4.2.3 Characterization of defects by EPR

The EPR X-band measurement studies of Se doped ZnO NRs provide detailed information regarding various defects associated with different fluorescence as explained above. The EPR spectrum shown in **Figure 2.2** (Chapter 2) exhibiting resonance signals ranging from g∼2.061 to 2.032 has been assigned to zinc vacancy (V_{Zn}) [42] in the lattice. The resonance signal at g∼2.005 has been attributed to oxygen vacancy (V_O) defects [43]. The narrow resonance signal observed at g∼1.962 had been assigned to oxygen interstitial (O_i) defects [42]. Thus, EPR studies reveal different types of defects generated in Se doped ZnO nanostructure and correlates well with observed blue, green, orange, and red PL emissions. The intensity of emissions depends on the concentration of defect sites generated in the crystal lattice. It has been observed that oxygen interstitial and vacancy defects are maximum in the newly synthesized Se doped ZnO NRs responsible for intense red emission, as discussed above.

4.2.4 Electroluminescence studies

The Commission Internationale de l'Eclairage (CIE) chromaticity diagram was calculated using color calculator software for Se doped ZnO NRs emission spectrum with an excitation wavelength at 365 nm. The data obtained were plotted in the Gaussian spectrum with a peak center at 625 nm and FWHM of 170 nm, as shown in **Figure 4.3a**. The PL CIE

coordinates (x, y) were found to be (0.52, 0.49), which lies in the orange-red region shown in **Figure 4.3b**. The CIE chromaticity confirmed that emissions were observed in blue, green, and orange-red regions. This behavior is probably due to a change in the concentration of different defects (V_{Zn}, $V_{o,}$ and O_i) present in Se doped ZnO NRs.

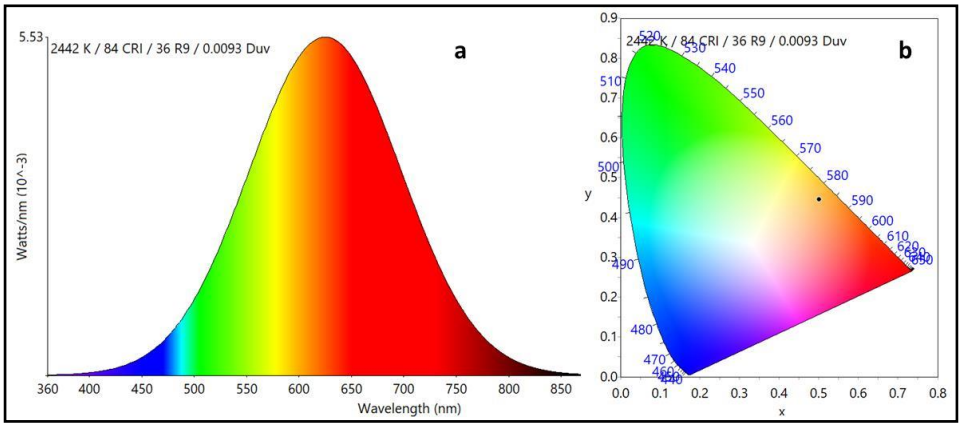

Figure 4.3 (a) Electroluminescence spectra (EL) spectra and **(b)** CIE chromaticity coordinates of in Se-doped ZnO.

4.2.5 One- and two-photo optical studies

PL emission studies were performed with one and two-photon single excitation wavelengths to further confirm the intensity of photoluminescence emission colors of the newly synthesized Se doped ZnO NRs. Se doped ZnO sample having superior optical quality is evident from the contribution of defect-related emissions in PL spectrum within the visible region. In the one-photon excitation study at 360 nm, **Figure 4.4a** shows a broad emission peak with blue, green, and orange-red areas of the spectrum due to different defect-related transitions. In the two-photon excitation study at 720 nm, **Figure 4.4b** shows blue, green, and red emissions in different channels. A possible explanation for observing these multiple emissions is due to the presence of various transitions [29] caused by defects (V_{Zn}, $V_{o,}$ and O_i) generated in the Se doped ZnO NRs.

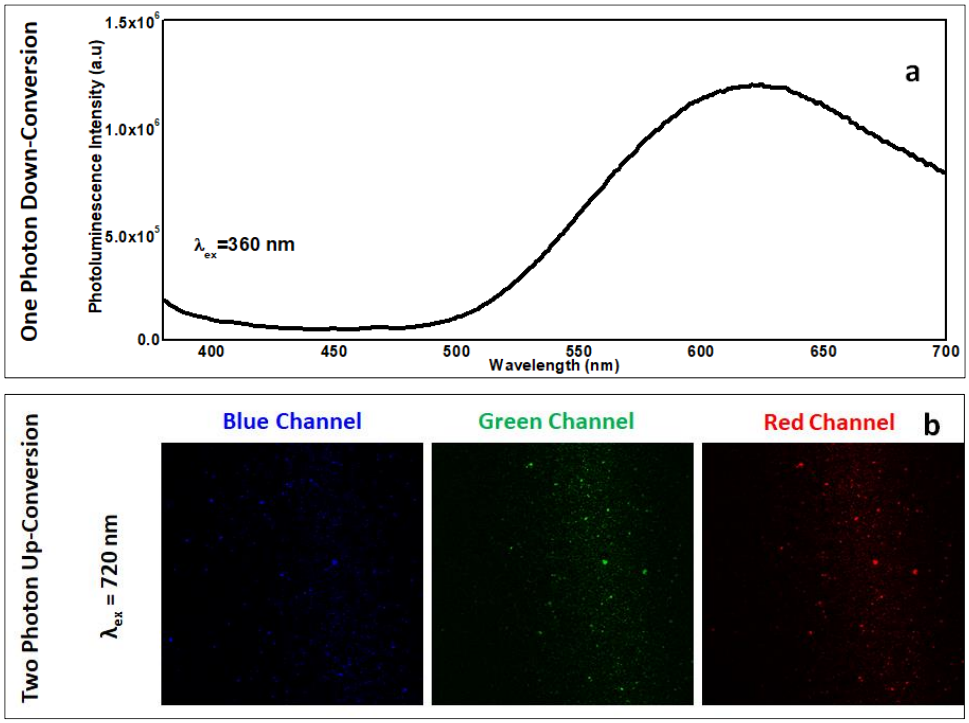

Figure 4.4 Se doped ZnO nanorods emission from **(a)** One-photon (360 nm) and **(b)** Two-photon (720 nm) excitation

Additionally, it is also interesting to study Se doped ZnO NRs with two-photon laser scanning microscopy for examining multicolor emission properties at various single wavelength excitations that can be used for multicolor imaging applications. In continuation of this, next the nonlinear [44] optical responses of Se doped ZnO NRs were examined using laser scanning microscopy with two-photon femtosecond (fs) laser pulses at different excitation wavelengths (λ_{ex}), i.e., at 720, 800, and 860 nm. The color changes from red to blue with increasing two-photon excitation wavelengths from 720-860 nm, implying that the emission is significantly blue-shifted during the two-photon excitation study. The luminescence intensities of blue, green, and red emissions were obtained on separate channels with a single [45] excitation wavelength, as shown in **Figure 4.5b**. For λ_{ex} = 720 nm, the luminescence was dominated by blue, green, and red emissions and is associated with V_{Zn}, $V_{o,}$ and O_i defects. At 800 nm excitation, nearly dominant green and red luminescence were observed

due to oxygen vacancies (V_O). When excited at 860 nm, the luminescence peak was dominated by blue color due to zinc vacancy (V_{Zn}) defects. An intense red emission was also observed than green and blue emissions during two-photon 720 nm excitation, which is in line with one photon (λ_{ex} = 360 nm) PL emission study as shown in **Figure 4.5a**.

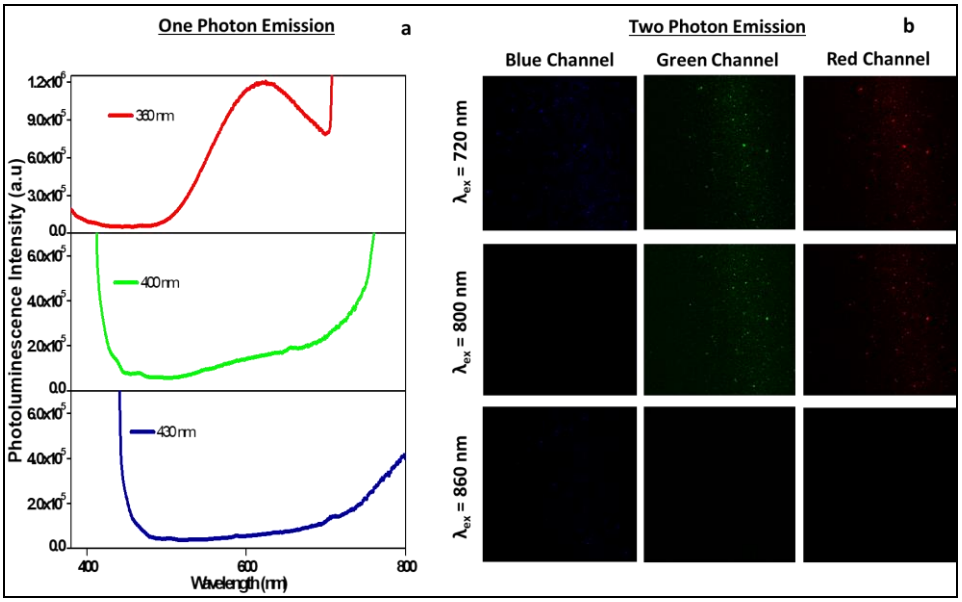

Figure 4.5 (a) Down-conversion (under UV excitation of 360 nm, 400 nm, and 430 nm) and **(b)** Up-conversion (under the excitation of 720 nm, 800 nm, and 860 nm under femtosecond laser pulses) in Se doped ZnO.

Defects in the crystal lattice (V_{Zn}, V_o, and O_i) lead to major intermediate states during the Se doped ZnO nanorods' energy transfer process. These defects, present in high quantity in Se doped ZnO NRs, lead to strong red, green and blue upconversion luminescence emissions. In all these cases, low-intensity colors also appear along with dominant colors in the luminescence emissions, implying selective electronic excitation of defects [46] at a specific wavelength. The multicolor emission in all three channels is mainly due to defects induced broad emission and overlap of defect energy states in the newly synthesized Se doped ZnO NRs.

4.3 Conclusion

In summary, Se doped ZnO nanorods with various defects induced multicolor emission properties were successfully prepared by a mechanothermal method. The material also displayed exceptional one and two-photon multicolor emissions governed by a mechanism of multiple transitions from defect centers generated in the assembled Se doped ZnO NRs. Moreover, a new type of Se doped ZnO NRs material with large Stokes shift and broad visible photoluminescence has been prepared and studied for the first time. At room temperature, the newly synthesized Se doped ZnO NRs excited at 360 nm show broadband visible emission ranging from 400-800 nm due to the presence of multiple deep level defects. Additionally, two-photon excitation at 720 nm shows significant multicolor up-conversion in blue, green, and red channels consistent with one photon measurements of broad visible emission range. The present defect engineering study in Se doped ZnO nanorods thus confers multicolor emissions to the nanomaterial that have great potential applications in bioimaging, optoelectronic and multicolor emission display devices.

4.4 Experimental section

4.4.1 Materials and methods

Se doped ZnO NRs investigated in this chapter were prepared by a mechano-thermal method by heating Se and ZnO at 450 °C as reported earlier in chapters 2 and 3. Single-photon absorption in Se doped ZnO NRs was measured using Fluoromax-4 Spectrofluorimeter (HORIBA Jobin Yvon, model FM-100). PL emission spectrum of Se doped ZnO of 3.68 mM concentration was obtained on a Fluoromax-4 Spectrofluorimeter at 365 nm excitation wavelength. To further examine the defects in Se doped ZnO, X-band (Frequency = 9.45 GHz) EPR spectra were analyzed using electron paramagnetic resonance (EPR)

spectrometer (Bruker) at room temperature. Se doped ZnO NRs sample was two-photon excited using tunable mode-locked Ti:sapphire solid-state laser with a femtosecond pulse in the range 700–900 nm with simultaneous separation of blue, green, and red channels in a Multi-Photon Laser Scanning Microscope (FV1200MPE, IX83 Model, Olympus). Two-photon up-conversion emission of Se doped ZnO nanorods sample was recorded at different excitation wavelengths of 720, 800, and 860 nm and compared with one-photon emission spectra recorded at different excitation wavelengths of 360, 400, and 430 nm.

4.5 References

1. Wilhelm S. (2017), Perspectives for upconverting nanoparticles, ACS Nano, 11, 10644–10653 (DOI: 10.1021/acsnano.7b07120)

2. Ding H., Lu L., Shi Z., Wang D., Li L., et al. (2018), Microscale optoelectronic infrared-to-visible upconversion devices and their use as injectable light sources, Proc Natl Acad Sci, 115, 6632–6637 (DOI: 10.1073/pnas.1802064115)

3. Chen G., Li Z., Wu X., Han G., Zhang Y., et al. (2014), Upconversion nanoparticles: A versatile solution to multiscale biological imaging, Bioconjug Chem, 26, 166–175 (DOI: 10.1021/bc5003967)

4. Wang Y., Deng R., Xie X., Huang L., Liu X. (2016), Nonlinear spectral and lifetime management in upconversion nanoparticles by controlling energy distribution, Nanoscale, 8, 6666–6673 (DOI: 10.1039/c6nr00812g)

5. Wang D. Y., Ma P. C., Zhang J. C., Wang Y. H. (2018), Efficient down- and up-conversion luminescence in Er^{3+}-Yb^{3+} Co-doped $Y_7O_6F_9$ for photovoltaics, ACS Appl Energy Mater, 1, 447–454 (DOI: 10.1021/acsaem.7b00093)

6. Lu H., Gillin W. P., Hernández I. (2014), Concentration dependence of the up- and down-conversion emission colours of Er^{3+}-doped Y_2O_3: A time-resolved spectroscopy analysis, Phys Chem Chem Phys, 16, 20957–20963 (DOI: 10.1039/c4cp02028f)

7. Li F., Li C., Liu X., Bai T., Dong W., et al. (2013), Microwave-assisted synthesis and up-down conversion luminescent properties of multicolor hydrophilic LaF_3:Ln^{3+} nanocrystals, Dalt Trans, 42, 2015–2022 (DOI: 10.1039/c2dt32295a)

8. Zhuang J., Yang X., Fu J., Liang C., Wu M., et al. (2013), Monodispersed β-$NaYF_4$ mesocrystals: In situ ion exchange and multicolor up- and down-conversions, Cryst Growth Des, 13, 2292–2297 (DOI: 10.1021/cg301751c)

9. Hoch L. B., Szymanski P., Ghuman K. K., He L., Liao K., et al. (2016), Carrier dynamics and the role of surface defects: Designing a photocatalyst for gas-phase CO_2 reduction, Proc Natl Acad Sci, 113, E8011-E8020 (DOI: 10.1073/pnas.1609374113)

10. Smith M. D., Watson B. L., Dauskardt R. H., Karunadasa H. I. (2017), Broadband emission with a massive Stokes shift from sulfonium Pb–Br hybrids, Chem Mater, 29, 7083–7087 (DOI: 10.1021/acs.chemmater.7b02594)

11. Wang Q., Zhang Q., Zhao X., Luo X., Wong C. P. Y., et al. (2018), Photoluminescence upconversion by defects in hexagonal boron nitride, Nano Lett, 18, 6898–6905 (DOI: 10.1021/acs.nanolett.8b02804)

12. Wen J., Guo Z., Guo H., Ning L., Duan C. K., et al. (2018), Thermodynamic stabilities, electronic properties, and optical transitions of intrinsic defects and lanthanide ions (Ce^{3+}, Eu^{2+}, and Eu^{3+}) in Li_2SrSiO_4, Inorg Chem, 57, 6142–6151 (DOI: 10.1021/acs.inorgchem.8b00752)

13. Pu Y. C., Hsu Y. J. (2014), Multicolored $Cd_{1-x}Zn_xSe$ quantum dots with type-I core/shell structure: Single-step synthesis and their use as light-emitting diodes, Nanoscale, 6, 3881–3888 (DOI: 10.1039/c3nr06158b)

14. Min Y., Li J., Liu F., Padmanabhan P., Yeow E., et al. (2014), Recent advance of biological molecular imaging based on lanthanide-doped upconversion-luminescent nanomaterials, Nanomaterials, 4, 129–154 (DOI: 10.3390/nano4010129)

15. Cheng L., Yang K., Shao M., Lee S. T., Liu Z. (2011), Multicolor in vivo imaging of upconversion nanoparticles with emissions tuned by luminescence resonance energy transfer, J Phys Chem C, 115, 2686–2692 (DOI: 10.1021/jp111006z)

16. Bian W., Lin Y., Wang T., Yu X., Qiu J., et al. (2018), Direct identification of surface defects and their influence on the optical characteristics of upconversion nanoparticles, ACS Nano, 12, 3623–3628 (DOI: 10.1021/acsnano.8b00741)

17. Reddy G. V. L., Moorthy L. R., Chengaiah T., Jamalaiah B. C. (2014), Multi-color emission tunability and energy transfer studies, Ceram Int, 40, 3399–3410 (DOI: 10.1016/j.ceramint.2013.09.092)

18. Zhou Y., Li W., Wu M., Zhao L. D., He J., et al. (2018), Influence of defects on the thermoelectricity in SnSe: A comprehensive theoretical study, Phys Rev B, 97, 1–8 (DOI: 10.1103/PhysRevB.97.245202)

19. O'Rourke C., Bowler D. R. (2014), Intrinsic oxygen vacancy and extrinsic aluminum dopant interplay: A route to the restoration of defective TiO_2, J Phys Chem C, 118, 7261–7271 (DOI: 10.1021/jp407736f)

20. Liu Y., Xu C., Yang Q. (2009), White upconversion of rare-earth

doped ZnO nanocrystals and its dependence on size of crystal particles and content of Yb^{3+} and Tm^{3+}, J Appl Phys, 105, 1–6 (DOI: 10.1063/1.3088881)

21. Li Y., Wang R., Xu Y., Zheng W., Li Y. (2018), Influence of silica surface coating on operated photodynamic therapy property of Yb^{3+}-Tm^{3+}: Ga(III)-doped ZnO upconversion nanoparticles, Inorg Chem, 57, 8012–8018 (DOI: 10.1021/acs.inorgchem.8b01169)

22. Li Y., Wang R., Zheng W., Li Y. (2018), Ga^{3+} doping induced simultaneous size/shape control, enhanced red upconversion luminescence, and improved X-ray imaging of ZnO:Yb/Tm for multifunctional nanoprobes, Inorg Chem, 57, 12166–12173 (DOI: 10.1021/acs.inorgchem.8b01799)

23. Rao A. V. R. K., Reddy R. B., Sengupta S., Chelvam V. (2018), Efficient ``turn-on'' nanosensor by dual emission-quenching mechanism of functionalized Se doped ZnO nanorods for mercury (II) detection, Appl Nanosci, 8, 1973–1987 (DOI: 10.1007/s13204-018-0875-9)

24. Ridhuan N. S., Abdul Razak K., Lockman Z., Abdul Aziz A. (2012), Structural and morphology of ZnO nanorods synthesized using ZnO seeded growth hydrothermal method and its properties as UV sensing, PLoS One, 7, e50405 (DOI: 10.1371/journal.pone.0050405)

25. Bae C-h, Lim K-S. (2019), Enhanced visible emission in Eu^{3+} doped glass containing Ag-clusters, Ag nanoparticles, and ZnO nanocrystals, J Alloys Compd, 793, 410–417 (DOI: 10.1016/j.jallcom.2019.04.122)

26. Huang H. Y., Cai K. Bin, Talite M. J., Chou W. C., Chen P. W., et al. (2019), Coordination-induced emission enhancement in gold-nanoclusters with solid-state quantum yields up to 40% for eco-

friendly, low-reabsorption nano-phosphors, Sci Rep, 9, 1–11 (DOI: 10.1038/s41598-019-40706-3)

27. Willander M., Nur O., Sadaf J. R., Qadir M. I., Zaman S., et al. (2010), Luminescence from zinc oxide nanostructures and polymers and their hybrid devices, Materials, 3, 2643–2667 (DOI: 10.3390/ma3042643)

28. Layek A., Banerjee S., Manna B., Chowdhury A. (2016), Synthesis of rare-earth doped ZnO nanorods and their defect-dopant correlated enhanced visible-orange luminescence, RSC Adv, 6, 35892–35900 (DOI: 10.1039/c6ra02278b)

29. Djurišić A. B., Leung Y. H., Tam K. H., Ding L., Ge W. K., et al. (2006), Green, yellow, and orange defect emission from ZnO nanostructures: Influence of excitation wavelength, Appl Phys Lett, 88, 1–3 (DOI: 10.1063/1.2182096)

30. Ahn C. H., Kim Y. Y., Kim D. C., Mohanta S. K., Cho H. K. (2009), A comparative analysis of deep level emission in ZnO layers deposited by various methods, J Appl Phys, 105, 1–5 (DOI: 10.1063/1.3054175)

31. Wang Z., Jacobson O., Tian R., Mease R., Kiesewetter D., et al. (2018), An improved prostate-specific membrane antigen targeting agent for prostate cancer imaging and therapy, J Nucl Med, 59, 1–2 (http://jnm.snmjournals.org/content/59/supplement_1/2.abstract)

32. Fang Z., Wang Y., Xu D., Tan Y., Liu X. (2004), Blue luminescent center in ZnO films deposited on silicon substrates, Opt Mater, 26, 239–242 (DOI: 10.1016/j.optmat.2003.11.027)

33. Bayan S., Mohanta D. (2011), Defect mediated optical emission of randomly oriented ZnO nanorods and unusual rectifying behavior of Schottky nanojunctions, J Appl Phys, 110, 1–6 (DOI:

10.1063/1.3631792)

34. Tam K. H., Cheung C. K., Leung Y. H., Djurišić A. B., Ling C. C., et al. (2006), Defects in ZnO nanorods prepared by a hydrothermal method, J Phys Chem B, 110, 20865–20871 (DOI: 10.1021/jp063239w)

35. Anbuselvan D., Muthukumaran S. (2015), Defect related microstructure, optical and photoluminescence behaviour of Ni, Cu co-doped ZnO nanoparticles by co-precipitation method, Opt Mater, 42, 124–131 (DOI: https://doi.org/10.1016/j.optmat.2014.12.030)

36. Zhang S. B., Wei S. H., Zunger A. (2001), Intrinsic n-type versus p-type doping asymmetry and the defect physics of ZnO, Phys Rev B - Condens Matter Mater Phys, 63, 1–7 (DOI: 10.1103/PhysRevB.63.075205)

37. Vanmaekelbergh D., Meijerink A., Meulenkamp E., van Dijken A. (2000), Identification of the transition responsible for the visible emission in ZnO using quantum size effects, J Lumin, 90, 123–128 (DOI: 10.1016/S0022-2313(99)00599-2)

38. Li D., Leung Y. H., Djurišić A. B., Liu Z. T., Xie M. H., et al. (2004), Different origins of visible luminescence in ZnO nanostructures fabricated by the chemical and evaporation methods. Appl Phys Lett, 85, 1601–1603 (DOI: 10.1063/1.1786375)

39. Greene L. E., Law M., Goldberger J., Kim F., Johnson J. C., et al. (2003), Low-temperature wafer-scale production of ZnO nanowire arrays, Angew Chem Int Ed, 42, 3031–3034 (DOI: 10.1002/anie.200351461)

40. Kegel J., Laffir F., Povey I. M., Pemble M. E. (2017), Defect-promoted photo-electrochemical performance enhancement of

orange-luminescent ZnO nanorod-arrays, Phys Chem Chem Phys, 19, 12255–12268 (DOI: 10.1039/c7cp01606a)

41. Alvi N. H., ul Hasan K., Nur O., Willander M. (2011), The origin of the red emission in n-ZnO nanotubes/p-GaN white light emitting diodes, Nanoscale Res Lett, 6, 1–7 (DOI: 10.1186/1556-276X-6-130)

42. Pöppl A., Völkel G. (1991), ESR and photo-ESR investigations of zinc vacancies and interstitial oxygen ions in undoped ZnO ceramics, Phys status solidi, 125, 571–581 (DOI: 10.1002/pssa.2211250218)

43. Pöppl A., Völkel G. (1990), ESR and photo-ESR investigations of the V centre in ZnO raw material and Li-doped ZnO ceramic powder, Phys status solidi, 121, 195–204 (DOI: 10.1002/pssa.2211210123)

44. Li H., Zhang C.-Y., Li X.-F., Xiang J., Tie S.-L., et al. (2015), Enhanced upconversion luminescence from ZnO/Zn hybrid nanostructures induced on a Zn foil by femtosecond laser ablation, Opt Express, 23, 30118 (DOI: 10.1364/oe.23.030118)

45. Lacoste T. D., Michalet X., Pinaud F., Chemla D. S., Alivisatos A. P., et al. (2000), Ultrahigh-resolution multicolor colocalization of single fluorescent probes, Proc Natl Acad Sci, 97, 9461–9466 (DOI: 10.1073/pnas.170286097)

46. Raghavendra A. J., Gregory W. E., Slonecki T. J., Dong Y., Persaud I., et al. (2018), Three-photon imaging using defect-induced photoluminescence in biocompatible ZnO nanoparticles, Int J Nanomedicine, 13, 4283–4290 (DOI: 10.2147/IJN.S165201)

Chapter 5

Conclusions and Scope for Future Work

5.1 Conclusion

This chapter aims to review Se doped ZnO NR's current and significant future applications in monitoring the environment and health. This thesis focuses on the synthesis of Se doped ZnO nanorods with multiple defects. These defects induce catalytic properties in Se doped ZnO for biodiesel production, mercury detection, optical down-upconversion by one and two-photon fluorescence studies that has environmental and healthcare applications.

Chapter 1 provides a general introduction of the environmental contaminants, healthcare dependence, its global status and conventional monitoring techniques. The emerging environmental and healthcare issues employ nanotechnology-based materials for energy production, mercury detection, and disease detection. The chapter details n-type and p-type doping and their importance in tuning different properties. It concludes with a review of ZnO defects induced properties in catalysis, sensing, and two-photon optical diagnostic material for environmental and healthcare applications.

Chapter 2 describes the synthesis of a new heterogeneous Se doped ZnO base catalyst for transesterification of vegetable oil to fatty methyl esters (FAME) or biodiesel. Surface area defects, mainly oxygen interstitials and oxygen vacancies, formed in Se doped ZnO's crystal lattice are characterized by PL, XRD, and EPR studies. These surface area defects play a vital role in improving base site reactivity, which was demonstrated by a transesterification reaction. The optimum reaction condition reveals the usage of 1:20 oil to methanol volume ratio, 5 wt.% catalyst load, 65 °C as reaction temperature to give a maximum yield of 94.7% FAME in 3

h. The nanocatalyst was recyclable without loss of FAME yield and can be used for industrial-scale biodiesel production.

Chapter 3 describes the preparation and application of orange-red luminescent Se doped ZnO nanorods coated with 3-mercaptopropionic acid (MPA), a chelating ligand to detect mercury ions because of the strong affinity of –SH functionality. In the presence of Hg^{2+} ions, MPA–Se doped ZnO nanoprobe show an efficient turn-on mechanism over dual emission-quenching phenomenon. Also, a linear fit of photoluminescence (PL) spectrum for various concentrations of Hg^{2+} ions provides compelling evidence for emission (R^2=0.990) over quenching (R^2=0.888) pathways, which is in support of our proposed mechanism. Therefore this "turn-on" MPA coated Se doped ZnO nanosensor was employed for selective detection of Hg^{2+} ions with the lowest limit of detection concentration to 1 pM. The studies demonstrate that our direct, rapid, and practical approach for mercury detection using this nanoprobe will offer great potential for monitoring Hg^{2+} ions from the environment and healthcare products.

Chapter 4 explores the generation of multiple zinc (V_{Zn}), oxygen (V_O) vacancies, and oxygen interstitials (O_i) defects for inducing multicolor emissions by single and two-photon single wavelength excitations. The photoluminescence studies reveal that single-photon excitation exhibits a broad multicolor emission peak from 400-800 nm with λ_{max} at ~625 nm and a large Stokes shift of about 250 nm. The de-convolution peaks within the superposition of defects (V_{Zn}, $V_{O,}$ and O_i) induce multicolor broadband emission to show blue, green, and red emissions consistent with their corresponding defects. The EPR signals also reveal detailed information about these defects and correlate with optical-electronic transition states in Se doped ZnO NRs. Moreover, the two-photon up-conversion luminescence of Se doped ZnO NRs also shows multicolor (blue, green,

and red) emissions from the channel at 720 nm excitation. Two-photon confocal studies of Se doped ZnO NRs show multicolor emission at 720, 800, and 860 nm excitations consistent with one photon fluorescence at 360, 400, 430 nm excitations. Therefore, these defects induced multicolor emissions by one, and two-photon excitation wavelengths have potential optoelectronic and biomedical applications.

5.2 Scope for future work

This thesis deals with the generation of multiple defects induced catalytic and optical properties in the nanomaterial for environmental and healthcare applications. Se doping in ZnO introduce defects and change bandgaps leading to significant tuning of the photophysical, electrochemical, catalytic, and optical properties. Selenium-based materials can tune the bandgap directly leading to charge carrier collection that impact opto-electronic properties of solar cells [1,2]. Se doped ZnO two-photon upconversion process can be employed for targeted optical imaging by surface conjugation of monoclonal antibodies, peptides, receptor antagonists, and aptamers. ZnO NRs can also exhibit simultaneous imaging and therapy with optical drug cargo conjugates [3,4]. The dual-modality ZnO NRs are readily applicable for bioimaging and therapeutic applications.

5.3 References

1. Patil S. S., Khot K. V, Mali S. S., Hong C. K., Bhosale P. N., (2007), Investigating the role of selenium-ion concentration on optoelectronic properties of the $Cu_2ZnSn(S_{1-x}Se_x)_4$ thin films, Ind Eng Chem Res, 59, 10868–10881 (DOI: 10.1021/acs.iecr.0c00294)

2. Taskesen T., Pareek D., Neerken J., Schoneberg J., Hirwa H., et al., (2007), The effect of excess selenium on the opto-electronic properties of $Cu_2ZnSnSe_4$ prepared from Cu–Sn alloy precursors,

RSC Adv, 9, 20857–20864 (DOI: 10.1039/C9RA02779C)

3. Hong H., Wang F., Zhang Y., Graves S. A., Eddine S. B. Z., et al., (2007), Red fluorescent zinc oxide nanoparticle: A novel platform for cancer targeting, ACS Appl Mater Interfaces, 7, 3373–3381 (DOI: 10.1021/am508440j)

4. Hong H., Shi J., Yang Y., Zhang Y., Engle J. W., et al., (2007), Cancer-targeted optical imaging with fluorescent zinc oxide nanowires, Nano Lett, 11, 3744–3750 (DOI: 10.1021/nl201782m)